

EXFOLIATION AND SENSING APPLICATION OF 2D MATERIALS

BY SONIA BICCAI



A THESIS SUBMITTED UNDER THE SUPERVISION OF
PROFESSOR JONATHAN N. COLEMAN

FOR THE DEGREE OF
DOCTOR OF PHILOSOPHY

IN THE SUBJECT OF
PHYSICS

SCHOOL OF PHYSICS,
TRINITY COLLEGE DUBLIN

2020

DECLARATION

I declare that this thesis has not been submitted as an exercise for a degree at this or any other university and it is entirely my own work.

I agree to deposit this thesis in the University's open access institutional repository or allow

the library to do so on my behalf, subject to Irish Copyright Legislation and Trinity College

Library conditions of use and acknowledgement.

Elements of this work that have been carried out jointly with others or by collaborators

have been duly acknowledged in the text wherever included.

Sonia Biccai

EXFOLIATION AND SENSING APPLICATION OF 2D MATERIALS

Abstract

In the past decade, graphene and layered material such as Transition metal dichalcogenides (TMDs) and Transition metal oxides (TMOs) have been investigated for their importance in several applications. For example, these materials can be used in several fields such as energy storage and sensing device production; additionally, some of these important devices need to be scaled up for mass production. In this work, production of 2D material has been performed by liquid phase exfoliation (LPE) and the nanosheet study has been followed by strain sensor fabrication, incorporating the nanosheet in a polymeric matrix. Afterwards, a statistical computer program has been used to build a scheme able to predict the interactions between the composite variables. These predictions describe when and how the results are dependent on different variables.

Liquid phase exfoliation is a scalable method to produce large quantities of few-layer 2D materials. Here, we report on the scale-up production of WS₂ in water and surfactant using shear exfoliation. Liquid exfoliation was performed changing processing parameters such as WS₂ concentration, surfactant (Sodium Cholate, NaC) concentration, total volume, shear time, and shear rate. The extinction spectra for LPE WS₂ was measured and empirical metrics allowed us to calculate the mean thickness and concentration of the dispersed nanosheets. The scaling equation of WS₂ exfoliation in water and NaC was found and WS₂ concentration and production rate were optimized, reaching a concentration of WS₂ nanoflakes of 1.82 g/L and a production rate of 0.95 g/h.

With the development of sensor technology, the growing demand of strain sensors has taken place to realize devices such as wearable electronics necessary for biomonitoring, or devices able to detect pressure or vibration changes. For this reason, the necessity to improve mechanical and electrical properties led to the use of nanocomposites as strain sensors. Nanocomposites exploit the combined properties of both filler and matrix. A strain sensor is a material that changes its resistance when a strain is applied and, commonly, the resistance increases during the tensile deformation. The strain gauge is related to the change of resistance as a

function of strain variation. The higher the gauge factor, the better the performance of the strain sensor. Considering that the strain gauge tells how fast the resistance changes as the composite is stretched, if the resistance increases, the gauge factor has positive values and for nanocomposites; this value can have a range from 2 to 500. Here, TMDs properties have been investigated including the nanomaterials in a poly (ethylene oxide) (PEO) matrix. The doping of TMDs (i.e. WS_2 and MoS_2) by the PEO yields conductive nanocomposites which act like sensors while stress transfer leads to nanosheets deformation. As a result, negative gauge factor has been found for these materials. This behaviour can be related to the band gap change of the material; in fact, spectroscopic and theoretical studies showed that the band gap of MoS_2 can be changed under strain, implying a negative piezoresistivity. However, MoS_2 -PEO composite gauge factors are approximately -25 , but fall to -12 for WS_2 -PEO composites and roughly -2 for PEO filled with MoSe_2 or WSe_2 . In this work, electromechanical properties of these nanocomposites have been studied. We also develop a simple model which describes all these observations and show that these composites can be used as dynamic strain sensors. Different parameters describe how performant a sensor is and gauge factor and hysteresis are two of them. The gauge factor describes the electrical properties of a material and determines how the resistance changes as a function of strain. The hysteresis tells more about the mechanical properties of a polymeric composite. In particular, it describes the degree of material elasticity. So far, many attempts have been made to find a nanocomposite with both high gauge factor and low hysteresis proving this challenge particularly difficult. One solution could be combining several polymeric matrixes with nanosheets in order to obtain characteristics of all materials that would provide us with the desired properties. In the last part of this work, a statistical program called Design of Experiment (DOE) has been used to predict the best ensemble of variables that would provide the optimization of both gauge factor and hysteresis. Here, different ratios of two different silicon-based polymeric matrixes have been used such as Sylgard 170® and silicone oil with different oil viscosities. Finally, graphene nanosheets have been included into the matrix and the relationship between these parameters has been studied.

List of Keywords:

Layered Materials, 2D Nanosheets, Liquid Phase Exfoliation, Shear Mixing Exfoliation, Transition Metal Dichalcogenide, Strain Sensors, Nanocomposites, Polymers, Design of Experiment, Gauge Factor, Hysteresis.

List of Publications

1. Khan U, **Biccai S**, Boland S C, Coleman J N. Low cost, high performance ultrafiltration membranes from Glass fiber-PTFE-graphene composites (in progress)
2. **Biccai S**, Boland C S, O'Driscoll D P, Harvey A, Gabbett C P, O'Suilleabhain D R, Griffin A J, Li Z, Young R, Coleman J N. Negative gauge factor piezoresistive composites based on polymers filled with MoS₂ nanosheets. ACS nano acsnano.9b01613 (2019). doi:10.1021/acsnano.9b01613 (**chapter 5**).
3. **Biccai S**, Barwich S, Boland D, Harvey A, Hanlon D, McEvoy N, Coleman JN. Exfoliation of 2D materials by high shear mixing. 2D Materials. 2018 Oct 30;6(1):015008 (**chapter 4**).
4. A. J. Ryan, C. J. Kearney, N. Shen, U. Khan, A. G. Kelly, C. Probst, E. Brauchle, **S. Biccai**, C. D. Garcarena, V. Vega-Mayoral, P. Loskill, S. W. Kerrigan, D. J. Kelly, K. Schenke-Layland, J. N. Coleman, F. J. O'Brien, Adv. Mater. 2018, 30, 1706442.
5. V. Alzari, V. Sanna, **S. Biccai**, T. Caruso, A. Politano, N. Scaramuzza, M. Sechi, D. Nuvoli, R. Sanna, A. Mariani, Tailoring the physical properties of nanocomposite films by the insertion of graphene and other nanoparticles, Composites Part B: Engineering, Volume 60, 2014, Pages 29-35, ISSN 1359-8368.

ACKNOWLEDGEMENT

First of all, I would like to thank Johnny for giving me the opportunity to work with him and with this wonderful group. I don't want to get too sentimental and I'm just honest when I say that I consider myself very lucky on having him as a supervisor. He's been a constant guide and support and thanks to him, I had the chance to grow as a scientist and overall as a person since the first Pavinar.

I would like to thank my "lab-mentor" Umar. He's been the first one who believed that a little forgetful Sardinian chemist could go through this PhD (even before myself) and I wanted to tell him that I kept my promise and I didn't burn and/or made explode anything. I want to thank the old Coleprople Claudia, Keith, Andrew, Dave, Damo, Tom, Peter, Victor and Zahra my liver has been trained as much as my exfoliation knowledge. I want to thank my Fitz-brothers Conor for all his support and for every "SISTER SISTEEER" sang in the lab and Dan for his incredible help and probably the craziest stories I've ever heard (I have just one advice for the new colemen/colewomen: don't listen to Dan when he talks about keto-diet, it doesn't work! case closed). To my favourite Honey Badger, to the Cowboy, and the Archangel JBriel thanks for the laughs and for brightening up the days in the office you guys made those stairs worth climbing (PS: I officially claim the ruler as mine). To Adam (the "PhD writing bible" saved this work from being just a bunch of disconnected sentences) and Seb, thanks a lot guys that key was my nightmare. To my travel partner Aideen, Yash, James and Ruiyuan for all the help, all the laughs, all the support, and overall all the drinks shared. To Ema for the coffees and the hours spent sharing the "joy" of being a PhD student. To Romina, Brigita, Patricia, my two little sisters Marta and Paola and the "new arrivals" Maria, Mia, and Dorotea thanks for putting up with me and even when every judge could have had justified an attempted murder, you just kept being my Irish family. To James (not from Donegal), thanks.

Ovviamente non potevo finire questa tesi senza scrivere i ringraziamenti anche nella mia lingua (non vi preoccupate non le scrivo in sussinco). Vorrei iniziare precisando che qui si conclude il mio capitolo da studente, per cui mi sembra doveroso ringraziare i miei primi insegnanti di vita: i miei genitori e i miei nonni. Ringrazio

mia sorella (e migliore amica) Fotokiok per esserci sempre e comunque. Ringrazio tutta la mia (non tanto normale) famiglia: tutti in un modo o nell'altro mi sostenete anche da lontano e se sono la Ponga di oggi lo devo a voi. Ringrazio la maestra Gavina e le maestre Maria Paola, Vanna e Rita per aver alimentato la mia curiosità da piccola, questo lavoro è un po' anche il vostro. Un grazie speciale va a tutti i miei amici oltremare per non essersi (ancora) stancati di me: in particolare a Stefania e Iolanda spietate rivali di "cinque" e amiche insostituibili da una vita. Grazie alle mie chimiche preferite (Eli, Nini, Vale e Vero), alle mie vecchiette preferite (Eli e Gabri), al mio miramico preferito (Davide) e alle mie troddione preferite (ovviamente Giulia e Ale).

Ho concluso le precedenti tesi con una frase che in un modo o nell'altro rappresentasse il mio stato d'animo, un momento particolare della mia vita, o che semplicemente mi avesse fatto morire dalle risate e, finalmente, ho trovato quella perfetta per questo dottorato:

*“Se la vita ti da limoni, tu congelali e tirali piu' forte che puoi a chi t'ha rotto i cogli*ni”*

TABLE OF CONTENTS

MOTIVATION AND THESIS OUTLINE	1
1.1 MOTIVATION	1
INTRODUCTION AND BACKGROUND THEORY	5
2.1 INTRODUCTION	5
2.2 GRAPHENE AND LAYERED MATERIALS	10
2.2.1 Transition Metal Dichalcogenides (TMDs)	13
2.3 EXFOLIATION OF 2D-MATERIALS	17
2.3.1 Liquid Phase Exfoliation	20
2.3.2 Dispersion Theory	23
2.3.3 Shear Mixer Theory	29
2.4 POLYMERS AND COMPOSITES	33
2.4.1 Polymers	33
2.4.2 Polyethylene Oxide (PEO)	38
2.4.3 Polydimethylsiloxane (PDMS)	39
2.4.4 Composites	40
2.4.5 0D Particles	41
2.4.6 1D Particles	43
2.4.7 Mechanical properties of materials	44
2.4.8 Effect of fillers on mechanical properties	51
2.4.9 Effect of the fillers on the electrical properties	53
2.4.10 Sensing materials: Piezoresistive effect	58
2.5 DESIGN OF EXPERIMENT	61
MATERIALS AND METHODS	67
3.1 INTRODUCTION	67
3.2 MATERIALS	67
3.3 SCALED-UP PRODUCTION OF WS ₂ NANOSHEETS VIA SHEAR MIXING EXFOLIATION	68
3.4 COMPOSITE PREPARATION (PEO/TMDs/GRAPHENE)	69
3.5 DESIGN OF PIEZORESISTIVE MULTI-MATRIX STRAIN SENSORS (PDMS/SYLGARD/GRAPHENE)	70
3.6 CENTRIFUGATION	72
3.7 UV-VIS SPECTROSCOPY	72
3.8 RAMAN SPECTROSCOPY	75
3.9 TRANSMISSION ELECTRON MICROSCOPY (TEM)	76
3.10 SCANNING ELECTRON MICROSCOPY (SEM)	79
3.11 ATOMIC FORCE MICROSCOPY (AFM)	80
3.12 ELECTROMECHANICAL TESTING	82
EXFOLIATION OF 2D MATERIALS BY HIGH SHEAR MIXER	83
4.1 INTRODUCTION	83
4.2 PROCEDURE	85

4.2.1 Pretreatment	85
4.2.2 Shearing step	86
4.3 RESULTS	87
4.3.1 Surfactant concentration variation	90
4.3.2 Shear rate variation	91
4.3.3 Initial concentration dependence	92
4.3.4 Volume study	92
4.3.5 Time dependence	93
4.4 CONCLUSIONS	98
NEGATIVE GAUGE FACTOR PIEZORESISTIVE NANOCOMPOSITES....	100
5.1 INTRODUCTION	100
5.2 PROCEDURE	101
5.2.1 Nanomaterial preparation	101
5.2.2 Film preparation.....	101
5.2.2 Electromechanical testing	102
5.2.3 <i>In-situ</i> Raman deformation test.....	103
5.3 RESULTS	103
5.3.1 Nanosheets production and analysis	103
5.3.2 Composite basic characterization	105
5.3.3 Electromechanical properties	113
5.3.4 Modelling composite piezoresistance	117
5.4 CONCLUSIONS	124
EXPERIMENTAL DESIGN OF POLYMER:POLYMER /GRAPHENE NANOCOMPOSITES	126
6.1 INTRODUCTION	126
6.2 PROCEDURE	129
6.2.1 Preliminary Studies on the Variables and Program Settings	129
6.2.2 Sample preparation	133
6.2.3 Electromechanical testing	133
6.3 RESULTS	135
6.4 CONCLUSIONS	141
CONCLUSIONS AND FUTURE WORK	143
7.1 CONCLUSIONS	143
7.2 FUTURE WORK	145
REFERENCES	146

LIST OF FIGURES

Fig.2.1. <i>Some of the allotropic forms of carbon</i>	11
Fig.2.2. <i>Band structure of graphene</i>	13
Fig.2.3. <i>Structure of BN, BP and TMOs</i>	14
Fig.2.4. <i>Representative structure of TMDs</i>	15
Fig.2.5. <i>Band structure of MoS₂ and WS₂</i>	15
Fig.2.6. <i>Schematic of the structural polytypes of TMDs</i>	16
Fig.2.7. <i>Graphic representation of the Sol-Gel method</i>	18
Fig.2.8. <i>Graphic demonstration of 2D-nanosheet production through CVD</i>	19
Fig.2.9. <i>Classic representation of Liquid Phase Exfoliation</i>	20
Fig.2.10. <i>Various dispersed materials obtained via LPE over the years</i>	21
Fig.2.11. <i>Examples of machines used in LPE</i>	22
Fig.2.12. <i>Schematic representation of surfactant</i>	26
Fig.2.13. <i>Representative image of the nanoparticle surface stabilised by the surfactant</i>	27
Fig.2.14. <i>Images of the shear mixer (Silverson, L5M series)</i>	30
Fig.2.15. <i>Graphic representation of shearing steps</i>	31
Fig.2.16. <i>Schematic representation of the delamination process</i>	32
Fig.2.17. <i>Different grouping of polymeric matrices</i>	35
Fig.2.18. <i>Examples of the most common plastics used and their applications</i>	35
Fig.2.19. <i>Examples of common elastomers</i>	36
Fig.2.20. <i>Schematic representation of crosslinked elastomers</i>	37
Fig.2.21. <i>Polyethylene oxide structure</i>	39
Fig.2.22. <i>PDMS structure</i>	40
Fig.2.23. <i>Schematic representation of different deformations</i>	45
Fig.2.24. <i>Schematic stress-strain diagram</i>	47
Fig.2.25. <i>Graphic representation of a plastic curve</i>	48
Fig.2.26. <i>Response of different materials as a load is applied</i>	49
Fig.2.27. <i>Schematic tensile stress-strain curve for a semicrystalline polymer</i>	49
Fig.2.28. <i>Stress-strain curve for a purely elastic material</i>	50
Fig.2.29. <i>Graphic representation of composites</i>	54
Fig.2.30. <i>Percolation steps</i>	56
Fig.2.31. <i>Schematic representation of piezoresistive behaviour</i>	58
Fig.2.32. <i>First step of DOE</i>	62
Fig.2.33. <i>Computed table of DOE runs</i>	63
Fig.2.34. <i>Data collection of DOE</i>	64
Fig.2.35. <i>Display of model specification to fit the data of DOE</i>	65
Fig.2.36. <i>Prediction profiler of an experiment designed</i>	66
Fig.3.1. <i>Extinction, Absorption and scattering spectra of MoS₂</i>	74
Fig.3.2. <i>Graphic representation of Rayleigh and Raman scattering</i>	76
Fig.3.3. <i>Schematic of a TEM column</i>	78
Fig.3.4. <i>Possible outcomes after an electron beam interacts with the specimen</i>	78

Fig.3.5. Schematic representation of a SEM column.....	80
Fig.3.6. General representation of AFM operation.....	81
Fig.3.7. Schematic representation of tensile tester apparatus.....	83
Fig.4.1. Graphic representation of WS ₂ preparation.....	85
Fig.4.2. Images of impurities collected after pretreatment.....	85
Fig.4.3. Extinction coefficient vs ratio of extinctions at A exciton and at 350 nm	88
Fig.4.4. Ratio of extinction at 365 nm and 465 nm vs flake size.....	89
Fig.4.5. TEM images and relative histogram and Raman spectrum of WS ₂ in H ₂ O/NaC.....	90
Fig.4.6. UV-vis spectra, C, <L> and <N> of WS ₂ vs NaC concentration	91
Fig.4.7. AFM and concentration of WS ₂ vs processing parameters	94
Fig.4.8. WS ₂ nanosheets' thickness as a function of processing parameters.....	95
Fig.4.9. WS ₂ nanosheets' length as a function of processing parameters	96
Fig.4.10. UV-vis spectrum of WS ₂ at high concentration	97
Fig.4.11. WS ₂ concentration versus scaling equation with high concentration value	97
Fig.5.1. Nanocomposite films containing different MoS ₂ 's loading level	102
Fig.5.2. Characterizations of MoS ₂ dispersion.....	104
Fig.5.3. TEM of WS ₂ , MoSe ₂ , WSe ₂ and graphene nanosheets.....	105
Fig.5.4. Raman spectra measured on a PEO film and MoS ₂ /PEO.....	106
Fig.5.5. Stress-strain curves of different MoS ₂ mass fractions.....	107
Fig.5.6. Representative stress-strain curves for selected MoS ₂ /PEO composites	108
Fig.5.7. Conductivity plotted versus MoS ₂ volume fraction for MoS ₂ /PEO composites.....	111
Fig.5.8. The procedure adopted in order to verify the doping effects of PEO on MoS ₂	112
Fig.5.9. SEM images of composite PEO/MoS ₂ films for different M _f	113
Fig.5.10. Electromechanical response of MoS ₂ /PEO	114
Fig.5.11. Raman band position vs strain	115
Fig.5.12. Dynamic strain profiles vs resistance at three different frequencies ...	116
Fig.5.13. Response of 5wt.-% MoS ₂ /PEO composite to step strains	117
Fig.5.14. Resistance vs strain plot for two samples of PEO/graphene samples. .	121
Fig.5.15. R _{I,0} /R _{NS,0} vs ϕ	122
Fig.5.16. Typical stress/strain and resistance/strain curves of PEO composites.....	124
Fig.5.17. Representative resistance-strain curves for composites of PEO.....	124
Fig.6.1. Polycondensation reaction of PDMS	126
Fig.6.2. Stress-strain curve of G-Putty and its hysteresis value (inset).	127
Fig.6.3. n! relationship between variables and samples required.....	128
Fig.6.4. Gauge factor as a function of time at 50, 70 and 100 °C.....	130
Fig.6.5. Cyclic stress-strain curve and hysteresis values of Sylgard/PDMS.....	132

Fig.6.6. <i>Stress-strain curve of a viscoelastic material during a loading-unloading cycle.</i>	134
Fig.6.7. <i>Stress-strain curves with calculated hysteresis (inset) for each sample prepared.</i>	135
Fig.6.8. <i>$\Delta R/R_0$, as a function of strain</i>	136
Fig.6.9. <i>Table of DOE with reported results</i>	136
Fig.6.10. <i>Prediction profiler with a selection of random factors</i>	137
Fig.6.11. <i>Stress-strain curve and $\Delta R/R_0$ as a function of strain % of the DOE...</i>	138
Fig.6.12. <i>Prediction profiler of the best sample</i>	138
Fig.6.13. <i>Images of the final nanocomposite</i>	139
Fig.6.14. <i>Dynamic strain profiles at two different frequencies</i>	139
Fig.6.15. <i>Responses of Sylgard/PDMS/graphene composite to step strains of 4%.</i>	140
Fig.6.16. <i>Dynamic strain profiles of G-Putty</i>	141

LIST OF TABLES

Table 3.1. <i>DOE test</i>	63
Table 4.1. <i>Pretreatment parameters</i>	75
Table 4.2. <i>Shearing parameters</i>	76
Table 4.3. <i>Beakers capacitance</i>	81
Table 6.1. <i>Sylgard curing times vs temperature</i>	108
Table 6.2. <i>DOE runs table</i>	111

*To Dario,
For the best puzzle
competitions I have ever had*

*To my Nonno,
For the best “pani e zuccaru”
I could ever wish*

Motivation and Thesis Outline

1.1 MOTIVATION

Throughout the past decades, nanoscience has been the driving force towards technological progress while over the last 15 years, an enormous jump forward has been made thanks to the joint findings of chemistry, engineering, and material science. When the first carbon nanotubes^{1,2} and fullerenes³ were described, the interest of industry was brought towards nanomaterials; however, it was only after the isolation of graphene⁴ in 2004, and the successful re-discovery of layered materials,⁵⁻⁸ that this interest grew exponentially. There has been plenty of confident speculation over the potential of these materials, and, in order to fully harness this potential, a separate branch of material science has been developed. This new branch has been dedicated entirely to the preparation, scalability, and application of layered materials.⁹⁻¹⁷

The necessity of a better understanding of 2D materials inspired me to explore all the different aspects of research, starting from preparation and going to application. However, it is possible to divide our research in three main parts: scale up exfoliation of 2D materials, sensing application and experimental design. The first part concerns the preparation of layered materials. Here, we aimed to further understand liquid phase exfoliation (LPE)^{18,19} as a preparation method of 2D materials. Indeed, while the liquid exfoliation of graphene^{18,20-23} has been largely explored going from sonic tip to shear exfoliation, other layered materials require more in depth study. For instance, tungsten disulphide (WS₂) has been fully explored in terms of liquid exfoliation, but the use of this material in applications like batteries,²⁴⁻²⁷ transistors^{28,29} and modern electronic devices requires scalability as well. However, this has been barely explored before using liquid exfoliation and therefore warrants further examination. Here, we focused our attention on liquid shear exfoliation of tungsten disulphide in water and surfactant (sodium cholate,

NaC) and developed an equation that describes the WS_2 final concentration as a function of several parameters.³⁰

This brought us to the second part of our work where TMDs have been incorporated in a polymeric matrix for sensing applications. Indeed, while other more conducting materials have been widely explored, TMDs based strain sensors are not commonly investigated because of their lower conductivity. Furthermore, a model that describes the piezoresistivity of polyethylene oxide (PEO) nanocomposites has been developed, which focused our attention on negative piezoresistivity of PEO/molybdenum disulphide (MoS_2) composites. Finally, we went from a simple system of strain sensor composed of just a polymer (PEO) and filler (TMD) to a more complex system where nanocomposites have been prepared using exfoliated graphene as a filler and a mixture of two different polymers as a matrix. Several variables have been changed with the purpose of enhancing the sensors' electromechanical properties by combining mechanical properties of both polymers and conducting characteristics of graphene. For this reason, a statistical program (Design of Experiment, DOE) has been used to "design the experiment" by finding the optimum combination of the variables involved.^{31,32}

Furthermore, using a prediction profiler of the aforementioned program, it was possible to define the relationship between the variables used in the experiment and improve the responses important in sensing materials such as hysteresis and gauge factor. Through our endeavour to model these dispersions, reviewing the main findings in sensing applications, and profiling complex polymeric systems through statistical analysis, it is hoped that this work will provide a richer picture of TMDs' characteristics and piezoresistive materials for future developments.

1.2 THESIS OUTLINE

Chapter 2 – Introduction and Background Theory

Here, a general idea of the theory behind the completed work is given. The 2D material properties and solubility parameters are introduced along with the exfoliation process. Also, an overview concerning composites and sensing materials is explained. The electromechanical properties of materials ranging from

the Young's modulus definition to piezoresistivity description are explained. Finally, a brief summary about the design of experiment and the principles that brought on the development of this concept is described.

Chapter 3 – Materials and Methods

The chapter comprises the materials, the sample preparation process and the characterization used during the course of this work. A brief description of the equipment used during electromechanical testing is also presented.

Chapter 4 – WS₂ Exfoliation via High Shear Mixing

In this chapter, shear mixer exfoliation is explained, results are reported of the experiments conducted, and the technique to create a scale-up equation that can describe the efficiency of this preparation method, is presented.

Chapter 5 – Negative piezoresistivity of PEO/MoS₂ nanocomposites

In this part of the thesis, the technique of how TMDs are prepared via liquid phase exfoliation is presented. These particular TMDs are introduced into a polymeric matrix and the resulting composite is used for strain sensing applications. We focus our attention on molybdenum disulphide and polyethylene oxide. Here, the polymer acts as a dopant, increasing the conductivity of MoS₂. Furthermore, it is shown how the stress is transferred into MoS₂ nanosheets at small strain, modifying the band gap and giving them the characteristic negative gauge factor. Lastly, a model has been developed to describe all these observations and we compare several materials including tungsten disulphide, molybdenum diselenide (MoSe₂), tungsten diselenide (WSe₂), and graphene.

Chapter 6 – Experimental Design (DOE)

Complex systems require long periods of research and the higher the number of variables involved in the experiment, the higher are the number of samples necessary to perform the experiment following the scientific method. Due to this, an experimental design program is used in this work referring to a statistical program which considers the variables involved in the experiment (i.e. graphene, PDMS, boric acid concentration) and then predicts a profile with the purpose to

obtain high elastic strain sensor performances (i.e. low hysteresis and high gauge factor).

Chapter 7 – Conclusions and Future Work

This thesis concludes with the main findings and suggestions for possible forthcoming research.

Introduction and Background Theory

2.1 INTRODUCTION

As demonstrated from innumerable articles, paper, and theses before this work,^{16,33–40} graphene marked a new era from 2004 when Geim and Novoselov demonstrated the possibility of separating free-standing graphene monolayers.⁴ This enormous step signified a rebirth of nanoscience and, thanks to graphene's incredible mechanical⁴¹ and electric⁴² properties, this led to a blossoming of a new interest in another class of materials: layered (2D) materials.^{4,43} The peculiarity of this category is the presence of stacked nanometric sheets, one on top of another, bound by weak Van der Waals or interactions. This structure allows electrons to move in a 2D plane and thus allows us to create a series of applications, ranging from optical devices,⁴⁴ energy generation and storage,⁴⁵ chemical sensors⁴⁶ and high speed electronics.⁴⁷ Two dimensional materials, with nanoscale dimensions, exhibit improved optical, electrical and mechanical properties that make the difference in the field of nanomaterials and nanodevices. A class of compounds that have been the subject of interest over the last few decades is the Transition Metal Dichalcogenide (TMD) category.^{11,40,48,49} A TMD is a combination of two elements: a transition metal of group 4 – 10 and a chalcogen such as sulphur, selenium or tellurium. In general, compounds with transition metals in the group 4 – 7 have a layered structure, and those with the metal in the group 8 – 10, have a non-layered structure (one exception is PtSe₂). Furthermore, materials with Molybdenum (Mo) and Tungsten (W), such as MoS₂, MoSe₂, WS₂, and WSe₂ (Tungsten Diselenide), have phases that have been identified as semiconducting.⁵⁰ These materials have been investigated for their properties and their importance in commercial applications.^{19,51–54} For example, their band structure changes when moving from the bulk crystal to a single layer material, and this gives peculiar electronic characteristics (i.e. high carrier mobility, sizable bandgaps,

photoluminescence) to the material useful for applications such as batteries^{24,45,55} or sensors⁵⁵⁻⁵⁷ and some of these important applications will demand industrial-scale production.²⁰ For this reason, it is important to find a method which leads us to large scale, defect free production of 2D nanomaterials (i.e. without oxidation reactions). Regarding mechanical properties, the AFM analysis of MoS₂ with the number of nanosheets between 5 and 25, shows high Young's modulus (0.33 ± 0.07 TPa) and 1 or 2 layers of MoS₂ have been found broken, but highly crystalline and defect-free.⁵⁰ Due to its excellent semiconducting properties, single-layer MoS₂ nanosheets are suitable for a variety of applications such as flexible electronic devices.^{34,58,59} Furthermore, the thickness dependent band gap of MoS₂ nanosheets is seen as an important characteristic that can be exploited for optoelectronic devices.⁶⁰ Thanks to the space between the S-W-S sheets, WS₂ is an excellent candidate for intercalation reactions and, therefore, for high energy density battery production.⁴⁵ Moreover, the performances of single and bilayer WS₂ transistors have been studied, finding their electronic transport properties interesting and suitable for this kind of application.⁶¹

Despite their properties, these materials are not widely used because most of their exfoliation methods are not scalable (i.e. scotch tape method; Chemical Vapour Deposition (CVD)). Applying these methods, it is possible to obtain material with a good yield and crystallinity, but it is not possible to scale these methods up for industrial quantities. A more suitable method that can lead to the achievement of a large amount of nanomaterial is liquid phase exfoliation (LPE).⁶²

LPE is an efficient technique for dispersion and exfoliation of several layered nanomaterials. It is a top down method where a layered material is immersed in a liquid, a solvent or aqueous surfactant, then, ultrasonic agitation supplies energy for cleaving the layers of the material.¹⁸ Liquid exfoliation through sonication gives defect-free nanosheets, but the scalability of this process is restricted by the low yield and the high amount of energy this technique requires. One possible alternative to sonication would be high-shear mixing.

Shear mixing is already widely used to exfoliate a variety of layered material.^{20,63} A recent work demonstrated the efficiency of this method in exfoliating large amounts of graphite to give defect-free graphene nanosheets that can be scaled up to an industrial level.²⁰

This work shows successful implementation of a technique to exfoliate massive quantities of defect-free WS₂ (**Chapter 4**); this technique is known as shear mixing exfoliation. As the name suggests, the exfoliation occurs by shearing the 2D materials via two main parts: a four blade rotor and a stator. We demonstrate that the theory describing shear exfoliation of 2D materials in the liquid phase can be applied not just to graphene as previously reported, but also to other materials. In this work we focus our attention on one material of interest (WS₂) and, through varying processing parameters, demonstrate that scalable production of WS₂ can in fact be performed using high shear mixing.³⁰

Even though research in liquid exfoliation has a lot to offer, our work was not solely intended to focus on the shear exfoliation of TMDs, rather it wanted to be pushed towards the application work, specifically, on strain sensors (**Chapter 5**).

Over the last 20 years, the need for the next generation of sensing materials increased exponentially across different areas of material science.^{14,34,45,46,64–67} Lately, finding biocompatible materials has been necessary to develop wearable sensors for monitoring biological functions such as blood pressure and pulse^{13,68,69} and in detecting brain seizures.⁷⁰ This interest has moved toward soft and stretchable materials, basing the research on nanocomposites and nanostructured sensing materials. In general, strain sensors are part of a category called “*Smart (or intelligent) Materials*”. The adjective “smart” implies that the material subjected to an environmental change has a predetermined response (i.e. multi-response hydrogels which change their shape as a function of temperature or pH)^{71,72} which make them suitable for drug delivery,^{73–75} interactive electronics^{76–78} and self-powered devices.^{79,80} Usually, strain sensors are based on piezoelectric materials^{14,65} which are a class of both organic (i.e. polymers) and inorganic materials that naturally generate an electric potential difference.⁸¹ However, another family of strain sensors that behave similarly to piezoelectric materials are piezoresistive sensors for which they base their operating principle on the piezoresistive effect from elastic deformation. The piezoresistive effect involves a change in the resistance ($\Delta R/R_0$) of an electric conductor such that^{59,82}

$$\Delta R / R_0 = G \varepsilon$$

(1.1a)

where G is the gauge factor and ε is the strain applied. Usually, the gauge factor is measured at low strain and in that limit it can be shown that⁶⁸

$$G = \frac{1}{\rho_0} \frac{d\rho}{d\varepsilon} + (1 + 2\nu)$$

(1.1b)

where ν and ρ are the Poisson ratio and resistivity of the piezoresistive material, respectively, and ρ_0 is its zero-strain resistivity. While for most metals, $d\rho/d\varepsilon$ is small leading to gauge factors in the range 2-4,⁸² for many semiconducting materials, $d\rho/d\varepsilon$ can be large, resulting in relatively high values of G .⁸³ This is generally attributed to quantum mechanical tunnelling between conductive particles which can lead to very high values of $d\rho/d\varepsilon$ and so G .⁸⁴ For example, p-type silicon displays a gauge factor of up to 175.⁸² Similarly, composite strain sensors based on polymers filled with conductive nanomaterials, such as nanotubes or graphene, can display very high gauge factors.⁸⁵⁻⁸⁸ For example, polysilicone-graphene composites have recently been reported with gauge factors above 500.⁶⁸ This implies that when a material is subjected to tensile strain, the resistance increases as well, resulting in a positive gauge factor. This is due to the fact that the piezoresistance in composites is dominated by tunnelling effects which lead to $G > 0$. While this is true for the vast majority of materials, there exists a class of materials which reports negative gauge factors. Negative piezoresistance is when resistance decreases with increasing tensile strain. This peculiar phenomenon offers the possibility to relate the dependence of band structure on the strain and this can be harnessed to produce novel sensors. Commonly, negative gauge appears in n-type materials⁸² (e.g. nickel polymeric composites with $G = -12$); this is due to strain-induced conductivity enhancement. In other interesting studies, conductive aluminium nitride films deposited on Ti//Ru electrodes have been reported; the

interaction at the Ru//AlN interface has an effect on the value of the piezoelectric response.⁸⁹ In addition, SiC, Ge and GaAs also have reasonably high negative values of G .⁸² However, most interestingly for this work is the fact that the band gap of the 2-dimensional semiconductor MoS₂ (i.e. the 2H polytype) tends to fall with strain,^{90,91} leading to negative gauge factors ranging from -225 for bilayer MoS₂, to -50 for few-layer MoS₂.^{58,92} To the best of our knowledge, no composites of polymers filled with semiconducting particles have been reported with negative G for two main reasons. Firstly, due to the low conductivity that a polymer filled with semiconductors implies. Secondly, even if such studies were made using negative piezoresistive particles, it is difficult to transfer an applied strain to the filler particles. Consequently, applied strain causes the motion of the adjacent fillers, rather than deforming the particles; while, the particle deformation would change the band gap and reduce the particle resistance.⁹³

Considering what mentioned above, the gauge factor represents a key parameter to determine the quality of a sensor; thus, improving this characteristic would lead to better sensing performance. However, another important characteristic is the hysteresis - both mechanical and electrical. Hysteresis comes from the Greek *husteros* which means late and in general; it is the phenomenon that describes a lag between input and output in a system upon a change in direction of the input.⁹⁴ This phenomenon can be related to several systems, i.e. when a material is subjected to a mechanical cyclic loading/unloading process ideally this would lead to the same deformation. The discrepancy in the stress values of the material during this cyclic process is called mechanical hysteresis.⁹⁵ In other words, the smaller the hysteresis, the better the elastic recovery of the material will be. The hysteresis can be defined as a dimensionless quantity and the value can range from 0 to 1, or it can be expressed in percentage.^{96,97} In other words, a strain sensor with hysteresis value equal to 0 means that it maintains the same performances overtime; for this reason, one of the goals, when fabricating a strain sensor, is to both maximise the gauge factor and minimise the hysteresis. In order to do so, several fabrication methods have been used over the past decade^{98,99} which in general can be divided into two categories: where a polymeric substrate is coated with conducting fillers;¹⁰⁰⁻¹⁰⁴ these types of strain sensors usually use nanowires as conductive filler (i.e. AgNW,¹⁰⁵ CNTs,¹⁰⁶ etc.) and a stretchable polymer as support such as

polydimethylsiloxane (PDMS)^{107,108} or polyurethanes (PU).^{109,110} A problem with these types of strain sensors is the filler cracking, which occurs after several cycles, and the consequent detaching from the substrate. Another option that would avoid this problem is preparing strain sensors where the conductive filler (or conductive polymer) is embedded within a polymer matrix;^{111–116} here it is possible to combine and control the properties (mechanical and electrical) of both polymer and filler but it is necessary to consider the interactions between these two in order to optimise their characteristics and obtain high gauge factor and low hysteresis. However, this has been challenging to achieve and a way to do so is combining more than two components. In this way, we can create a complex system that can be modulated in order to obtain the expected results. Nonetheless, more variables imply also more testing to perform thus, more time and money to spend on the experiment. One solution could be the use of Design of Experiment or experimental design (DOE).^{117–119} Design of experiment is a method which harnesses statistical calculation regarding a specific experiment in order to predict the best results achievable from that experiment.¹²⁰ With this method it is possible to predict the desired results (called “responses”) of an experiment through statistical analyses. In order to use this method in the most appropriate way, we need a pre-phase. Here, the variables necessary to perform the experiment (referred to as “factors”) are defined and a specific range of values of the variables is specified in the program. This technique, commonly used in industries, represents an efficient way to perform every kind of experiment in a broad range of fields; from the realization of chemical reactions,^{121,122} to the optimization of devices used in renewable energy^{123–128} or to improve biomedical materials’ performances.^{129–132}

2.2 GRAPHENE AND LAYERED MATERIALS

As previously mentioned, the discovery of graphene represented a breakthrough in material science. Graphene is simply a mono-atomic sheet of sp^2 hybridised carbon atoms arranged in a honeycomb lattice. These sheets stacked one on top of each other and bonded with Van der Waals forces, form the 3D crystal known as graphite. Even though the term graphene is referred to a single layer, this term can be used also for few-layers graphene (2-5 layers)⁴⁶ inasmuch as it presents similar

properties to the single-layer one.^{4,18,133} However, graphene is an allotropic form of carbon as well as fullerenes (hexagonal and pentagonal units connected together in a spherical shape)² and carbon nanotubes (graphene sheet wrapped to form a tube)^{39,84,93} (**Fig.2.1**). Graphene has exceptional properties, including: high value of Young's Modulus close to that of diamond, high breaking strength, high specific surface area, and very high thermal and electrical conductivity.^{33,41} Electrons can move in the graphene lattice without encountering obstacles and this allows for a much higher mobility than the one present in metals or semiconductors (**Fig.2.2**).¹³⁴ Thanks to these properties, the potential applications are innumerable; some applications are: energy storage,¹³⁵ electronics, production of transistors components and microchips,²⁸ optics,^{33,47} biomedicine^{16,70} and production of nanocomposite materials,^{136–138} the latter of which aligns most closely to our interests.

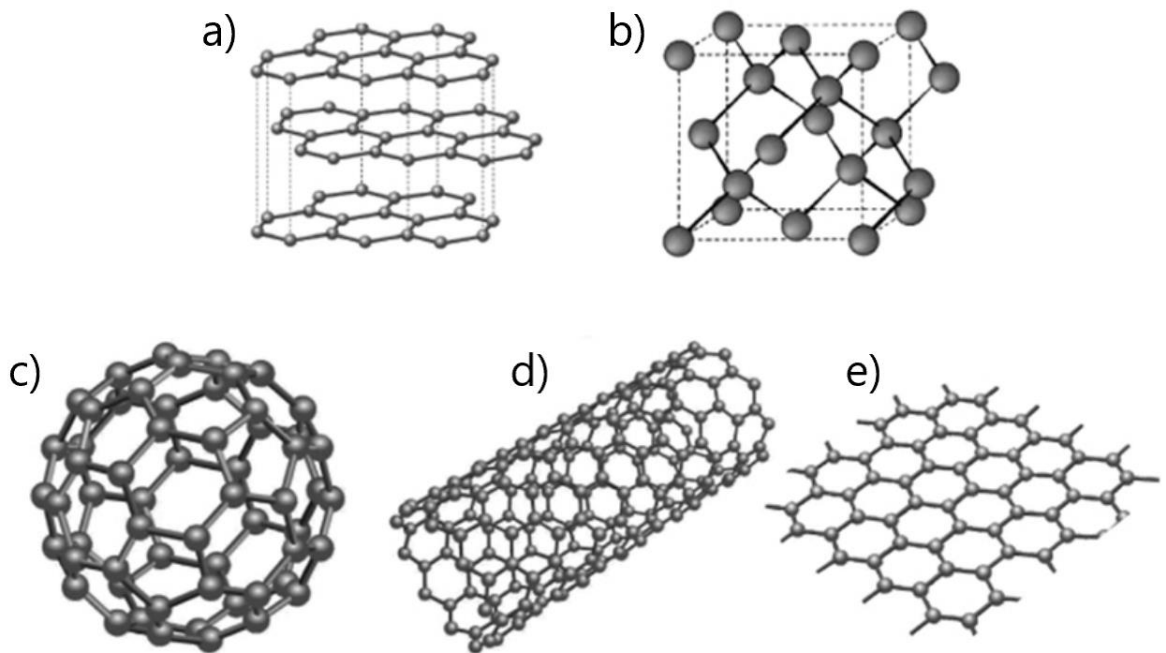


Fig.2.1. Some of the allotropic forms of carbon: a) graphite, b) diamond, c) fullerene, d) carbon nanotubes, and e) graphene³⁵.

Furthermore, its peculiar band structure allows for particularly important electrical and optical effects. For example, one phenomenon observed on a graphene flake is "*ambipolar ballistic transport*". The ambipolar effect consists of both electrons and holes conduction from a material and this characteristic causes the inversion of the sign of the charge carriers as a function of the sign of the applied voltage.¹³⁹ A graphene flake was inserted into a device with several Hall-type terminals and has demonstrated extraordinarily high carrier mobility values (between 3,000 and 10,000 cm² (V·s)⁻¹ up to 10⁵ cm² (V·s)⁻¹ if the concentration of impurities is limited). Unlike traditional semiconductors, these mobility values do not decrease at high concentrations of charge carriers (> 10¹² cm⁻²) leading to a ballistic-type transport, so called because the carriers move in the lattice without scattering over sub-micrometric distances (up to ~ 0.3 μm at 300 K).⁴² Moreover, the high thermal conductivity of graphene (5000 W·m⁻¹·K⁻¹)³⁸ was found to be even hundred times higher than that of copper (401 W·m⁻¹·K⁻¹), known as the bulk material with the highest thermal conductivity.³⁸ Graphene combines the peculiarity of being an extremely light material (density equal to 0.77 mg / m²) with exceptional mechanical strength properties (it is estimated a tensile strength around 42 N / m and Young's modulus around 1 TPa); if compared to steel, for example, it is a hundred times stronger.^{33,41} Among the many features, there is the high flexibility and fragility (it is able to form folded structures but for high loads, it fractures as if it were a glassy material), and the ability to stretch up to 20% compared to its initial length.⁴⁴

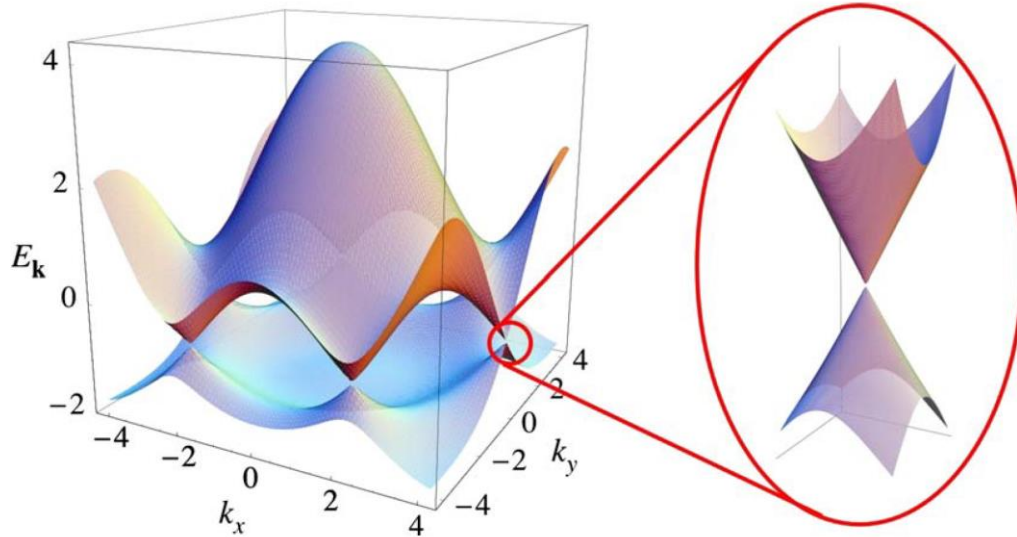


Fig.2.2. Band structure in the honeycomb structure of graphene. We can see that the energy at the Dirac points is zero and because it is gapless, graphene is considered a semi-metal.¹³⁴

2.2.1 Transition Metal Dichalcogenides (TMDs)

Although graphene's superior properties produced countless studies of this material, there are also other layered materials that deserve attention. In recent times, the attention has been drawn to other 2D materials such as boron nitride (BN),¹⁴⁰ black phosphorus or phosphorene (BP),³⁴ transition metal oxides (TMOs)¹⁴¹ and transition metal dichalcogenides (TMDs)¹⁴² (**Fig.2.3**). Despite the fact that graphene and BN show analogous structures where BN presents sp^2 bonded sheets of alternated boron and nitrogen atoms, this molecule is an electrical insulator. This property opens a set of applications different from graphene.¹⁴⁰ Compared to graphene and BN, BP has a very dissimilar structure. Although BP is included in the class of layered materials, it has a wrinkled orthorhombic structure where one phosphorus atom is covalently bonded to three other adjacent phosphorus atoms.^{34,54} One of the peculiarities that make BP attractive for electronic devices, is the tunability of its bandgap which can change from 0.3 eV to 1.8 eV, depending on the number of layers stacked.¹⁴³ TMOs are a class of compounds where transition metal atoms are bound to oxygen atoms. Their ability to change metal-oxygen ratios gives them a broad structural variety and,

consequently, some diverse properties.¹⁴⁴ Usually used for their catalytic activity and their semiconductive properties, TMOs can be used in photo-assisted processes^{145–147} or electronic devices.^{148–150}

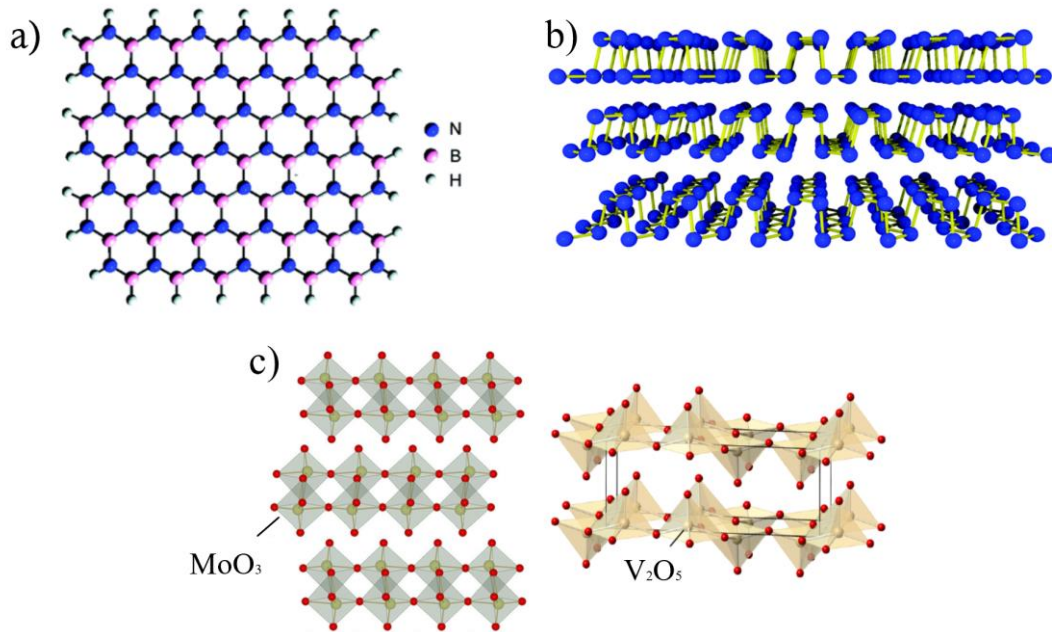


Fig.2.3. Structure of a) Boron Nitride,¹⁵¹ b) Black Phosphorus¹⁵² and c) some examples of Transition Metal Oxide compounds (MoO₃ on the left and V₂O₅ on the right).¹⁵³

Although all these layered materials have remarkable characteristics suitable for a large variety of applications, this work has been focused on the study of TMDs. These compounds have been known for a long time, but it was just after graphene exfoliation in 2004 that there has been a renewed interest in them. Despite their similar structure to the other 2D materials, TMDs properties cover a broad spectrum ranging from insulator to semiconductor, to metal.^{154–157} As mentioned before, TMD is a combination of a transition metal of group 4 – 10 and a chalcogen. materials with Molybdenum (Mo) and Tungsten (W) as part of their structure such as MoS₂, MoSe₂, WS₂, and WSe₂ (Tungsten Diselenide) have been identified as semiconducting materials (**Fig.2.3**).¹⁵⁸

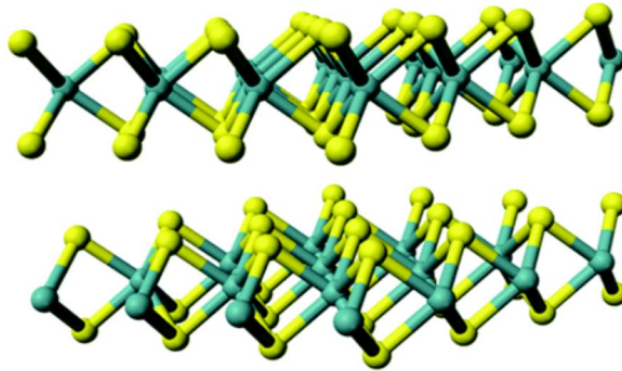
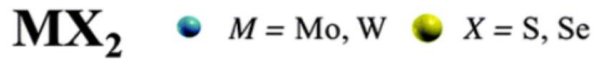


Fig.2.4. Representative structure of TMDs.¹⁵⁹

The band structure for these compounds changes drastically going from the indirect gap in bulk samples to the direct gap in single layer nanosheets (**Fig.2.5**).¹⁶⁰ This affects the electrical and optical properties which depend on the numbers of layers, especially for samples with less than five layers.¹⁵⁵

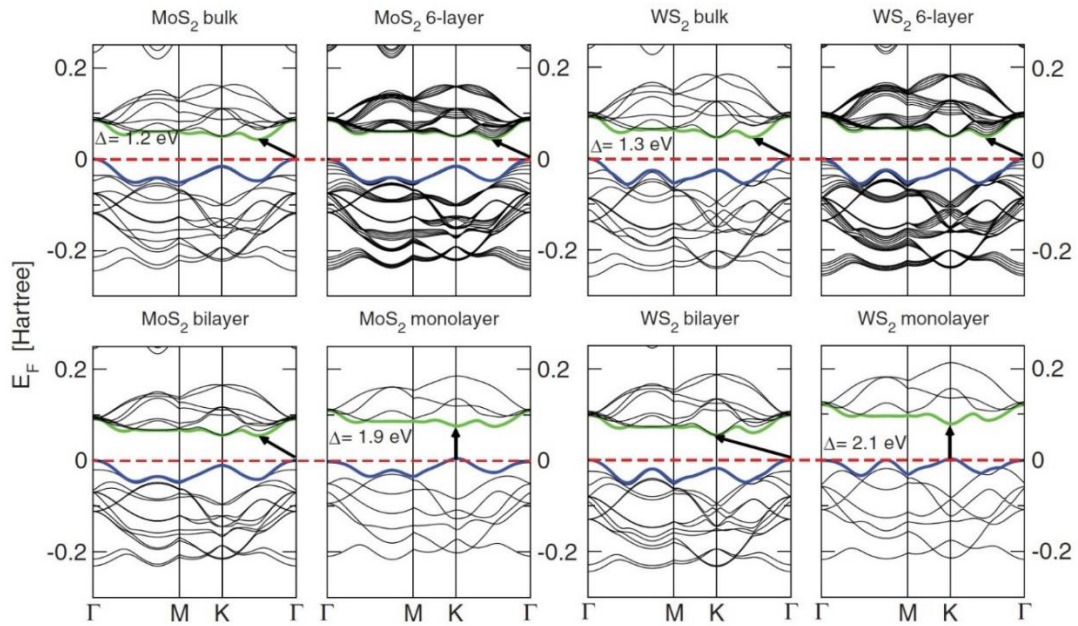


Fig.2.5. Band structure of both MoS₂ (on the left) and WS₂ (on the right) from bulk crystal to monolayer demonstrating the how they change with exfoliation.¹⁶⁰

Their electrical properties are very sensitive to external factors such as temperature, strain and pressure.¹⁶¹ Moreover, the presence of defects in the form of vacancies, adatoms and boundaries can lead to fascinating magnetic properties.^{58,61,157} There are about sixty TMDs where just a third does not have layered structure,¹⁶² mostly are synthetic but, a good portion exists in nature such as MoS₂ in its forms 2H and 3R (here the numbers represent the number of layers in the unit cell of the compound and the letters H and R specify the symmetry, i.e. H = hexagonal, R = rhombohedral, T = trigonal, **Fig.2.6**). These polymorphs can be stacked or arranged in 3 different polytypes.¹⁶²

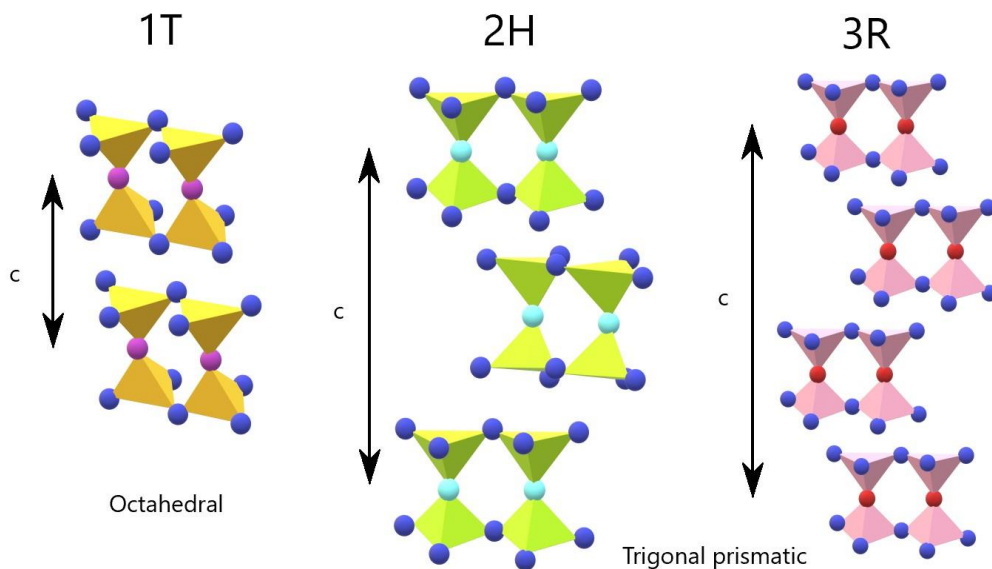


Fig.2.6. Schematic of the structural polytypes of TMDs from left to right **1T** (tetragonal symmetry with octahedral coordination of the metal and one repetition of the layer), **2H** (hexagonal symmetry with trigonal prismatic coordination of the metal and two repetition of the layer), **3R** (rhombohedral symmetry with trigonal prismatic coordination of the metal and three layers per repeat).

The change of thickness of TMDs not only has an effect on electronic properties, but also on the optical properties, and both layer number and lateral dimension of the nanomaterial affect absorption and the extinction spectrum

respectively.^{10,11,48,163} Previous work done by Backes *et al.*, relates qualitatively and quantitatively the extinction spectra to specifically the MoS₂⁴⁸ and WS₂¹¹ length and thickness, developing metrics for these materials exfoliated via liquid phase exfoliation. Indeed, the atoms at the edges of the flakes have different effects on the local absorption coefficient, thus the optical absorption. When the length of the nanosheet is reduced, the ratio of edge to central atoms increases, causing a change of the spectral shape. Regarding the thickness of the material, it has been previously demonstrated that if we reduce the number of layers, we confine the electrons into a 2D space; this change can be observed in the optical spectrum through the shifting of A-exciton (defined as electrically neutral quasiparticle commonly presents in semiconductors which is able to transport energy without a charge transport) as well as the extinction spectra.^{10,11,17,19,48}

2.3 EXFOLIATION OF 2D-MATERIALS

Over the years since 2004, several synthesis approaches have been developed with the purpose of improving both processing quality and quantity of 2D nanosheets.^{24,33,158,164,165} These methods can be broadly classified into bottom-up or top-down, depending on how the monolayer is obtained. Briefly, the starting materials of the bottom-up approach are atoms and molecules which self-assemble into building blocks and subsequently into a nanostructure through physical and chemical interactions;^{166,167} one example is the Sol-Gel method (**fig.2.7**). This technique is generally used to prepare 2D materials, in particular metal oxides, as well as oxide composites.¹⁶⁸⁻¹⁷³ The Sol-Gel method is a wet-chemical process where the metal precursor of the nanoparticles is immersed in a liquid forming colloidal suspension (Sol) first and subjected to a gelation process afterwards (Gel).¹⁷⁴ This method comprises few steps before obtaining the final product:

- Hydrolysis step (**fig.2.7a**). Here, the formation of metal hydroxide occurs.
- Condensation step (**fig.2.7b**). A condensation reaction leads to a gel formation.

- Drying process (**fig.2.7c**). In this step the final product can be obtained through evaporative drying (forming a Xerogel), or through supercritical drying (forming an Aerogel).¹⁷⁴

Moreover, the Sol-Gel can be divided into two categories; aqueous Sol-Gel^{172,173,175} which consists of the use of water as solvent and non-aqueous Sol-Gel, where an organic solvent replaces water as solvent.¹⁷⁶ In several cases, especially for the aqueous Sol-Gel, the key steps of hydrolysis, condensation, and drying process take place at the same time causing a difficult morphology control and repeatability of the protocol.^{168,170,171}

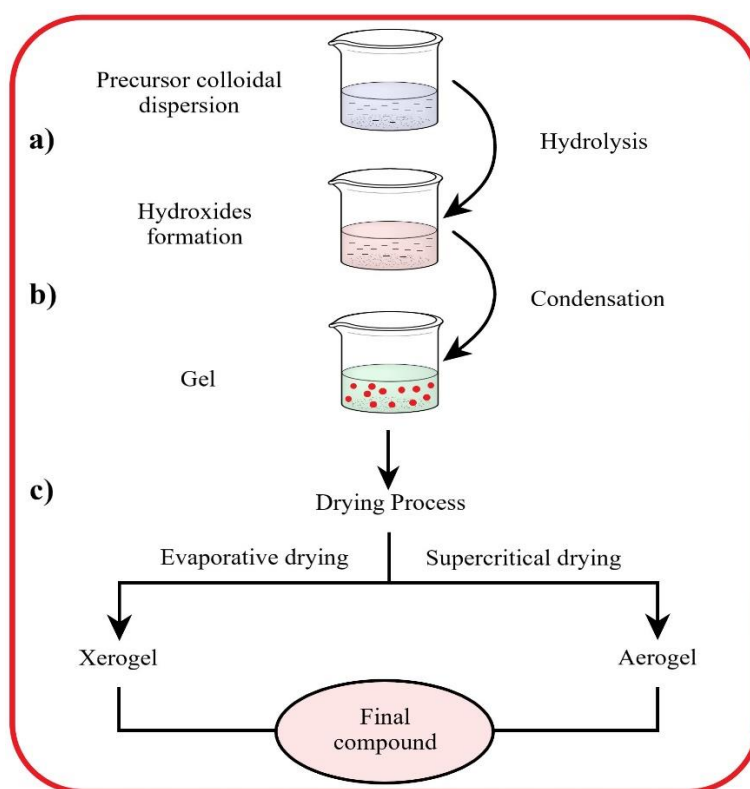


Fig.2.7. Graphic representation of the Sol-Gel method.

Another important method for bottom-up synthesis of 2D materials is chemical vapour deposition (CVD). This method allows the synthesis of single layers of 2D materials on a dielectric substrate. In the particular case of graphene, the method exploits the decomposition of hydrocarbons (i.e. methane) in the presence of catalysts (typically) on thin copper layers pre-deposited on a dielectric substrate.

The copper layers are subsequently evaporated, leaving a single layer of graphene on the surface of the dielectric material.^{164,177} It has been successfully demonstrated that it is also possible to obtain TMD nanosheets using a slightly different synthesis method. Indeed, instead of hydrocarbons, this process involves heating a metal oxide precursor (**Fig.2.7**).¹⁷⁸ Chemical methods offer the advantage of control over both nanosheet size and thickness, creating good quality monolayers; however high-yield electronic device production requires an alternative method of production which is more scalable than CVD or Sol-Gel.

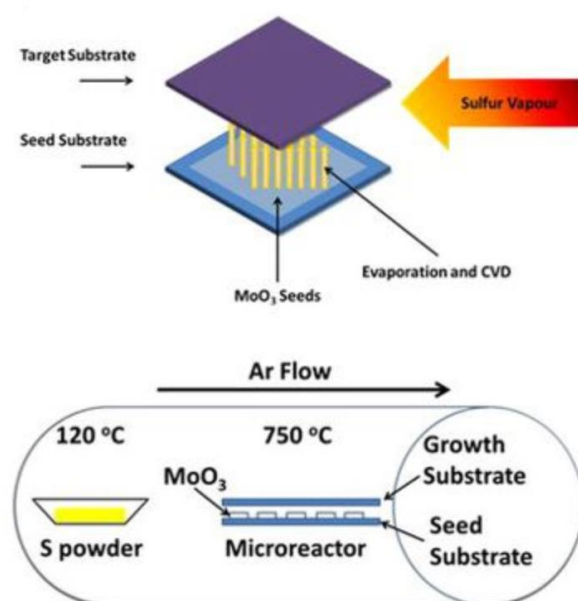


Fig.2.8. Graphic demonstration of 2D-nanosheet production through chemical vapour deposition (CVD).¹⁷⁹

In comparison, the top-down method utilises macroscopic initial structure (bulk crystal) and the exfoliation can be externally controlled in the processing of the nanostructure. This can be obtained using several synthesis strategies such as mechanical exfoliation, ion intercalation or liquid phase exfoliation.^{11,18,54,134,180,181} While mechanical exfoliation has been used since the early 60s using the simple Scotch[®] tape method to separate a thin layer of material from the bulk crystal,¹⁸² it was not until just after 2004 that this approach was expanded to effectively include graphene. This simple method involves the adhesion of tape onto the surface of graphite and as it is pulled away, there is a transfer of stress to the sheets and the

mechanical energy overcomes the weak Van der Waals forces between the layers. Despite the fact this method enables the production of high quality monolayers, the method has a very low yield which means scalability is not a possibility.⁴

2.3.1 Liquid Phase Exfoliation

The need to find an ideal method that can lead to both high quality nanomaterials with the ability to control their size, thickness, flake orientation, as well as an easy and cheap processing technique, has been the main objective of research in this field. For the scope of this work (which aims to use 2D-materials in electronic devices), it is very important to find a method that comprises all these features. In fact, the presence of defects in the material can affect the electric properties (i.e. conductivity) resulting, consequently, in poor performances of the electronic device. However, none of the techniques developed to-date have been able to combine all these characteristics; nevertheless, the possibility of high yield and high quality nanosheets have made the liquid phase exfoliation process very appealing in the 2D research world. This liquid phase exfoliation (LPE) process was demonstrated for the first time in 2008 by Hernandez *et al.*,¹⁸ when the achievement of exfoliated graphene from graphite through ultrasonication was shown (**Fig.2.8**). The graphite powder was dispersed into a specific solvent (N-methyl pyrrolidone) to prevent the reformation of the hydrogen/Van der Waals bond once exfoliated, and thus, reaggregation of the nanosheets.¹⁸

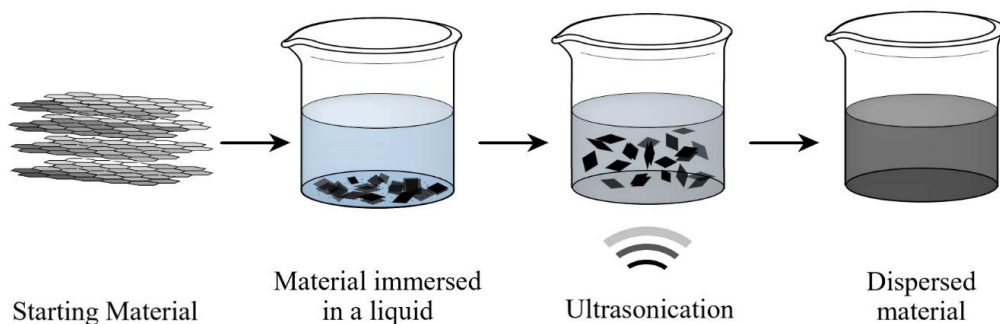


Fig.2.9. Classic representation of Liquid Phase Exfoliation.

In the paper mentioned above,¹⁸ it was shown how it is possible to harness nanosheet-solvent thermodynamics (section 2.3.2) to achieve high yield and quality of the exfoliated material. This technique is extremely versatile and since its first use, it has progressed significantly to exfoliate other layered materials such as TMDs, TMOs, hBN, BP, hydroxides (Fig.2.9), etc.¹⁹



Fig.2.10. *Various dispersed materials obtained via LPE over the years.*¹⁹

Furthermore, not only has it been possible to exfoliate a large range of 2D materials, but through the years, this method has been refined through different liquid medium studies.^{183,184} This includes not just common solvents, but also the use of water and surfactant.^{23,49} In general, the solvent or surfactant choice is based on Hildebrand solubility parameters, which roughly can be defined as the measure of how well solute and solvent interact with each other. Basically, if the surface energy of the nanoparticle is very different from the solvent or surfactant reaggregation will occur,^{185,186} thus, a careful system choice is necessary to obtain an optimal result. It is important to emphasize that, over time, the research has been extended to the use of several types of exfoliating machinery that can be included in this synthesis approach. This machinery started with a sonic bath^{23,136} for exfoliation and began to include such devices such as a sonic tip increasing yield and reliability,¹⁸ a kitchen blender,¹⁸⁷ and a shear mixer,²⁰ with the latter producing a good and scalable alternative for 2D nanosheet production (Fig.2.10).

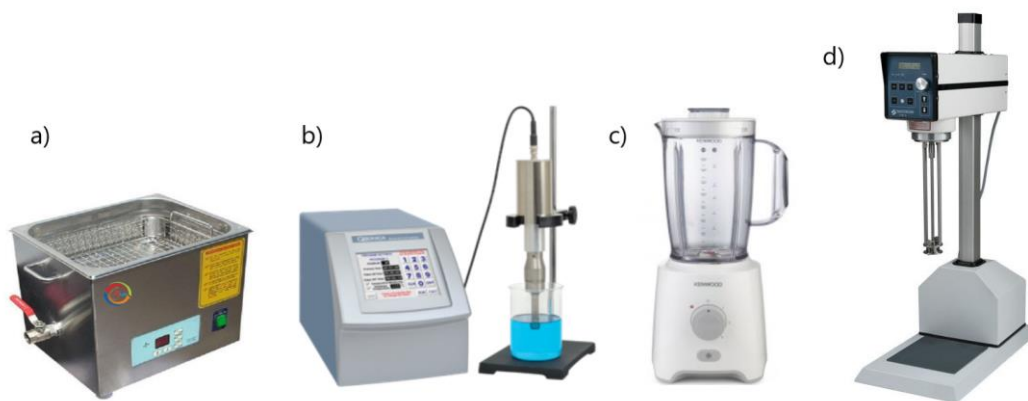


Fig.2.11. *Examples of machines used in LPE: a) sonic bath, b) sonic tip, c) kitchen blender and d) shear mixer.*

While the use of both ultrasonication and shear mixing leads to a high amount of defect-free nanosheets which make them appealing for electronic applications, the polydispersity of exfoliated material obtained by these techniques is too high to be effectively used immediately after the ultrasonication and/or the shearing. For this reason, this process is usually accompanied by following specific centrifuging steps which separate the nanoparticles based on their weight and thus on their dimension.^{10,19,188} One of the main benefits of LPE is the fact that nanomaterial production takes place in a liquid. This allows the material to be easily processed into inks for aerosol deposition and inkjet printing,¹⁸⁹ from which point it is possible to produce supercapacitor electrodes¹⁹⁰ or transistors²⁸ through simple deposition of the material. Also, this makes it suitable for multi-component composite manufacturing¹³⁶ which can be used in applications such as biomedical device preparation.¹⁶ Moreover, thanks to this technique, it is possible to exploit simple spectroscopy like UV-vis and Raman analysis to obtain information regarding the quality and both lateral size and thickness of the material. Indeed, an in-depth investigation on metrics has been carried out over past few years which are able to describe and relate the material characteristics to a large set of variables (from the sonication/shearing time and volume to the centrifugation speed and starting material concentration). This has been successfully realized for a big variety of nanomaterials, ranging from TMDs and graphene^{18,51,163,191} to layered oxide⁵² and hydroxide compounds.¹⁹²

2.3.2 Dispersion Theory

As previously mentioned, a careful choice of solvent (or surfactant in the case of aqueous dispersions) is necessary to obtain a good dispersion where the material is not just exfoliated but also stable in the liquid medium without reaggregation. To achieve this, a theory that describes both the physics and the chemistry behind the liquid exfoliation process has been developed from Coleman's work.^{18,193} The dispersion theory is a fundamental part of liquid phase exfoliation, and it can be divided into two methods: one method considers the exfoliation through a solvent (Solvent Exfoliation Mechanism), and the other method studies the mechanism of the process using water/surfactant (Electrostatic Stabilising Mechanism or Surfactant Exfoliation). These two methods are analogous, and in this thesis, both methodologies are described.

Solvent Exfoliation. The stability of a solute in a solvent depends on two factors: the type of the solute and the nature of the solvent. In fact, nanomaterials with a certain structure can have different chemical interactions depending on the surrounding environment. In the case of TMDs, graphene or other layered materials, the forces responsible for their interlayer bonding are the Van der Waals dispersive forces. A theory developed by Hildebrand¹⁹⁴ and later developed by Hansen,¹⁹⁵ demonstrated that by matching Hildebrand solubility parameters of the solvent and the solute, it was possible to obtain a stable dispersion of the nanomaterial. Strictly speaking, we can assume (from Hamaker theory) that solute and solvent with similar surface energy gives a stable dispersion¹⁹⁶. Therefore, the interaction can be described very simply by analysing the Gibbs free energy of the mixture and, for ideal dispersions, ΔG_{mix} has negative values. This quantity is the combination of two factors: the enthalpy of mixing and the mixing entropy and is defined as

$$\Delta G_{mix} = \Delta H_{mix} - T \Delta S_{mix} \quad (2.1)$$

Here, T is the temperature, ΔH_{mix} is the enthalpy of mixing, and ΔS_{mix} is the entropy of mixing. For a negative ΔG_{mix} , we need to minimize ΔH_{mix} ; thus it is necessary to consider and include other important parameters. In fact, it is not sufficient to describe just solute-solvent interactions, but also solvent-solvent and solute-solute interactions. It is even possible to achieve a better understanding by applying the Flory-Huggins theory.¹⁹³ In this case, ΔH_{mix} can be described by:

$$\Delta H_{\text{mix}} = \chi\phi(1-\phi)kT / v_0 \quad (2.2)$$

Here, ϕ is the solute volume fraction, v_0 is the volume of one molecule and χ is the Flory-Huggins parameter. This parameter χ is defined as:

$$\chi = -\frac{z}{2} \frac{(2\varepsilon_{AB} - \varepsilon_{AA} - \varepsilon_{BB})}{kT} \quad (2.3)$$

Here, z is the coordination number of both solvent and solute and ε represents the inter-molecular pairwise interactions.

Looking at the equations (2.2) and (2.3), we notice several things. First of all, we have to take solute-solute and solvent-solvent interactions into account, not just solute-solvent interactions (represented in the equation (2.3) by A and B). Second, solute-solvent interactions are dominant if $\chi < 0$ while if $\chi > 0$, the solute molecules are attracted to each other causing aggregation of the nanosheets. This also means that the smaller χ is, the smaller ΔH_{mix} will be and, consequently, will promote a better dispersion.¹⁹³

However, it is common to express the parameter χ in terms of cohesive energy and use the Hildebrand solubility parameter¹⁸⁵ instead of the Flory-Huggins parameter. There are three main types of interactions that have to be considered in this case:

dispersive energy (E_D), polar cohesive energy (E_P) and the electron exchange parameter (E_H). The total sum of these parameters is the total cohesive energy (E),

$$E = E_D + E_P + E_H \quad (2.4)$$

The Hildebrand parameter is the sum of the squares of each Hansen parameter ($\delta = \sqrt{E/V}$, where V is the molecular volume).

$$\delta^2 = \delta_D^2 + \delta_P^2 + \delta_H^2 \quad (2.5)$$

Thus, it is possible to express χ in terms of Hansen parameter:

$$\chi \approx \frac{V_0}{kT} \left[(\delta_{D,A} - \delta_{D,B})^2 + (\delta_{P,A} - \delta_{P,B})^2 + (\delta_{H,A} - \delta_{H,B})^2 \right] \quad (2.6)$$

By matching Hansen parameters of solutes and solvents, it is possible to minimise $(\delta_A - \delta_B)^2$ and, consequently, minimise the mixing enthalpy encouraging dispersion stabilisation.^{193–195}

Surfactant stabilisation. In this work, exfoliation through (ionic) surfactant stabilisation has been adopted for dispersion preparation. Surfactants, which stands for “surface-active agents”,¹⁹⁷ are molecules composed of a hydrophilic head and a hydrophobic tail (**Fig. 2.11a**) and, for this reason, are defined as amphipathic compounds.

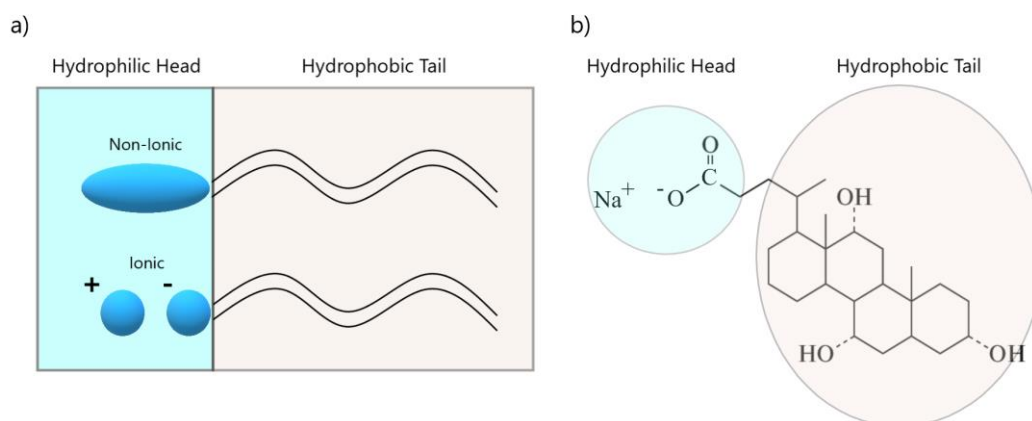


Fig.2.12. *Schematic representation of (a) surfactant and (b) sodium cholate molecule used in this work.*

Therefore, in LPE the hydrophobic tail will be attracted to the nanoparticle while the polar phase is solvated by the water. The most commonly used surfactants used in LPE are ionic compounds such as sodium cholate (SC or sometimes NaC, **Fig.2.11b**), sodium dodecyl benzenesulfonate (SDBS) both of which create a charge in the dispersion. This charge is balanced by a counter ion of the tail and it is large enough to prevent the reaggregation of the nanosheets (**Fig.2.12**).

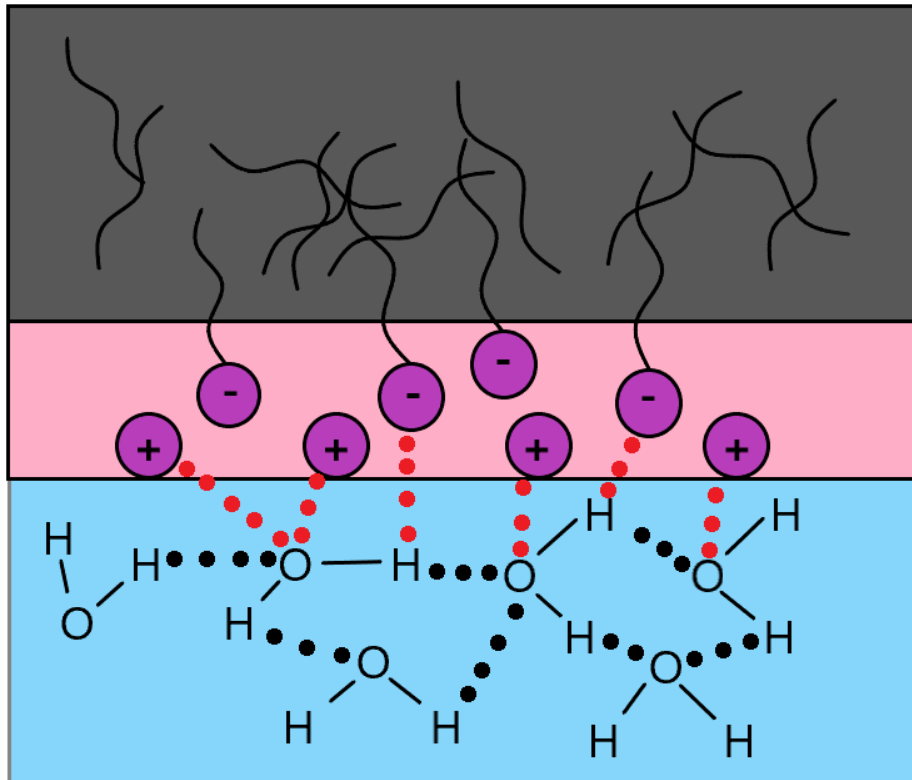


Fig.2.13. *Representative image of the nanoparticle surface (grey) stabilised by the surfactant (pink).*

This charge distribution around the nanoparticle produces a potential difference (electric double layer, EDL)¹⁹⁸ which can be described by the DLVO theory; the theory takes its name from people who studied this phenomenon (Derjaguin, Landau, Verwey, and Overbeek). DLVO theory assumes that for dispersed spherical particles with an equilibrium of attractive and repulsive potential energies, the attractive energies depend on Van der Waals weak bonds and the repulsive forces are influenced by the EDL. Consequently, to have a dispersion of the nanoparticles the EDL has to be greater than VdW forces. It is possible to describe this mechanism through the equation:

$$V = V_A + V_R \quad (2.7)$$

where the total potential energy, V , is the sum of attractive, V_A , and repulsive, V_R , potential energy. V_A for two spheres in vacuum, with radius r , at distance D can be expressed by

$$V_A = -\frac{Ar}{12D} \quad (2.8)$$

where A is the Hamaker constant.¹⁹⁶

V_R can be described by several factors. It depends not just on the size and the shape of the nanoparticles but also on the distance between them, and on the Zeta potential, ζ , which is the key indicator of the stability of a colloidal dispersion. The magnitude defines the potential at the nanoparticle surface and it indicates their repulsion degree. Moreover, V_R depends also on the dielectric constant of the liquid, ϵ_r , and the Debye screening length, κ^{-1} , which represents the effective thickness of the EDL¹⁹⁹

$$\kappa^{-1} = \left[\frac{\epsilon_r \epsilon_0 kT}{2e^2 n_0} \right]^{1/2} \quad (2.9)$$

where ϵ_0 is the permittivity of free space and n_0 is the concentration of the surfactant.

For two small particles with radius r when $\kappa r \ll 1$ then

$$V_R = \frac{\epsilon_r \epsilon_0 r^2 \zeta^2}{D} e^{-\kappa D} \quad (2.10)$$

So we can define the total potential energy with

$$V = -\frac{Ar}{12D} + \frac{\varepsilon_r \varepsilon_0 r^2 \zeta^2}{D} e^{-\kappa D} \quad (2.11)$$

From the equation above, we can say that the Zeta value has to be high in order to avoid reaggregation, typically around 30mV. Even though this model describes the potential for two spherical nanoparticles without considering the orientation effects or planar objects, it gives an idea of the mechanism and physical parameters involved in this process.

2.3.3 Shear Mixer Theory

Since the work in 2008 where the use of ultrasonication lead to well-dispersed graphene, several studies have been performed aiming to increase the scalability of 2D material exfoliation via LPE.^{9,20,21,187} Although, through the simple use of a kitchen mixer it was possible to obtain a high yield of graphene nanosheets,¹⁸⁷ it was actually the work by Paton *et al.* in 2014 that marked an important turning point in large-scale production.²⁰ Indeed, it was possible to apply shear mixing exfoliation not just to graphene but also to MoS₂, BN, and other layered materials.^{200–203} Moreover, the nanosheets obtained with this method have been incorporated into several systems, working well for both composites and conductive coatings.^{204,205} Shear exfoliation is a method which can be used in industrial production by just applying high shear rate to the bulk material.^{206–208} The shear mixer exploits rotating blades or alternative devices immersed in a liquid medium with the sample. Here, the rotating movement of the blades drives the nanoparticles in small precise gaps between the rotating and the stationary phase called the shearing region.^{209,210} Depending on the purpose of the experiment, it is possible to use different stationary phases (bottom of **fig.2.13**). For example, to exfoliate fibres it is possible to use the slotted disintegrated head while an emulsor screen can be utilised for emulsions.²¹¹ In this work, a rotor-stator mixer has been used (**Fig.2.13** top). The assembly is comprised of a frame, rotor with four blades, screen with 96 square holes and a base plate.

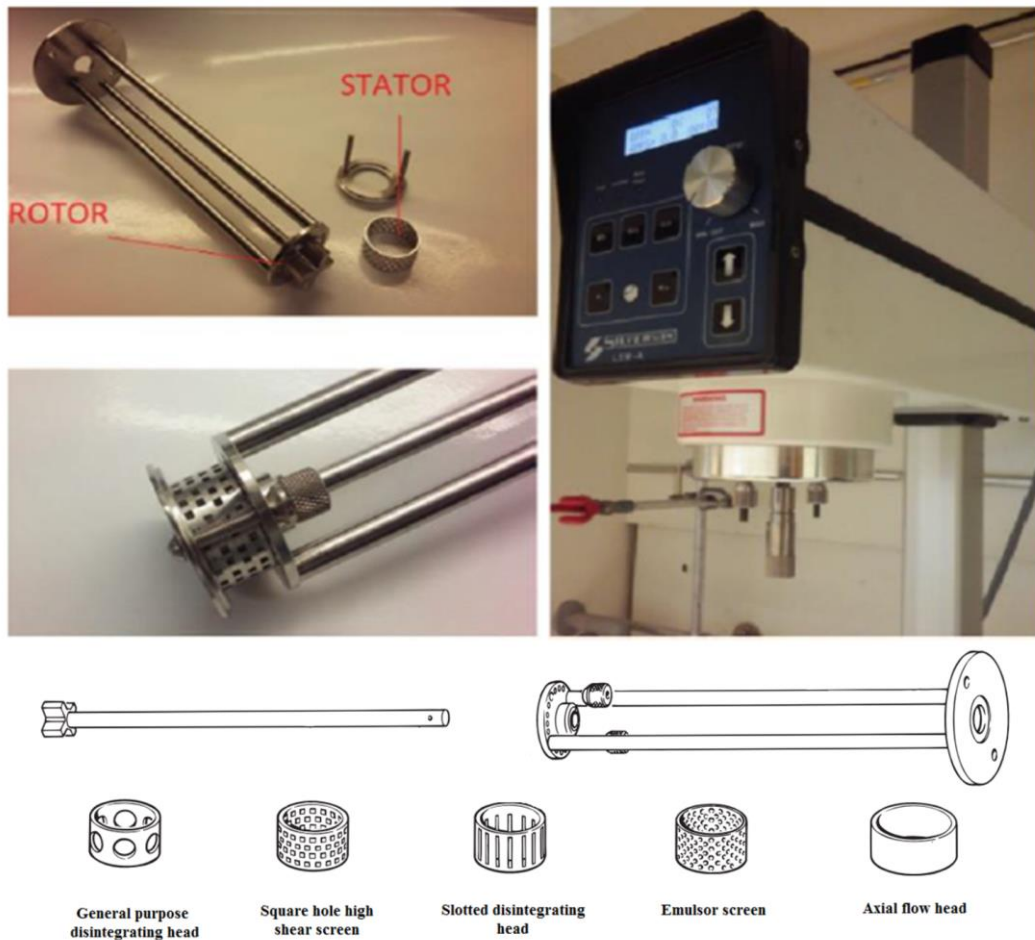


Fig.2.14. Images of the shear mixer (Silverson, L5M series), working head (top) and the different stationary phases (bottom).²¹²

During the rotation, the shear mixer acts as a pump. It is possible to describe the whole process in four stages (**fig.2.14**):²⁰⁹

- The rotation of the rotor applies a powerful pressure gradient driving the dispersion from the bottom of the container into the centre of the workhead.
- The centrifugal force pushes the particles to the gap between the rotor and the stator (the shearing region) where they are subjected to a milling action.
- Afterwards, due to the high velocity, the particles are subjected to a shear exfoliation, forced to pass through the small perforations in the stator and then they are pushed out in the main body of the mix.

- The material horizontally ejected from the workhead is led to the edge of the mixing vessel and, at the same time, fresh material is drawn into the workhead maintaining the mixing cycle.²¹⁰

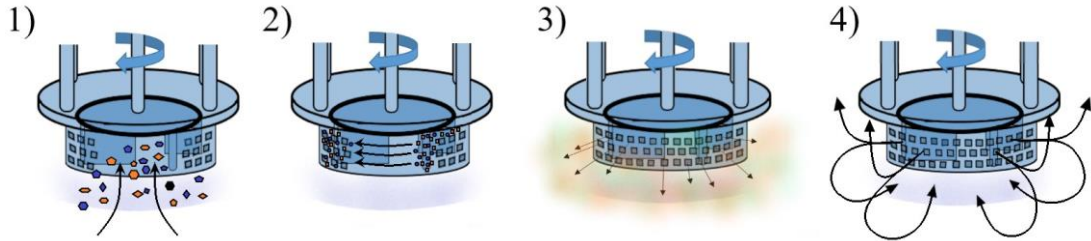


Fig.2.15. *Graphic representation of shearing steps.*

An important parameter to consider is the shear rate, one of the values which are related to the exfoliated material.²¹³ The approximate shear rate ($\dot{\gamma}$) can be calculated via the following equation:

$$\dot{\gamma} = \frac{\pi ND}{\Delta R} \quad (2.12)$$

where N is the rotation per second, D is the diameter of the shear head and ΔR is the gap between rotor and stator ($\sim 100 \mu\text{m}$).^{214,215}

We can describe this process as shear delamination. For a better understanding of this procedure, we can consider two square platelets with $L \times L$ dimension. We assume that they are bonded with weak bonds between them such as van der Waals interactions, and we place them in a flowing solvent at zero shear rate. If we apply shear stress to the material, this will lead to delamination and, consequently, to an exfoliation (**fig.2.15**). According to that, the induced stress can be related to the induced force $F = \sigma L^2$ and for Newtonian fluids, the shear stress is described by the formula $\sigma = \dot{\gamma} \eta$. Thus, combining these two equations, we can relate the force directly to the viscosity (η) and to the shear rate ($\dot{\gamma}$) finding $F = \dot{\gamma} \eta L^2$ or $\dot{\gamma} = F / \eta L^2$. As a result, we can illustrate delamination in three steps. Firstly, the platelets are arranged one on top of the other one bonded with VdW interaction. After that, the

force applied induces a partial sliding, and finally, we have complete delamination of the flakes.^{20,209,216}

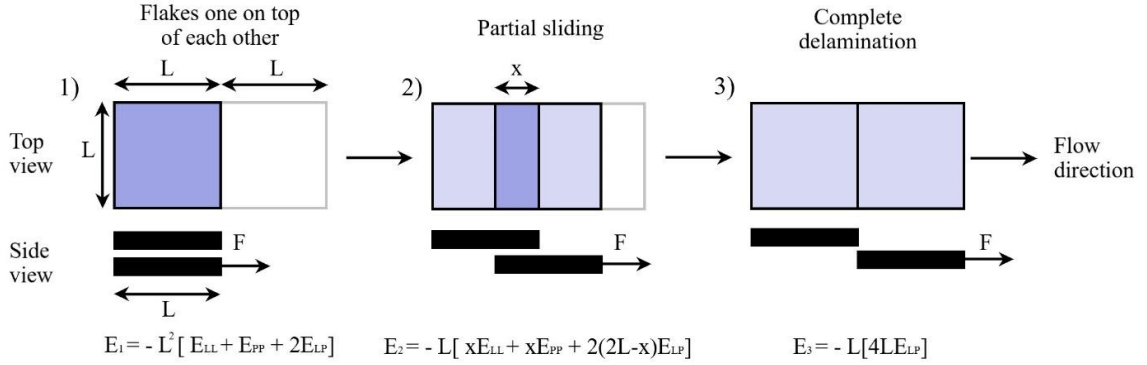


Fig.2.16. Schematic representation of the delamination process in terms of interfacial energies.^{20,217}

It is also possible to analyse the delamination process in terms of interfacial energies and as described from *Paton K. et al.*²⁰ the energy change on the delamination process can be estimated (using the geometric mean approximation $E_{LP} = \sqrt{E_{LL}E_{PP}}$) by the following formula:

$$\Delta E = L^2 \left[\sqrt{E_{LL}} - \sqrt{E_{PP}} \right]^2 \quad (2.13)$$

where E_{LL} is the interfacial energy associated with Liquid-Liquid interaction, E_{PP} is related to the Platelet-Platelet interaction and E_{LP} (**fig.2.15**) is correlated to the Liquid-Platelet interface. Furthermore, the minimum applied force for delamination (F_{\min}) can be obtained from the derivation of the energy: $(-\partial E(x)/\partial x)$. Moreover, using the geometric mean approximation ($\Delta E > 0$) we have²⁰

$$F_{\min} = L \left[\sqrt{E_{LL}} - \sqrt{E_{PP}} \right]^2 \quad (2.14)$$

Consequently, we can define the minimum shear rate to exfoliate particles with L size by²⁰

$$\dot{\gamma}_{\min} = \frac{\left[\sqrt{E_{LL}} - \sqrt{E_{PP}} \right]^2}{\eta L} \quad (2.15)$$

2.4 POLYMERS AND COMPOSITES

2.4.1 Polymers

A polymer is a chemical compound defined as a macromolecule, or large molecule, which is composed of a high number of repeated subunits.²¹⁸ Due to their broad range of properties, there are different ways to classify polymeric materials (**fig.2.17**); from categorizing polymers depending on their molecular characteristics (**fig.2.17 a**), to the type or polymerization reaction (**fig.2.17 b**) or the source type from which these polymers are fabricated (**fig.2.17 d**). Another way is according to their end-use and, depending on its properties, a particular polymer can be used in more than one application. For the purpose of this work, which aims at the use of composite as strain sensors, the last classification has been selected to describe the different characteristics of polymers at first and composites afterwards (emphasizing the attention on the mechanical and electrical response). The various types of polymers include plastics, elastomers (or rubbers), miscellaneous (fibres, coatings adhesives, foams, and films) and advanced materials which include thermoplastic elastomers, liquid crystal polymers, ultrahigh molecular weight polyethylene (UHMWPE).²¹⁹ **Ultrahigh molecular weight polyethylene (UHMWPE)** has been developed considerably over the last several years, and it has mainly found a place in new technologies applications. This is because UHMWPE has extremely high impact resistance, energy absorption characteristics, and excellent low-temperature properties. It is utilised for bulletproof vests, bushings, pump impellers, biomedical prostheses, etc.¹⁸² **Liquid Crystal Polymers (LCPs)** may be considered a new state of matter, where the material is neither liquid nor

crystalline. It is sufficient to say that LCPs are composed of long rigid molecules which are highly aligned in both solid and liquid (melted) state. This characteristic gives them incredible properties and the common use for this material is in displays.²²⁰ The **Thermoplastic Elastomers (TPEs)** are polymeric materials which show elastomeric properties at room temperature while still preserving their thermoplastic nature. This behaviour is due to physical crosslinks which act as anchor points, while normally elastomers are thermosetting for the presence of chemical crosslinks (**Fig.2.17b**). This means that above the melting point, T_m , they melt instead of degrading and therefore can be processed as thermoplastic materials and subjected to a reversible melting-solidification process. In other words, they are recyclable. These materials have replaced thermoset elastomers in a large variety of applications such as automotive components, sporting goods, protective coatings, etc.²²¹ The past years have been focusing on the improvement of this previous polymer generation, nonetheless it is important to have an idea also of the other categories and for this reason a brief description of these polymers is discussed.

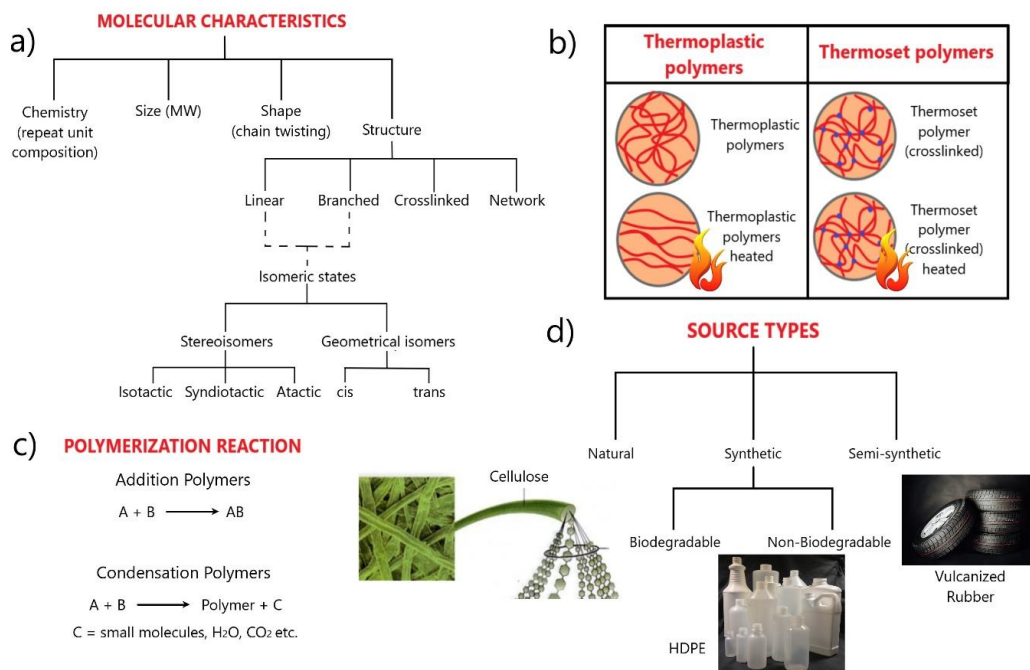


Fig.2.17. Different grouping of polymeric matrices based on a) the molecular characteristics, b) the response at high temperature, c) the polymerization reaction and d) the source.²²⁰

PLASTICS

Plastics is a general term to define synthetic or semi-synthetic organic polymers most commonly derived from petrochemicals. It is possible to classify their mechanical properties between elastomers and fibres.²²² Polymers belonging to this category may have different degrees of crystallinity, molecular structure or configuration, which implies that some are very flexible and can exhibit both elasticity and plasticity while some of them are rigid and brittle (**fig.2.18**).^{222,223} Moreover, they can be thermosetting or thermoplastics depending on their molecular features. However, we can define a polymer as plastic when they maintain their shape below their glass temperature (if amorphous), below their melting temperature (if semi-crystalline) or when crosslinked. Numerous plastics reveal exceptional properties, such as optical transparency (PS, PMMA), chemical attack resistance (Teflon), mechanical strength (Nylon)^{220,221,224} and, for this reason, they are used in countless applications (e.g. lenses, coatings, bearings, gears, safety helmets, toys, bottles, pipes, etc).

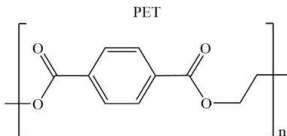
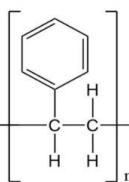
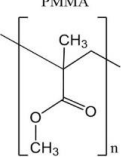
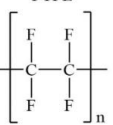
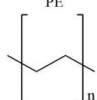
POLYMERS	APPLICATIONS	POLYMERS	APPLICATIONS
<p>PET</p> 	Recording tapes, clothing, beverage containers	<p>PS</p> 	Wall tile, battery cases, toys, indoor lighting panels, appliance housings
<p>PMMA</p> 	Lenses, drafting equipments, transparent aircraft enclosures, outdoor signs	<p>PTFE</p> 	Anticorrosive seals, chemical pipes and valves, antiadhesive coatings, high temperature electronic parts
<p>PE</p> 	Flexible bottles, toys, tumblers, battery parts, ice trays, film wrapping materials		

Fig.2.18. Examples of the most common plastics used and their applications.²²⁰

ELASTOMERS

One of the most fascinating properties of elastomers is their ability to be largely deformed and spring back to their original form when they are in an unstressed state. The elastomeric behaviour, due to crosslinks between the chains, was first observed in natural rubber (**Fig.2.19**).¹⁸²

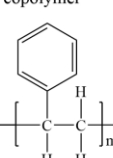
POLYMERS	APPLICATIONS	POLYMERS	APPLICATIONS
Natural polyisoprene (rubber) $\left[\begin{array}{c} \text{CH}_2 \quad \text{H}_2\text{C} \\ \quad \\ \text{C} = \text{C} \\ \quad \\ \text{H}_3\text{C} \quad \text{H} \end{array} \right]_n$	Pneumatic tires and tubes; heels and soles	Chloroprene (Neoprene) $\left[\begin{array}{c} \text{H}_2 \quad \text{H}_2 \\ \quad \\ \text{C} - \text{C} = \text{C} - \text{C} \\ \quad \\ \quad \quad \text{H} \quad \quad \text{Cl} \end{array} \right]_n$	Wire and cable; belts, hoses, seals and gaskets
Styrene-butadiene copolymer $\left[\begin{array}{c} \text{H}_2 \quad \text{H}_2 \\ \quad \\ \text{C} - \text{C} = \text{C} - \text{C} \\ \quad \\ \text{H} \quad \text{H} \end{array} \right]_n \left[\begin{array}{c} \text{H} \quad \text{H} \\ \quad \\ \text{C} - \text{C} \\ \quad \\ \text{H} \quad \text{H} \end{array} \right]_m$ 	Same as natural rubber	Polysiloxane (Silicone) $\text{HO} \left[\begin{array}{c} \text{CH}_3 \\ \\ \text{Si} - \text{O} \\ \\ \text{CH}_3 \end{array} \right]_n \left[\begin{array}{c} \text{CH}_3 \\ \\ \text{Si} - \text{O} \\ \\ \text{CH}_3 \end{array} \right]_m \text{OH}$	High and low temperature insulation; seals for food and medical uses

Fig.2.19. Examples of common elastomers.²²⁰

However, a polymer must have a series of characteristics to be considered an elastomer. First of all, elastomers are amorphous polymers that must not easily crystallize. Second, their chain bond rotation must be reasonably free to easily respond when under stress. Third, the plastic deformation has to be delayed and the presence of crosslinks must prevent the chain slippage typical of plastics acting like an anchor. The crosslinking process occurs in most of the elastomers via vulcanization, the process involving sulphur bond formation between the chains. Finally, the elastomer must be above its glass transition temperature for below that it becomes brittle (**Fig.2.20** and **Section 2.4.8**).²²⁵

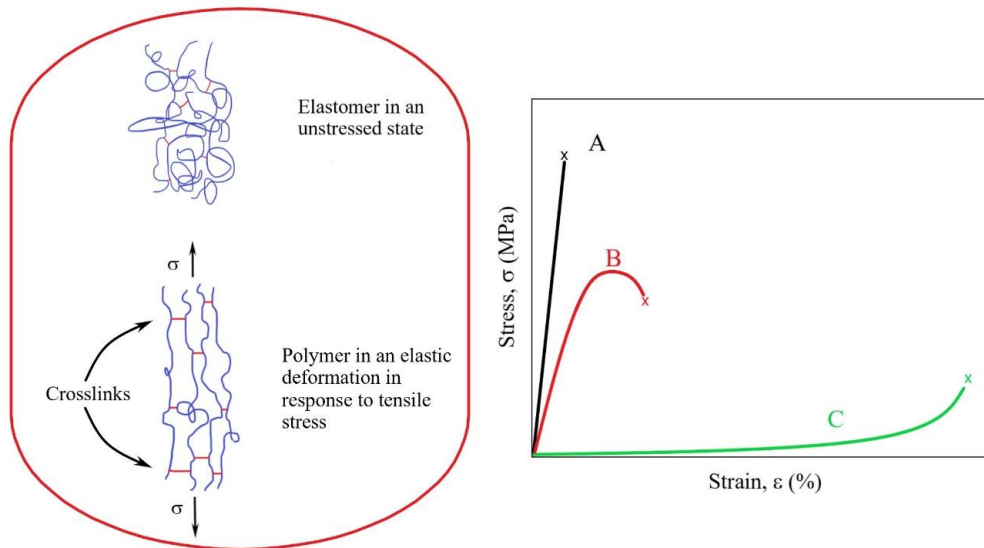


Fig.2.20. Schematic representation of crosslinked elastomers in both relaxed and stressed mode on the left, and stress-strain behaviour for brittle (a), plastic (b), and elastic (c) materials on the right.

MISCELLANEOUS APPLICATIONS

- *Fibres.* The most common fibre polymers are used in the textile industry; they typically have a 100:1 length/diameter ratio. While in use, fibres may be subjected to a variety of mechanical deformations such as shearing, twisting, stretching and abrasion. Therefore, they must have high tensile strength and high elasticity modulus, as well as abrasion resistance. These properties depend on both chemistry of the polymer chains and the fabrication process.
- *Coatings.* Coatings are mainly used for three purposes: 1) to protect the item from deteriorating or abrasive environment, 2) to provide electrical insulation, and/or 3) to improve the item appearance. Many common coatings are latexes, which is a stable suspension of small insoluble polymer dispersed in water. Another subclass of materials belonging to this category is the *adhesives materials*. This substance is used to bond together the surface of two solid materials. There are two types of bonding mechanisms: chemical and mechanical. In the case of mechanical adhesion, the material

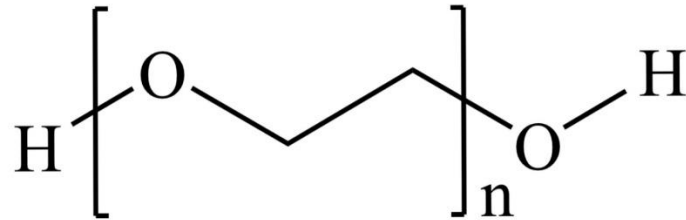
penetrates into the pores of the surface attached (i.e. methacrylates).²²⁶ Chemical bonding comprises both covalent and weak bonds (i.e. Van der Waals) between the adhesive and the adhered material; in the case of VdW bonds, polar functional groups enhance the adhesion. Depending on the type of the surface on which to adhere, a selective polymer can be used. Albeit different natural polymers have adherence characteristics (casein, starch, animal glue), synthetic polymers such as polyurethanes, polysiloxanes (silicones) and acrylates are commonly used as adhesives.^{182,220,226}

- *Foams*. Foams can be defined as plastic materials with a high percentage in volume of bubbles trapped in the solid matrix. This type of polymer is commonly used in thermal insulation as well as packaging and furniture. Typical materials belonging to this class are polyurethanes, rubbers, polystyrenes and PVC.
- *Films*. Films are polymeric materials with a thickness between 0.025 and 0.125 mm. These compounds are fabricated for several purposes among which there are food packaging, textile products, and in the last decade for biomedical uses.²²⁰ These materials are characterised by a high degree of flexibility, high tensile strength and high tear strength. In this work, Polyethylene oxide (PEO) films (as well as PDMS films) have been fabricated with the purpose of finding a biocompatible and flexible material for sensing applications.

2.4.2 Polyethylene Oxide (PEO)

PEO is a common thermoplastic polymer also known as polyethylene glycol (PEG) or polyoxyethylene (POE) depending on the molecular weight. Its structure, shown in **fig. 2.21**, comprises the presence of oxygen atoms in the chain which gives it the hydrophilic character and, even though the chemical properties do not change with the molecular weight, the physical properties are significantly different as the chains length changes, i.e. PEO is solid while PEG is liquid at room temperature.^{227,228} Because different properties lead to different applications in both

chemical and biological fields, this polymer is categorized as a function of its molecular weight. For this reason, PEO is considered as such if its molecular weight is above 20,000 g/mol.



PEG $\rightarrow 4 \leq n \leq 460$ ($200 \leq \text{MW} \leq 20000$ Da)

PEO $\rightarrow n \geq 460$ ($\text{MW} \geq 20000$ Da)

Fig.2.21. Polyethylene oxide structure.

The PEO at room temperature is tough, exceptionally crystalline, and it shows a moderate Young's modulus that changes proportionally with its molecular weight. Moreover, it has very high elongation, and it is characterized by the ability to orient when stressed. Although PEO is water soluble, its tensile properties are not significantly affected by the humidity up to 90%, where it drops drastically.²²⁷ Furthermore, PEO can be processed using the methods for common thermoplastic polymers such as molding, extrusion, etc.¹⁸² Usually, this polymer is used as an additive or, most commonly, as a component for copolymer preparation combining the properties of two or more matrices and subsequently used in several applications ranging from biomedical to high-performance battery fabrication.^{229–231}

2.4.3 Polydimethylsiloxane (PDMS)

PDMS, or dimethicone, is maybe the most widely used elastomer for its incredible mechanical and rheological properties, optical transparency, inert and, not-toxic which make it suitable for innumerable applications.²³² This polymer belongs to the class of organosilicon compounds that are referred as siloxanes or silicones.^{223,232,233}

Siloxanes comprise a backbone of alternating silicon-oxygen repeating units with organic chains attached to the silicon atoms, in the case of the PDMS, as the name suggests, the organic chains attached are two methyl groups (**Fig.2.22**).

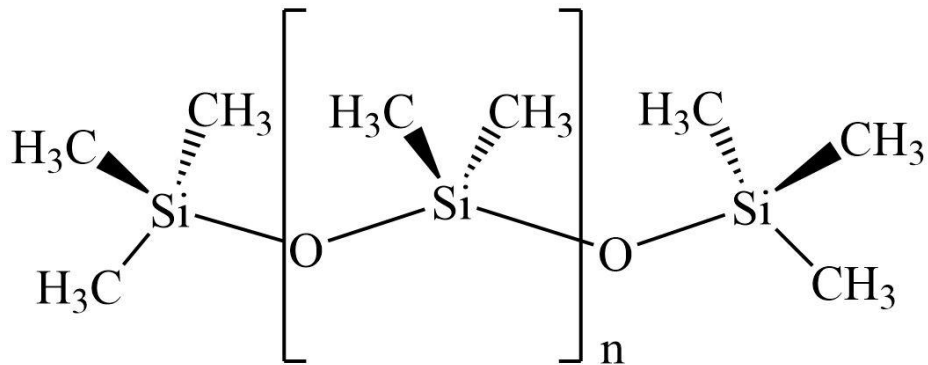


Fig.2.22. PDMS structure.

Thanks to long and highly flexible backbone chains, PDMS has rubber-like properties. This polymer is classified as a viscoelastic, non-crystalline elastomer and depending on the type and the degree of crosslinking we have different mechanical responses (i.e. physical crosslinking for silly putty,^{137,138} and chemical crosslinking for Sylgard 170®²³⁴). The presence of methyl groups gives the high hydrophobicity to the molecule as a consequence, in case of chemical crosslinking, non-polar solvents (THF, chloroform) are able to swell considerably this polymer. Also, depending on the demand, the properties of this polymer can be easily tuned finding place in several applications from contact lenses and medical devices^{235–237} to shampoos²³⁸ and anti-foaming agent.^{239–241}

2.4.4 Composites

Composites are materials consisting of several chemically different constituents, with a separation interface. The combination of these materials leads to physical-chemical properties not found in the individual materials that compose it. An example of a composite structure is reinforced concrete where cement and steel preserve their identity.²⁴² The structure of the composites consists of a matrix and

a filler or reinforcement. The matrix comprises a continuous homogeneous phase which encloses the reinforcement (called also filler) and ensures that the particles of the latter are dispersed inside the composite without segregation. Thus, depending on the type of composite we want to obtain, the choice of the matrix is important as much as the filler choice.

The reinforcement (or filler) constitutes the dispersed phase in the matrix and we can classify composites based on the type of reinforcement in 1) particulate composites, 2) fibre reinforced composites (continuous and discontinuous), and 3) structured composites (formation of interpenetrating lattices). Particular composites consist of particulates dispersed in the matrix (e.g. gravels, micro-granules, and resin powders). The latter has a marked anisotropy (a property for which a given object has characteristics that depend on the direction along which they are considered).²²⁴ In both cases, there is no significant interaction between the matrix and reinforcement interface, but in the case of the fillers, if the filler is on the order of nanometres, the so-called nano effect²²⁰ takes place. This effect is defined by an increase in surface atoms and, consequently, the interfacial region rises considerably. In this case we can define a nanofiller as a reinforcement. This type of filler leads to a very high contact area between matrix and filler and therefore to a significant increment in a variety of performances. Based on the dimensions (length, width, height) of the dispersed particles, we can classify the nanofillers into isodimensional particles (0D), when the three particle sizes are of the order of nanometres (i.e. fullerenes, POSS, metals);^{243,244} one-dimensional particles (1D), such as nanotubes or whiskers, when two dimensions out of three are nanometric;^{182,245} two-dimensional (2D) particles, when only one dimension in three is nanometric (TMDs, TMOs, graphene). In this case, the filling material is present in the form of sheets with a thickness of a few nanometres.

0D and 1D particles are described more in depth in the two paragraphs below, whereas 2D materials, such as graphene and TMDs, and their characteristics have been previously described (**section 2.2**).

2.4.5 0D Particles

As mentioned above, POSS, fullerenes and metals are isodimensional particles examples.

POSS (polyhedral oligomeric silsesquioxanes) are polyhedral structures composed mainly by silicon and oxygen;²⁴⁶ the silicon atoms are placed at the vertices of the polyhedron and the oxygen is interposed between them in a tetrahedral geometry. These polyhedral compounds can be linked to organic or inorganic substituents which determine the chemical and physical properties of the material and based on their number we will have a particular name (i.e T₈ for structures containing eight substituents, T₁₂ the molecule has twelve substituents, etc.) (**fig.2.23**).^{247–254} POSS synthesis had a considerable impact on nanocomposite polymeric materials production,^{255–260} for example, with the insertion of nanoparticles directly in the melted polymer by simply mixing.²⁵⁷ This material, in fact, is able to adapt the compatibility and solubility with the polymer thanks to its non-polar interactions which occur between the R groups and the polymer itself;^{248–250,261} this represents a useful property for the study and production of innovative materials. In fact, with the insertion of reactive functional groups (i.e. acrylic, methacrylic groups, etc.) it is possible to fabricate hybrid systems (called also “macromers”)^{246,247,256,259,262–265} which have a broad range of properties such as higher decomposition temperature and glass transition temperature (T_g), oxygen permeability increase, viscosity reduction, resistance to oxidation, and improvement of mechanical properties.^{266,267}

Metals are the substances that drastically change their properties as their dimensions are reduced to nanometric size.²⁶⁸ Thus, it is fundamental to understand how size, shape, surface, and state of aggregation of the nanocharges change after integration with the polymeric matrix, in order to optimize the final nanocomposites performances. For this reason, it is useful to characterize the nanocharges with techniques such as transmission electron microscopy (TEM), dynamic light scattering (useful for granulometric analyzes), and UV-vis spectral spectroscopy. These analyses methods allow to relate their size and shape with their peculiar optical, magnetic and catalytic properties^{103,269–271} and, for these reasons it is possible to use polymeric nanocomposites with silver and gold in a broad range of applications.^{272–275} For example, one of the gold nanoparticles applications is as detector of biomarkers for the diagnosis of heart diseases, tumors and infectious agents.^{99,274,276–278} Whereas, silver nanoparticles are introduced into polymeric materials in order to exploit their high electrical stability and conductivity for

products that find applications in the photovoltaic field^{107,279–281} and for the production of biological and chemical sensors.^{105,108,110,279,279,282–285}

As previously mentioned, **fullerene** is a nanometric allotrope of carbon (**fig.2.1**) and the first type of fullerene, discovered in 1985 by Kroto *et al.*³ is called fullerene C₆₀, “buckyball” or buckminsterfullerene. This carbon cluster is defined as icosahedron, a polygon with 60 vertices, 12 pentagonal and 20 hexagonal faces.²⁸⁶ Thanks to their peculiar physical and chemical properties, fullerenes and its derivatives are used in manifold applications from biology²⁷¹ to chemistry²⁸⁷ and physics²⁸⁸ applications, such as electron transport layer in heterojunction perovskite solar cells,²⁷¹ as a support for bone cell growth to treat arthritis,²⁸⁹ or for thin-film transistor fabrication.²⁹⁰ Lately, the C₆₀-based nanostructures, including nanotubes, nanorods, and nanosheets have been one of the fulcrums of nanoscience and the use of this material represents one of the ways forward for further studies and applications.²⁶⁸

2.4.6 1D Particles

Carbon nanotubes (CNTs) are examples of one-dimensional particles. It was discovered in 1991 by the Japanese Sumio Iijima as secondary products during fullerenes manufacture.² It is difficult to give a precise definition of carbon nanotubes due to the variety of their shapes and conformations, but we can divide them into two classes:

- SWNT, single-walled nanotubes
- MWNT, multi-walled nanotubes

An SWNT can be seen as a sheet of graphene rolled-up on itself to form a cylinder closed in both ends. The body of the nanotube is formed only by hexagons while the ends by hexagons and pentagons, like fullerenes, and for this reason they are called “buckytubes”.^{291,292} MWNTs consist of several concentric cylinders. Every single nanotube that forms the MWNT retains its properties, so it is very difficult to predict its behavior; moreover, they contain a greater number of defects and this limits their use.²⁹³ Carbon-based nanotubes are very resistant and hard materials: experimental evidence shows that they can be incorporated in polymer matrices to

create materials with interesting mechanical properties.^{294–300} Structural defects can be present on the sheets which can reduce the elastic modulus and tensile strength of the material even by some orders of magnitude. However, it is possible to reduce the number of defects through high-temperature treatment.^{292,296,301} Regarding the electric properties, SWNTs, despite the structural affinity to a graphite sheet which is a semiconductor, can assume metallic behavior depending on the way in which the graphite sheet is rolled up to form the nanotube. The electric properties of perfect MWNTs are similar to those of defect-free SWNTs due to the weak coupling between MWNT cylinders.^{302–307} Electronic transport in SWNTs and metal MWNTs takes place along the length of the tube, so they are able to transport high currents without overheating.³⁰⁸

The thermal properties are represented by the specific heat and thermal conductivity, which propagate easily along the pipe; this is why nanotubes are good thermal conductors and good insulators transversely to the axis of the tube.^{308–311} Thanks to all these characteristics, the applications of these materials are innumerable starting from the formation of high-performance polymeric materials up to the production of nanodiodes.^{291–293} The limits in the use of these materials are mostly due to their high cost compared to other materials (i.e. graphene).

The study of nanocomposites constitutes a highly multidisciplinary field of investigation that involves multiple research directions ranging from molecular biology to chemistry, from material science to physics, and from mechanical and electronic engineering.²²⁰ For this reason, it is important to explain both mechanical and electrical characteristics that describe a nanocomposite.

2.4.7 Mechanical properties of materials

It is important to know the mechanical properties of materials in order to prevent their fracture when in service. We can define the mechanical behaviour of a material as the relationship between its response or deformation to an applied load or force. To study this behaviour we need to recreate the conditions by applying certain types of loading, and depending on the type of experiment we want to perform, the

duration of the force applied as well. It is possible for the force applied to be tensile, compressive, shear or torque (**Fig.2.23**).^{182,220,225}

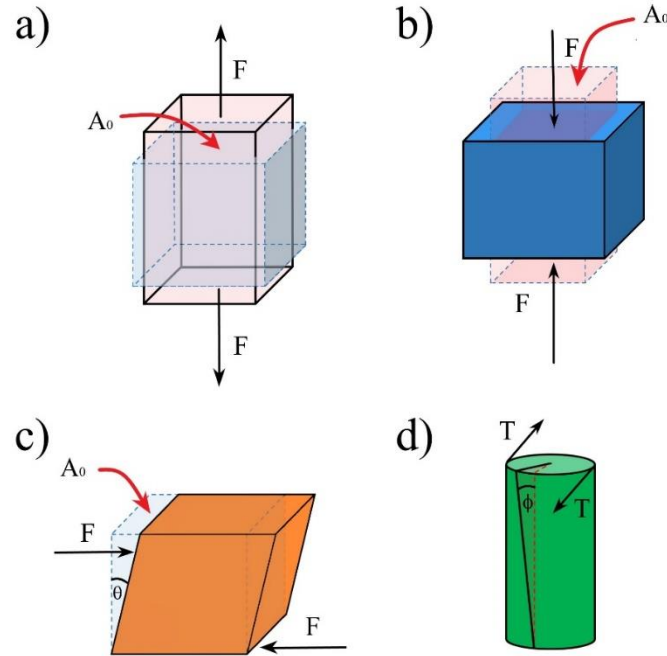


Fig.2.23. Schematic representation of how tensile (a), compression (b), shear strain (c) and torque load (d) produce a deformation on materials.

One of the most common mechanical tests performed on materials is tension. Typically, during tensile tests, a well-defined sample is permanently deformed and usually fractured. The output of these tests is recorded as force versus elongation and the results are dependent on the specimen size. Thus, we can define the stress, σ , and the strain, ϵ , as:

$$\sigma = \frac{F}{A_0} \quad (2.16)$$

$$\epsilon = \frac{l_i - l_0}{l_0} = \frac{\Delta l}{l_0} \quad (2.17)$$

where F is the force applied to the material over the area, A_0 , of the specimen (equation 2.16); l_i is the elongated length of the specimen, l_0 is the initial length and Δl is defined as the change in length of the specimen. For most of the materials, at relatively low tension strain level, stress and strain are proportional.²²⁰

$$\sigma = Y \cdot \varepsilon \quad (2.18)$$

This is known as Hooke's law where Y is the modulus of elasticity (Young's modulus) which represents the constant of proportionality expressed in GPa (or MPa). For both tensile and compression tests, the elasticity modulus is described in the same way but, for the shear stress-strain curves the shear modulus, G , represents the slope of the linear elastic region. It is defined at low loading by this formula:

$$\tau = G \cdot \gamma \quad (2.19)$$

Furthermore, for isotropic materials (dependent on the direction in which stress is applied), shear and elastic moduli are related to each other according to this equation:

$$Y = 2G(1 + \nu) \quad (2.20)$$

Where ν is the Poisson's ratio, defined as the ratio of the lateral and the axial strains (**Fig.2.24b**)

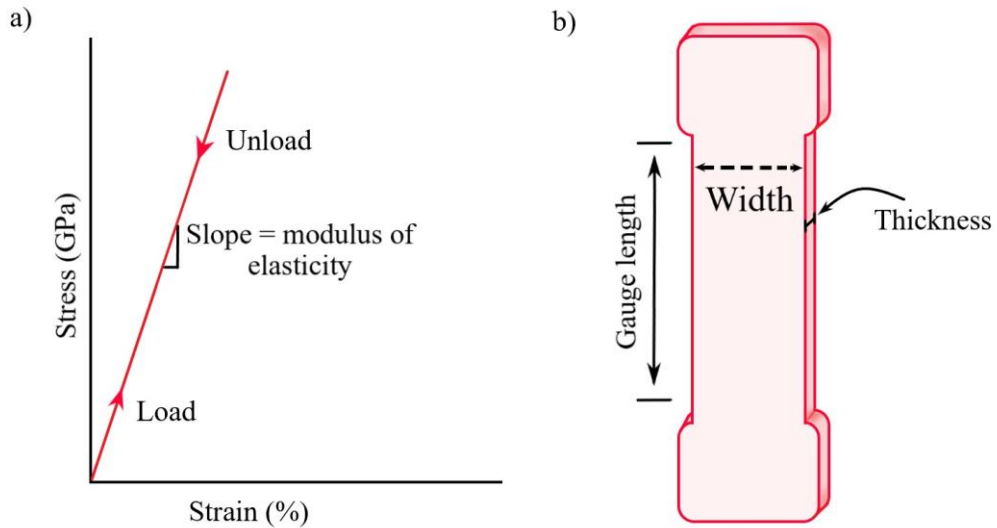


Fig.2.24. Schematic stress-strain diagram (a) showing the linear elastic deformation of a standard specimen (b).

So far, just stress-strain curves at low loading level have been described but, as a material is deformed beyond the linear region, stress is no longer directly proportional to the strain and a plastic deformation occurs. The graph in **fig.2.25** shows the typical plastic behaviour of a material. Here, the strength increases gradually until it reaches a point where the material experiences a permanent change in shape and the phenomenon of yielding occurs. The stress corresponding to this point is called *yield strength*.³¹²

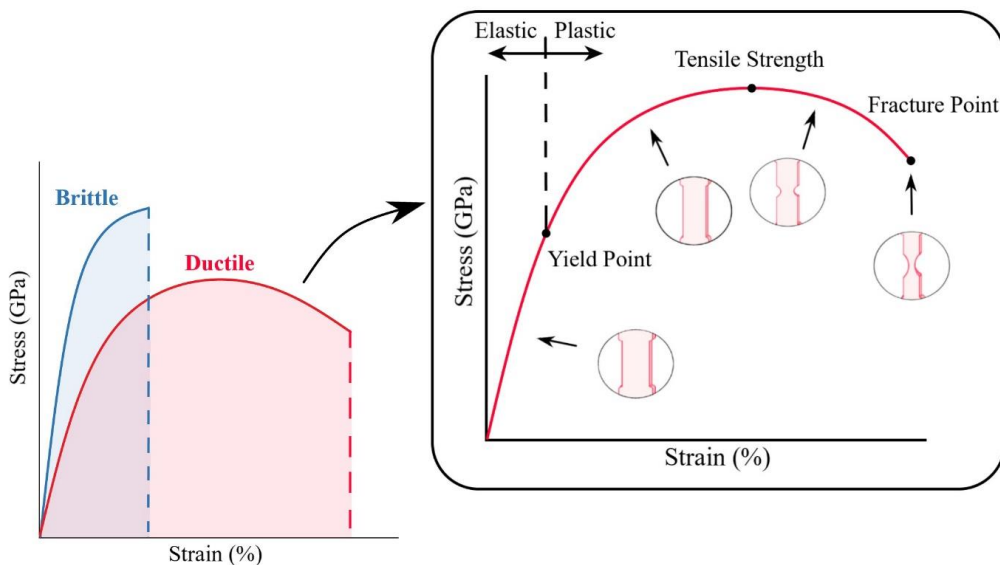


Fig.2.25. Graphic representation of a typical plastic curve.

In this case, the curve reaches a maximum (called *tensile strength*) and, after this point, the stress decreases until the fracture point. The area below this curve describes another important mechanical property called *ductility* which is a measure of the degree of plastic deformation a material can sustain. Quantitatively, this parameter can be expressed as the percent elongation (plastic strain % at fracture) and a material with very little or no plastic deformation is called *brittle*. Up to this point, we assumed that both elastic and plastic deformation are time independent; however, for most of the materials, after an elastic strain is released a certain amount of time is needed for recovery. This time-dependent elastic behaviour in polymeric materials is known as *viscoelastic behaviour*. Moreover, in case an inelastic material has a plastic deformation that depends on the rate of the test, we introduce *viscoplastic behaviour*. In this case, it means that the irreversible deformation depends on the rate at which a load is applied. However, both a semicrystalline and amorphous polymer exhibit elastic as well as viscous characteristics, and the combination of these two properties determine the viscoelastic behaviour (Fig.2.26).^{220,312}

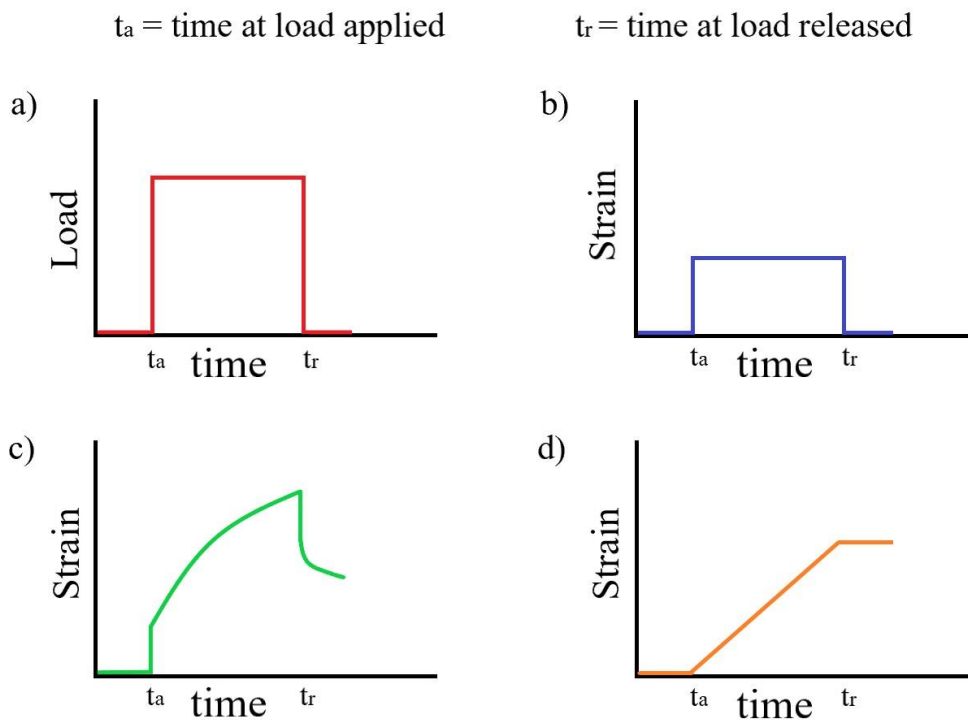


Fig.2.26. Response of different materials as a load (a) is applied for a certain time: elastic (b), viscous (c) and viscoelastic (d) behaviour.

Because of these characteristics, the resultant stress-strain curve of a viscoelastic material shows an initial elastic response which is followed by the elastic limit. After that, a viscous time-dependent strain occurs and a plastic response takes place (**Fig.2.27**).³¹³

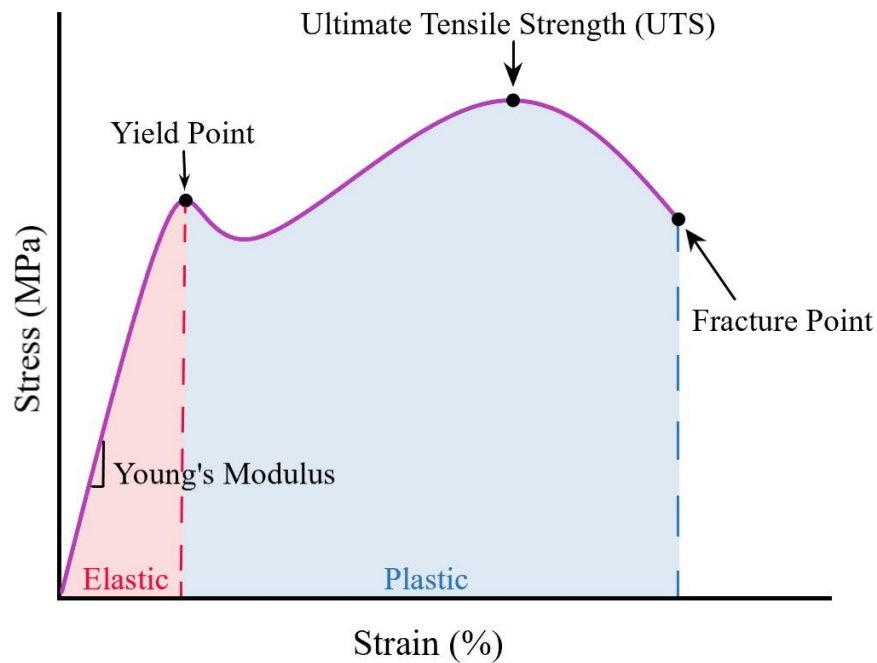


Fig.2.27. Schematic tensile stress-strain curve for a semicrystalline polymer.

A viscoelastic material has the following properties:

- Hysteresis
- Stress relaxation
- Creep

The hysteresis is due to the viscous component of the material which shows different stress values when it is underdone to loading-unloading cycle (**Fig.2.28**).

Indeed, purely elastic materials do not dissipate energy when a load is applied. However, in the case of viscoelastic materials, this energy loss can be evaluated with the area of the loop - the higher the energy loss the higher the hysteresis. Another way to evaluate this energy loss is through the calculation of the percent hysteresis (H%)

$$H\% = \frac{\sigma_0 - \sigma_i}{\sigma_0} \times 100 \quad (2.21)$$

where σ_0 and σ_i are the load and unload stress respectively, taken at the same value of the strain applied (**Fig.2.28b**)

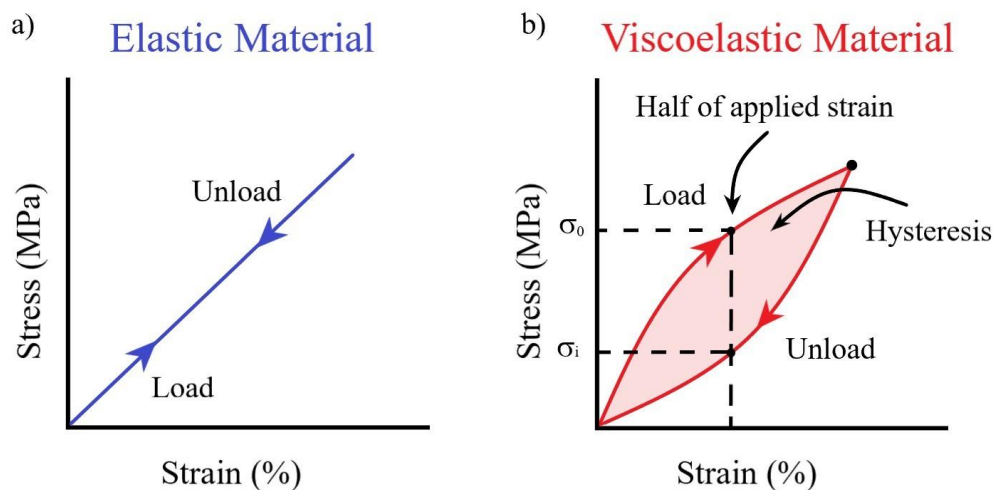


Fig.2.28. Stress-strain curve for a purely elastic material (a) and a viscoelastic material (b).

Another way to measure viscoelastic behaviour is through the examination of its time-temperature dependency. One method is through stress relaxation measurements where the strain is kept constant and the stress as a function of time (or temperature) is recorded and a *relaxation modulus*, $E_r(t)$, represents a time-dependent elastic modulus for viscoelastic polymers and is calculated through

$$Y_r(t) = \frac{\sigma(t)}{\varepsilon_0} \quad (2.22)$$

where $\sigma(t)$ is the measured time (or temperature)-dependent stress and ε_0 is the strain level kept constant. Another method to study the viscoelasticity is through the creep modulus calculation. Indeed, many materials are susceptible to time-dependent deformation when the stress is kept constant, and this deformation is called *viscoelastic creep*:²²⁰

$$Y_c(t) = \frac{\sigma_0}{\varepsilon(t)} \quad (2.23)$$

2.4.8 Effect of fillers on mechanical properties

Many of our technologies require materials with unusual combinations of properties that cannot be found in just polymeric materials by themselves, and for this reason, the development of composite materials is necessary. This requires a model that describes the combined properties of the material. A mathematical equation to predict the elastic modulus of composites (c) is based on the combination of both filler and polymer elastic moduli and volume fractions. This relationship is called **rule of mixtures**^{312,314} and is represented by:

$$Y_C = Y_f \Phi_f + Y_m \Phi_m = Y_f \Phi_f + Y_m (1 - \Phi_f) \quad (2.24)$$

here, Y and ϕ denote the elastic modulus and the volume fraction of filler (f) and matrix (m), respectively. However, it is important to point out that, when a filler is added to the polymer, its mechanical properties depend not only on the filler

characteristics but also on the degree to which the stress applied is transferred to the filler itself, by the matrix and also on the orientation of the filler.^{59,314,315} These effects have been abundantly studied with the **shear lag theory**,^{314,316,317} which assumes that the stress transfer occurs through a shear stress at the nanoplatelets/matrix interface. Recently, Young *et al.*³¹⁴ developed a theory able to predict the elastic moduli of different polymer matrixes reinforced with graphene nanoplatelets (GNPs), and that can be applied to other layered materials such as MoS₂, WS₂, WSe₂ and MoSe₂.⁵⁹ The work describes how other factors, such as particle geometry, orientation, and the strength of filler-matrix interface interacts between them. Based on these studies, the equation 2.24 can be rewritten considering these variables:

$$Y_C = \eta_l \eta_o Y_f \Phi_f + Y_m (1 - \Phi_f) \quad (2.25)$$

where η_l and η_o are the efficiency factors associated with the nanoparticle length^{37,59} and orientation (i.e. $\eta_o = 1$ for aligned nanoplatelets and is equal to 8/15 for randomly oriented nanoplatelets)³¹⁸, respectively. For non-aligned nanoplatelets, η_l is given by

$$\eta_l = 1 - \frac{\tanh(nl_f / 2t_f)}{(nl_f / 2t_f)} \quad (2.26)$$

where

$$n \approx \sqrt{\frac{Y_m \Phi}{Y_f (1 + \nu)}} \quad (2.27)$$

here, l_f and t_f are length and thickness of the filler and ν is the Poisson's ratio. Alternatively, for aligned fillers, it is possible to use the Halpin-Tsai model to calculate the composite modulus:³¹⁷

$$Y_C = Y_m \left[\frac{1 + 2\Phi \eta l_f / t_f}{1 - \Phi \eta} \right] \quad (2.28)$$

where

$$\eta = \frac{Y_f / Y_m - 1}{Y_f / Y_m + 2l_f / t_f} \quad (2.29)$$

2.4.9 Effect of the fillers on the electrical properties

ELECTRIC PROPERTIES OF MATERIALS

We have considered the mechanical properties of polymers and, in general, what the effects were of the filler insertion into a matrix. In this section, we give an overview of the effects conductive fillers have on the electrical properties of polymers and how this affects sensing applications. One of the most important electrical properties of a solid material is the ease at which it conducts electricity; this is described by Ohm's law which relates the current, I , that passes through a material with a resistance, R , and the voltage, V ($V = IR$).²²⁰ While the resistance is influenced by the geometry of the specimen, the resistivity, ρ , is independent from it and it is correlated to the resistance through this equation:

$$\rho = \frac{RA}{l} \quad (2.30)$$

where l is the distance between the two measuring points and A is the cross-sectional area perpendicular to the current flow. This parameter is expressed in units $\Omega \cdot m$. Another important parameter which describes the electrical properties is conductivity. This parameter is an indicator of how well a material can conduct electricity and is defined as the reciprocal of the resistivity (ρ)⁻¹.²²⁰

$$\sigma = \frac{1}{\rho} \quad (2.31)$$

COMPOSITE CONDUCTIVITY AND PERCOLATION THEORY

When a conductive filler is inserted into a polymeric insulating matrix, it is assumed that the nanoparticles (or other types of conductive fillers) are totally surrounded by the polymer (**fig.2.29**). Thus, the conductivity of the nanoparticles is limited by the presence of the insulating material, and the only way the charge transport can occur is through quantum tunnelling effects.^{36,318-320}

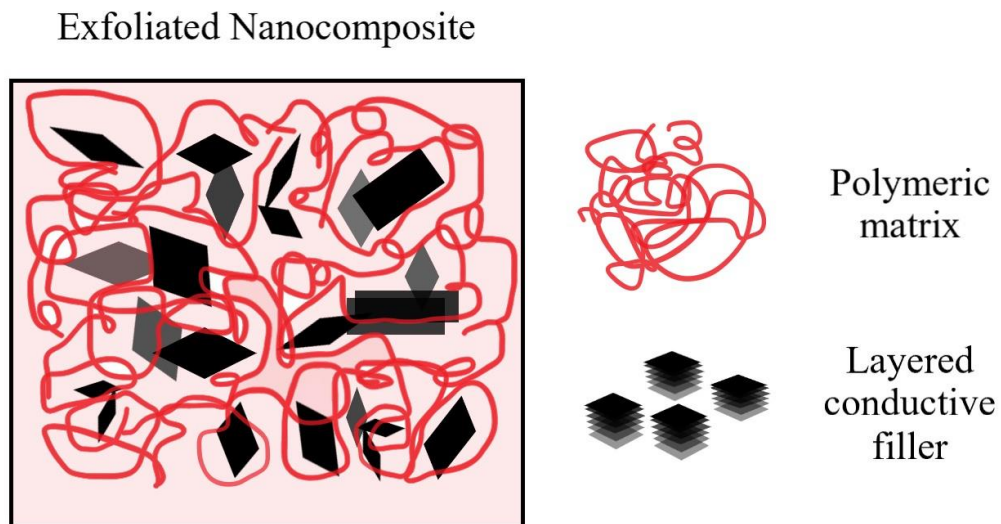


Fig.2.29. *Graphic representation of composites.*

An important aspect to evaluate is how the conductivity changes as we increase the amount of conductive filler we insert in the matrix. Indeed, as we add the filler, the electrical properties of the whole composite vary in a determined way that can be described through *percolation theory*.^{321,322} In general, percolation theory can be defined as a model which is intended to describe the propagation of small particles (i.e. ions, electrons) through a medium.³²³ This process can be applied to several systems and can be used to describe different properties.^{323–325} In the case of the electrical behaviour description in a composite, percolation theory states that the conductivity of a composite depends on the concentration of the nanoparticles following a power law:^{323,325,326}

$$\sigma = \sigma_0 (\Phi - \Phi_c)^n \quad (2.32)$$

where σ is the conductivity of the film, σ_0 is the conductivity of the filler, Φ is the volume fraction of the filler, Φ_c is the volume fraction of the filler at the percolation threshold, and n is the percolation exponent (which for 2D composites, i.e. thin films, assumes a value of 1.3).³²⁷ In fact, charge carriers flow in a composite through a connecting network which is formed by adding conductive particles to a polymeric matrix (**fig.2.30**). In this process, there is an initial growth of conductive clusters (**fig.2.30 A, B**) which is followed by a conductive pathway formation (percolation threshold, **fig.2.30 C**).

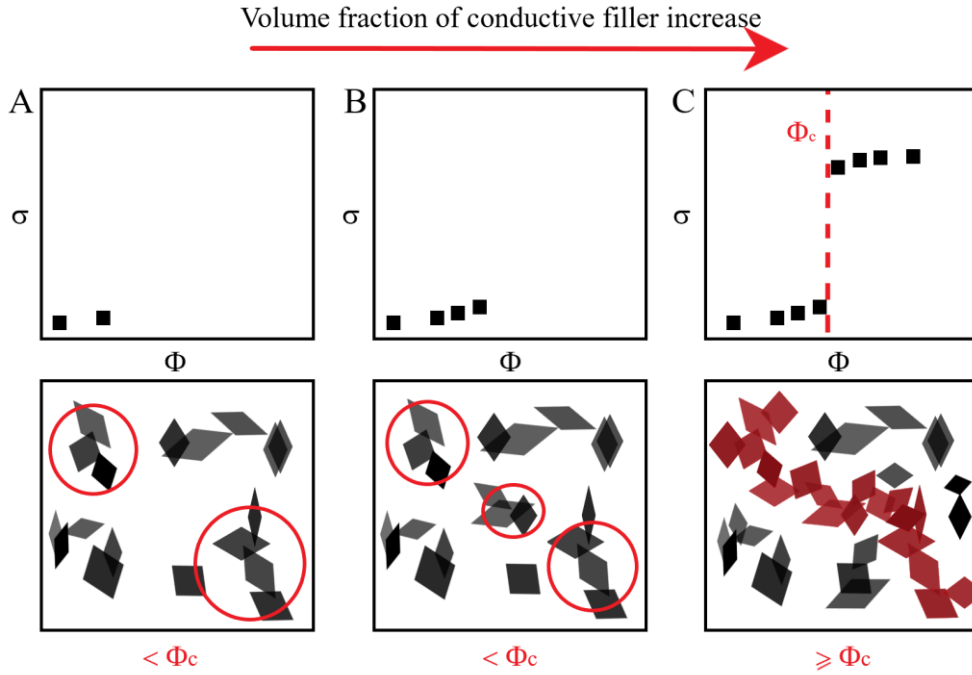


Fig.2.30. Charge transport showing the behaviour of the material as the filler is added to the polymer until it forms a conductive path ($\geq \Phi_c$).

In other words, classical percolation theory regards geometrical connectivity complemented with the electrical connectivity in disordered systems. However, the correlation between the two depends on several physical processes and one of them, as mentioned before, is the tunnelling effect.^{134,324,328,329} In general, this effect is defined as a phenomenon where subatomic particles pass through a potential barrier.³³⁰ In conductive polymeric systems where this effect occurs, the transport mechanism of the charges is based on the “nearest neighbour” interparticle tunnelling (i.e. carbon black composites).³²⁴ However, this effect is related to the temperature accordingly to the equation:³²²

$$\rho = \rho_0 e^{[-T_1/(T+T_0)]} \quad (2.33)$$

where T is the temperature of the system, T_1 is the energy necessary to transport an electron through the polymer, and T_0 is the energy required to have the resistivity

independent of temperature. Both T_1 and T_0 can be evaluated by the following equations³²²:

$$T_1 = \frac{wA\varepsilon_0^2}{8\pi k} \quad (2.34)$$

$$T_0 = \frac{2T_1}{\pi\chi w} \quad (2.35)$$

where χ and ε_0 are defined by

$$\chi = \sqrt{\frac{2mV_0}{h^2}} \quad (2.36)$$

$$\varepsilon_0 = \frac{4V_0}{ew} \quad (2.37)$$

and where m and e are mass and charge of an electron, respectively, A is the area of the capacitance formed by the junction, w is the interparticle distance, h is the Plank constant and V_0 is the potential barrier height. Based on these studies, it was possible to relate the resistivity to the gap width, W , and when we have temperature constant:

$$\ln \rho \propto -W \quad (2.38)$$

This means that during the strain of a material the width of potential barrier increases and consequently the resistance of the composite increases.

2.4.10 Sensing materials: Piezoresistive effect

As mentioned in the introduction of this thesis, sensing materials belong to the class of *smart (or intelligent) materials*. This adjective implies that the material responds in a predetermined way depending on the change of the environment, and piezoresistive materials belong to this category. The piezoresistive effect was reported for the first time by Lord Kelvin in 1856^{322,331} and it is a change of resistance as a mechanical strain is applied. This property is in contrast with the piezoelectric effect which implies a change of potential as tension or compression is applied (**fig.2.31**).^{332–335} Certain types of ceramics display piezoelectric effect and are usually used as transducers,³³⁶ which are devices that change electrical energy into mechanical strain and vice versa.^{81,89}

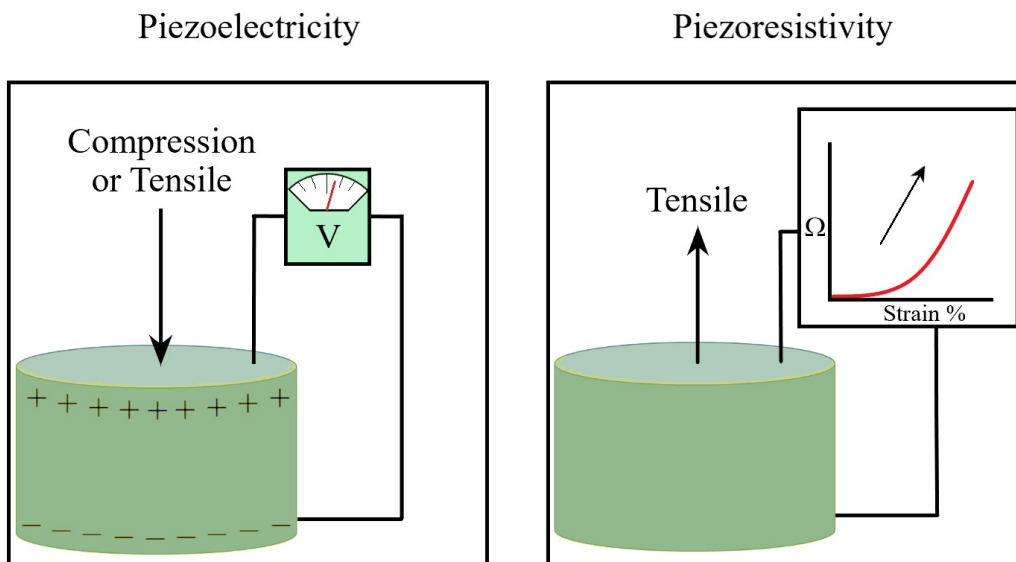


Fig.2.31. Schematic representation of piezoresistive (left) and piezoelectric (right) effect.

In conducting and semiconducting materials, the stress transfer on the materials as a strain is applied induces an alteration in the band gap.^{113,331,337–339} This results in a different motion of electrons (moving them into the conductive band or vice versa depending on the material) that changes the resistance of the material.³³¹ In section 2.4.5, a definition of resistivity, ρ , has been described in relationship with both resistance, R , and specimen area, A , and length, l , and from the equation 2.30:

$$R = \rho \cdot \frac{l}{A} \quad (2.39)$$

When a strain is applied and the resistance changes, this change depends on the resistivity, length and cross-section area variation.³⁴⁰⁻³⁴³ Indeed, because of the Poisson's effect,^{65,82,85,137,138} when a material is deformed it will experience strain in all three axes; therefore, for semiconductors:

$$\frac{\Delta R}{R} = \frac{\Delta l}{l} - \frac{\Delta A}{A} + \frac{\Delta \rho}{\rho} \quad (2.40)$$

Due to Poisson's effect, we can write

$$\frac{\Delta A}{A} = -2\nu \frac{\Delta l}{l} \quad (2.41)$$

where ν is the Poisson ratio (section 2.4.3). Combining eq. 2.40 and 2.41 we can obtain

$$\frac{\Delta R}{R} = (1 + 2\nu) \frac{\Delta l}{l} + \frac{\Delta \rho}{\rho} \quad (2.42)$$

And because we can define the strain as

$$\varepsilon = \frac{\Delta l}{l_0} \quad (2.43)$$

We can rewrite the change of resistance this way:

$$\frac{\Delta R}{R} = (1 + 2\nu)\varepsilon + \frac{\Delta\rho}{\rho} \quad (2.44)$$

For metals, the resistivity does not vary significantly with strain thus, the term $\Delta\rho/\rho$ is negligible. In this case for incompressible materials, such as metals, the $\nu = 0.5$ ^{137,138} and equation 2.44 can be rewritten as:

$$\frac{\Delta R}{R} = G\varepsilon \quad (2.45)$$

where G is called gauge factor.^{344,345} This parameter indicates the sensitivity of the material; thus, we can assume that the higher the gauge factor the better the sensor. Usually, when a tensile strain is applied, this parameter has positive values while it has negative values when under compression.^{82,137} In semiconductors the first term, related to the Poisson's is insignificant. In this case, the resistivity change of (intrinsic) semiconductors is related to the electronic charge, e , number of charge carriers, and the average mobility of the charge carriers:³⁴⁶⁻³⁴⁸

$$\rho = \frac{1}{e(n\mu_n + p\mu_p)} \quad (2.46)$$

Usually, in n-type composites, the electron mobility (μ_n) increases resulting in a resistivity decrease,^{59,66,89,349} while in p-type materials the hole mobility (μ_p) raises with a consequent resistivity increase as a strain is applied (most common behaviour).^{15,65,137,283,350,351}

2.5 DESIGN OF EXPERIMENT

Improving the quality and efficiency of experiments is an important goal in research. Sometimes, it is possible to face situations where a complete study involves considering multiple variables at the same time, as well as potential interactions between them. Using traditional methods of a variable by variable experimentation can become unfeasibly time-consuming and cost-intensive. Design of experiment (DOE) is an effective method for investigating such complex multifactor experiments, and their interactions, in an efficient and statistics-driven process.^{117,124,126,129,130} This method is centred on factors (variables), responses (results), models and runs (tests).^{117,119} To reveal relationships between a factor, or input variable, and a response, or output variable, we deliberately change the former and investigate its effect on the latter. Actively manipulating factors according to a randomised, controlled and pre-determined design is a powerful way to get useful information from the minimal amount of experiments and is the basis of the DOE method. The design of experiments or experimental design was developed by Sir R.A. Fisher¹²⁰, a British statistician and geneticist in 1920. This design explains the variation of information and predicts the outcomes by introducing one or more independent variables defined as input variables. The design may also select control variables which are kept constant to avoid external factors that affect the results.³¹ Furthermore, in 1950, the statistician G. Taguchi developed a method which is an extension of the classic DOE approach. The classic DOE approach comprises two main steps: first, an early phase of investigation to evaluate the experimental factors, responses, and design for viability. Secondly, the use of a more powerful design which considers the non-linear effect of the process, in order to have a profile of the interactions between factors and result, being able to predict the best outcomes of the experiment.¹¹⁷ Moreover, DOE strongly supports an adaptive approach, whereas the Taguchi model is based on the study of one large experiment which also considers some important interactions.³¹ Depending on the type of information we want to obtain, a different strategy can be selected among the two. For instance, DOE is the best option to define the optimal conditions of the process or to connect the response (in our case gauge factor and hysteresis) with the set of process factors and their interaction. Comparatively, the Taguchi model is more suitable to reduce variability around a specified target.³¹ For these reasons, a classic

DOE approach has been utilised in this work. Previously, it was necessary to perform statistical calculation through factorial study, nowadays it is possible to use specific programs able to execute calculations and statistical analysis. In this work a program called Jump (JMP) has been used. We can divide the process in five main steps:

Describe the experiment

For this step is necessary to perform a preliminary study and collect all the information regarding potential input and response variables (i.e. in this work silicone oil viscosity was used as one of the factors for the preparation of multi-matrix strain sensors, while the minimisation of the hysteresis was selected as one of our desired responses). Once we have collected information on all the variables involved, it is necessary to define the factor properties, as well as the desired properties of the responses generated by the DOE method. (i.e. maximise mechanical and/or electrical parameters, **fig.2.32**).

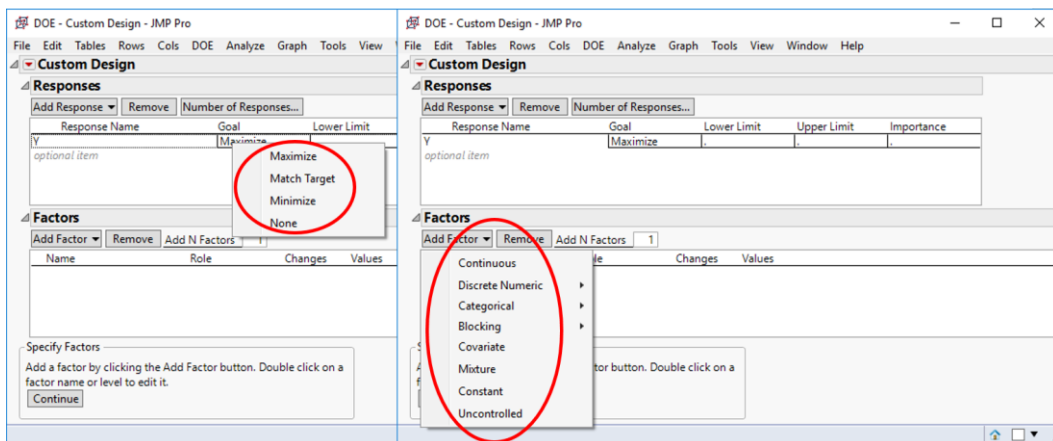


Fig.2.32. First step of DOE where we describe the characteristics of the factors (right) and we define the type of responses we desire (left).

Design

In this key mathematical step, an experimental design is computed and a table with a series of tests to perform is acquired. This design is a randomised sequence of

tests to be performed, also called experimental runs, with each run having a unique set of factor levels. Each column in this table represents an input variable (factor) with each cell corresponding to its factor level in a given run. The numbers -1, 0 and 1 denote one of three possible predefined levels a factor can take in a specific run (i.e. if the temperature is selected as an input factor, the values -1, 0, 1 may represent low, medium and high temperature respectively). Here, the values of the variables are selected from the program in a way to obtain the maximum information from the set of runs, as shown in **fig.2.33**.

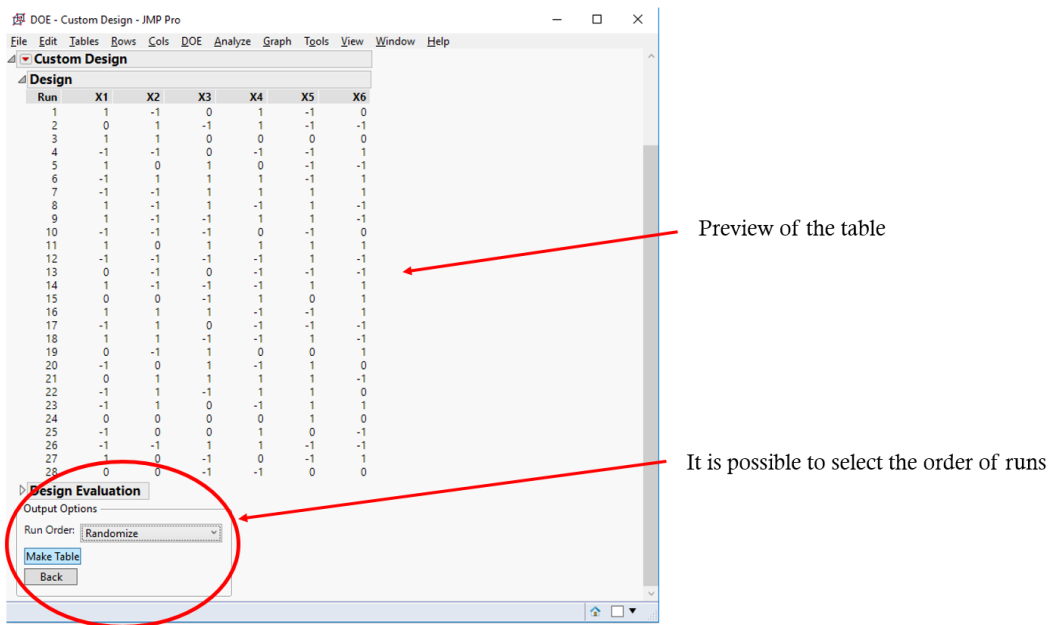


Fig.2.33. Example of a computed table showing a set of 28 experimental runs to study the effect of varying a set of six factors X1-X6 across three defined levels (-1, 0, 1).

Collection

This is the “physical” or experimental part of the procedure, where each experimental run is performed. Here, the results are collected and the observed response for each run is populated in the table (**fig.2.34**).

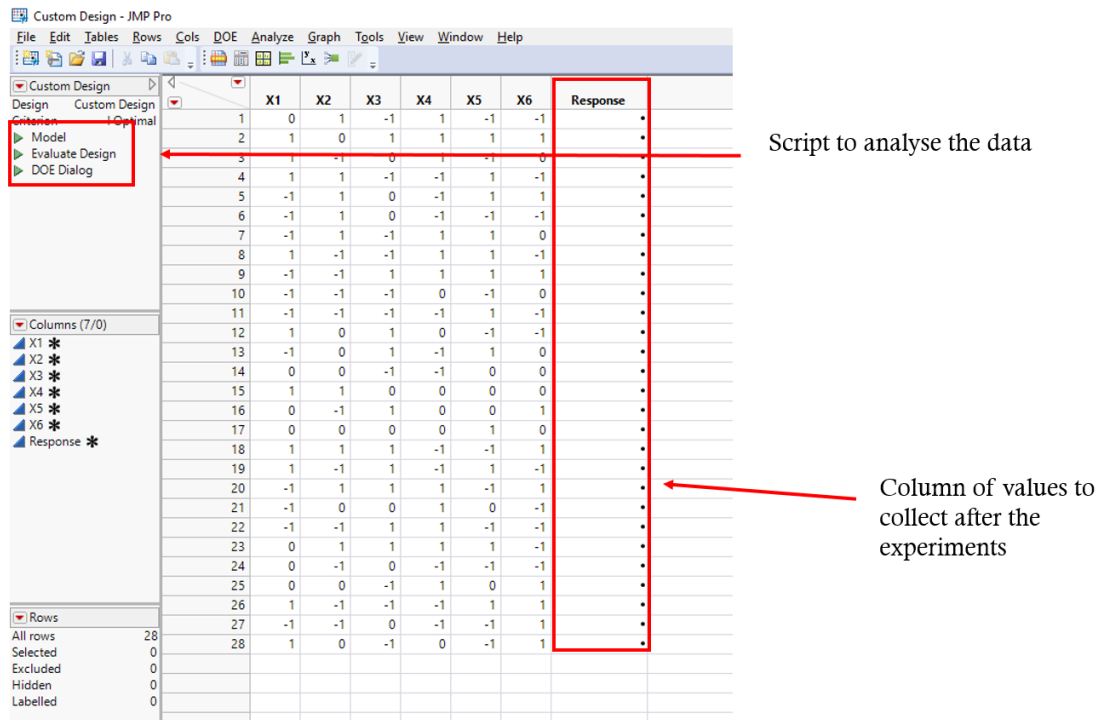


Fig.2.34. Data collection after performing all the runs and reporting the findings in the responses column, it is possible to select a suitable type of model (on the left of the figure) to fit the data.

Fitting the data

After collecting all the responses, it is possible to compute the best fit of a mathematical model to the test run data. This is achieved by selecting the appropriate “personality” depending on the experiment performed, in order to find a pattern and a connection between factors and responses. The “personality” specifies the different mathematical models that are available to select based on the choice of factor type and data (**fig.2.35**).

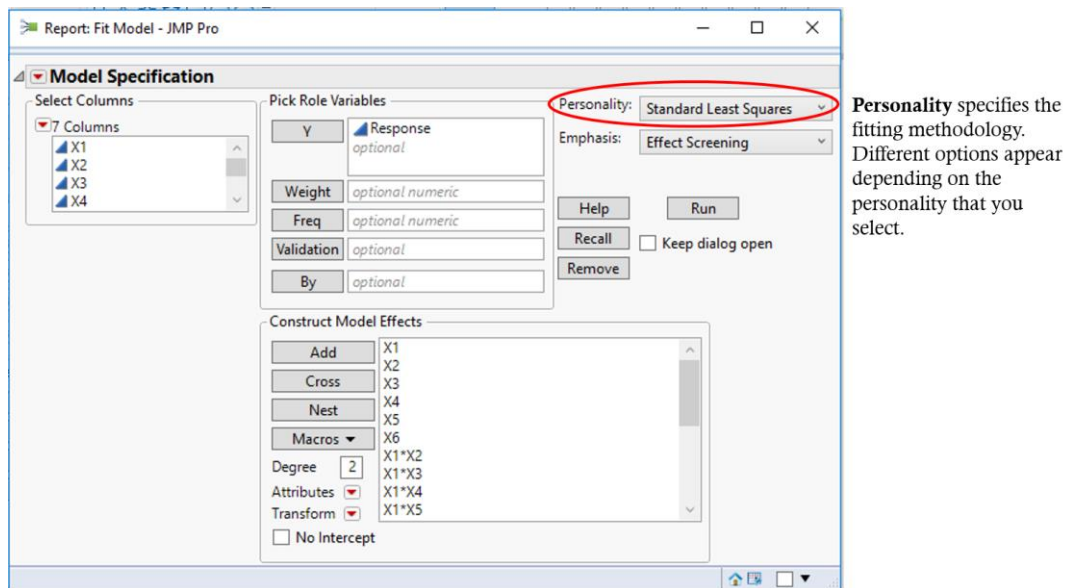


Fig.2.35. Display of model specification to fit the data.

Prediction

Finally, after a mathematical model is selected, it is possible to obtain a prediction profile, which displays the best factor settings for on-target responses and the minimum variability. In this step, it is possible to observe not just the link between factors and responses, but it is possible to generate a “desirability” value, which shows how suitable a determined factor setting is. This means that the higher is the desirability, the closer the values are to the best results (**fig.2.36**).

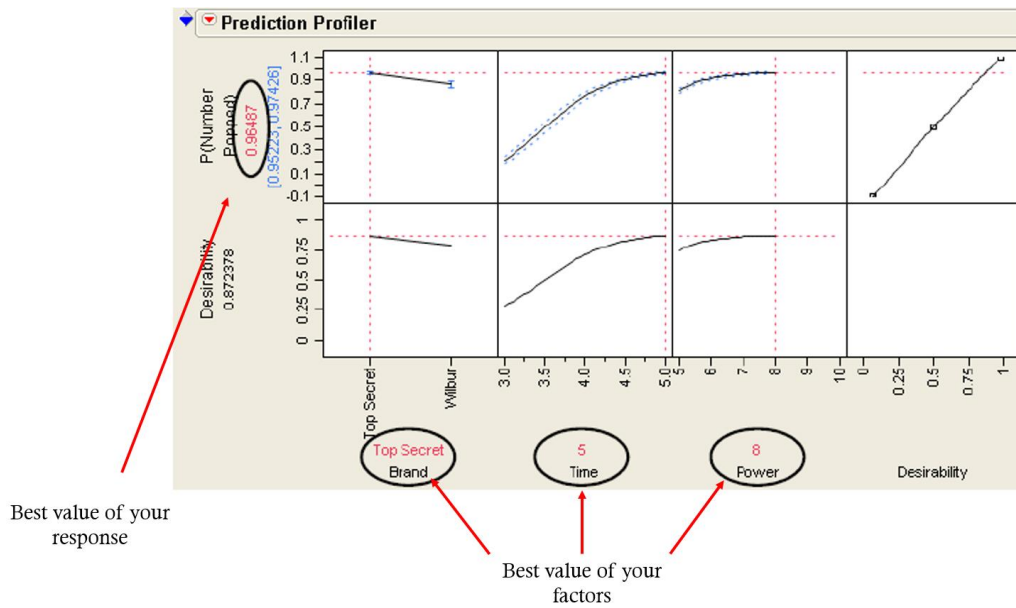


Fig.2.36. Prediction profile of an experiment designed by the program. Factors with the values which give the best results, thus the highest desirability, are reported on the bottom; while the results are reported on the left of the prediction profile.

Materials and Methods

3.1 INTRODUCTION

Discussed in this chapter is the production and characterization of the materials used in this thesis. These materials were exfoliated via ultrasonication and/or shear mixing. The nanomaterials were prepared in three different ways: shear exfoliation in water and surfactant for scaled-up production of WS₂ nanosheets, water ultrasonication stabilized by surfactant for the 2D materials later inserted in a PEO matrix, and solvent stabilized ultrasonication for exfoliated material (DOE project). These nanosheet dispersions are usually polydisperse thus, they can be size selected, or the non-exfoliated material can be simply removed via centrifugation procedures.

The resulting dispersions and prepared nanocomposites are both characterized by a variety of methods. UV-vis spectroscopy was used to find the concentration, length and thickness of nanomaterials, confirmed by other types of analyses such as AFM, TEM and SEM. Raman spectroscopy was performed on both dispersions and composites to examine their chemical nature and finally, electromechanical tests were performed on composites with different filler loading levels to verify their mechanical and electrical response.

3.2 MATERIALS

Poly (ethylene oxide), molybdenum disulphide, tungsten disulphide, sodium cholate hydrate, boric acid, Sylgard 170®, N-methyl pyrrolidone, and isopropanol were purchased from Sigma-Aldrich. Silicone oil at different kinematic viscosities was used: 1000 and 10000 mm² s⁻¹ (referred also as 1k and 10k cst) were purchased from Clearco Products, 100000 mm² s⁻¹ (or 100k cst) was purchased from Sigma

Aldrich. Molybdenum diselenide was purchased from Alfa Aesar, tungsten diselenide was purchased from Fisher Scientific, and graphite was purchased from Asbury Graphite Mills. Each product was used as received.

3.3 SCALED-UP PRODUCTION OF WS₂ NANOSHEETS VIA SHEAR MIXING EXFOLIATION

Dispersions were prepared using a high-shear laboratory mixer (Silverson model L5M-A, 746 W). This model is supplied with a standard mixing assembly, comprising a frame and base plate holding a four-bladed rotor and a stator with 96 square perforations (2×2 mm). The rotor-stator gap for the assembly used was ~110 μm. Centrifugation was performed using a Thermo Scientific centrifuge (Heraeus Megafuge 16) with a TX-400 swinging bucket rotor (max 5000 rpm) and a Hettich Mikro 220R centrifuge with a high-speed rotor for size selection. Optical absorbance spectroscopy was performed with samples held in a 4 mm path length quartz cuvette using a UV-Vis-NIR spectrophotometer (Varian Cary 500) in 0.5 nm wavelength increments. Raman spectroscopy was performed using a Horiba Jobin Yvon LabRAM-HR with a 100x objective lens and 633 nm laser excitation. TEM samples were prepared on holey carbon grids and the analysis was performed using a JEOL 2100, operated at 200 kV.

Preparation of WS₂ dispersions

WS₂ dispersion preparation is comprised of two steps, and the first is called the pre-treatment stage (PT) to remove impurities present in the material. After the first shearing, the dispersion was left overnight to settle down. Then, the supernatant is removed, the sediment re-dispersed in fresh DI water, and subjected to the final shearing. The standard sample was prepared using the following parameters: a 32 mm rotor diameter (D), initial WS₂ concentration (C_i) of 20 mg ml⁻¹, a NaC concentration (C_s) of 0.8 mg ml⁻¹, a pre-treatment shearing time (PT-t) of 90 minutes, the shearing time (t) used was set at 90 minutes, the rpm was set at 6000

for the pre-treatment stage (PT-N) and at 9000 for the shearing stage (N), and the volume (V) used for both pre-treatment and shearing was 300 mL.

To test the effect of processing parameters, a standard sample was established and two parameters, PT-t and PT-N, were kept constant while the other five parameters were varied individually. Furthermore, the volume was varied in both the PT and the shearing step and the rotor diameter was kept constant (32 mm) because it was found that it was not possible to exfoliate WS₂ using smaller rotors.³⁰

Centrifugation process

The dispersion preparation is followed by size selection using the centrifuge speed (2-10 krpm) to select a particular range of particle dimensions. The supernatant was collected after the shear mixing and centrifuged at 2000 rpm for two hours. After that, the supernatant was collected and the sediment, with unexfoliated material, discarded. Again, the supernatant was centrifuged at 10 krpm for two hours and the sediment was collected and re-dispersed in water. The final dispersion volume was then analysed.³⁰

3.4 COMPOSITE PREPARATION (PEO/TMDs/GRAPHENE)

In this project, TMDs and graphite powder (20 g/L) were sonicated in water for 1 h using a solid flathead tip (Sonics VX-750) at 60% amplitude with a pulse of 6 s on and 2 s off duty cycle. The dispersion was centrifuged for 2 h at 6000 rpm to separate low-mass impurities into the supernatant using a Hettich Mikro 220R centrifuge with a fixed-angle rotor. The supernatant was discarded and the sediment redispersed in 2 g/L sodium cholate aqueous solution by sonication for 330 min using the same sonic tip settings as previously described. Following this, the dispersion was centrifuged at 1000 rpm to transfer unexfoliated material to the sediment, leaving large nanosheets in the supernatant. The optical characterization of nanosheet dispersions was performed in a 4 mm path length quartz cuvette using a UV-vis spectrophotometer (PerkinElmer Lambda 650). Raman analyses were performed with a Horiba Jobin Yvon LabRAM HR800 (100× objective lens, travel

spot size $\sim 1 \mu\text{m}$, $\lambda = 532 \text{ nm}$) under ambient conditions. TEM analyses were performed on dispersions using a JEOL 2100, operated at 200 kV with holey carbon grids as substrates. SEM analyses were performed on composite PEO/MoS₂ films using a SEM Carl Zeiss Ultra operating at 2 kV. A Veeco Nanoscope-IIIa system (Digital Instruments) was used in tapping mode AFM measurements. Samples were prepared by drop-casting 15 μL of diluted dispersion (O.D. approximately 0.4) onto a preheated, cleaned Si/SiO₂ wafer (285 nm oxide layer) at 180 °C. Wafers were washed with water to remove excess surfactant. Nanosheets were then analysed individually using previously established length corrections for pixelation effects and tip broadening.¹⁹¹ Step height analysis was used to convert the apparent thickness of nanosheets to the number of layers using a step height of 1.9 nm. The nanosheet thickness was then found by multiplying the number of monolayers per nanosheet by 0.6 nm. Electromechanical analysis on composite films was executed using a Keithley KE2601 source meter in a 2-probe mode, controlled by Lab-View software, in conjunction with a Zwick Z0.5 Pro-Line Tensile Tester (100 N Load Cell).³²⁰

Film preparation

Different ratios of polymer-nanosheet composite films were prepared. Specific volumes of nanosheet dispersions were mixed with PEO/H₂O solution. Water was added, keeping the total volume constant (15 mL), and the nanosheet-polymer dispersion was poured into a Petri dish and dried overnight at 50 °C. The films obtained looked macroscopically uniform and were then analysed.³²⁰

3.5 DESIGN OF PIEZORESISTIVE MULTI-MATRIX STRAIN SENSORS (PDMS/SYLGARD/GRAPHENE)

The composites were prepared using different ratios of a commercial elastomer (Sylgard 170) and PDMS (polydimethylsiloxane) while the graphene concentration was kept constant. Graphite powder (20 g/L) was sonicated in NMP for 72 h using a solid flathead tip (Sonics VX-750) at 60% amplitude with a pulse of 6 s on and 2 s off duty cycle. The dispersion was centrifuged for 1 h at 1500 rpm to remove

unexfoliated material using a Hettich Mikro 220R centrifuge with a fixed-angle rotor. Afterwards, the graphene was filtered and redispersed in IPA.

Composite preparation

The PDMS was prepared by adding a specific amount of boric acid to the silicone oil. Different viscosities of silicone oil were used to prepare the samples (1000, 10000 and 100000 cst). The PDMS was prepared following previous studies by crosslinking the silicone oil in an oil bath at ~215 °C for 2 hrs.¹³⁸ Afterwards, the PDMS was dissolved in IPA and a specific amount of graphene was added to the polymer. Sylgard 184 was added, the mixture was transferred on a Teflon dish, and the solvent was evaporated overnight at room temperature. Finally, the sample was cured at 100 °C for 2.5 hrs and subjected to electromechanical tests. Also in this case, the electromechanical analysis was executed using a Keithley KE2601 source meter in a 2-probe mode, controlled by Lab-View software, in conjunction with a Zwick Z0.5 Pro-Line Tensile Tester (100 N Load Cell). A table with specific parameter values was prepared using DOE (**table 3.1**), the composites realized using that table and characterized.

Table 3.1. *Designed tests obtained from the DOE after the preliminary study.*

Graphene wt. -%	Sylgard wt.-%	PDMS wt.-%	Oil Viscosity (cst)
12.5	30	57.5	10k
12.5	30	57.5	100k
12.5	77.5	10	100k
12.5	30	57.5	1k
12.6	77.4	10	10k
12.6	77.4	10	1k
12.6	77.4	10	100k

3.6 CENTRIFUGATION

After using either sonication or shear mixing, dispersions produced are polydispersed and still contain large amounts of unexfoliated, unstable dispersed material. In order to characterise exfoliated nanosheets, it is necessary to separate the produced nanosheets from bulk material. A way to size select dispersions is via sequential centrifugation cascade. Our group has shown in previous studies the efficiency of this method, size-selecting a large range of 2D exfoliated materials in several solvents.^{19,191,192} Centrifugation consists of rotating a sample about a fixed axis at a certain speed, usually expressed in rotations per minute (RPM) which is a relative measure to specific centrifuges. However, it is possible to convert RPM to another unit that can be used across different types and sizes of centrifuges. This is called relative centrifugal force or G-force (RCF). This parameter is dimensionless and is related to the gravitational force, g , the radius of the rotor, r , and the angular rotation w :

$$RCF = \frac{w^2 \cdot r}{g} \quad (3.1)$$

where $w = 2\pi N$ and here, N is the rotation rate in rotations per second. Thus, it is possible to convert RCF to RPM (and vice versa) with the equation:

$$RCF = 1.118 \times r \times \left(\frac{RPM}{1000} \right)^2 \quad (3.2)$$

with the radius r , expressed in mm.

3.7 UV-VIS SPECTROSCOPY

Optical absorption spectroscopy is a technique based on light interactions with a sample. In particular, the light can interact in three ways: it can be absorbed by the

sample, transmitted, and/or scattered. This is the foundation of UV-vis spectroscopy where a cuvette containing a sample is able to decrease the exit intensity of a light beam through absorption and/or scattering effects. This light intensity decrease due to absorption and scattering effects is called extinction. During analysis, the light of different wavelengths that passes through the sample is collected and the irradiance difference between the sample input beam and cuvette output beam is detected and measured.³⁵²

This type of spectroscopy is a very common method used to analyse nanomaterials exfoliated in liquids and it exploits the Lambert-Beer law.³⁵³ For solution, the scattering is minimal thus, absorption and extinction match and Lambert-Beer law can be expressed by the following equation:

$$A = \varepsilon cl \quad (3.3)$$

Here, A is the absorbance of the dispersion, ε is the extinction coefficient (typical of each material), c is the concentration of the nanomaterial in the liquid and l is the path length (section of the cuvette where the light passes through). However, for colloidal dispersions, the presence of scattering effects influences the result of the UV-vis absorption spectra thus the Lambert-Beer law can be used to find the absorption by:

$$A = \alpha cl \quad (3.4)$$

Where α is the absorption coefficient. In the same way, the extinction is described by this equation:

$$Ext = \varepsilon cl \quad (3.5)$$

As previously mentioned, the extinction is related to both absorption and scattering and in many solutions, scattering is minimal so extinction is mainly dependent on absorption. However, for nanomaterials dispersed in liquids, scattering contributes an appreciable amount, and therefore one must consider absorption as well as scattering which is done through the equation:

$$\varepsilon(\lambda) = \alpha(\lambda) + \sigma(\lambda) \quad (3.6)$$

where $\varepsilon(\lambda)$, $\alpha(\lambda)$ and $\sigma(\lambda)$ are extinction, absorption and scattering coefficients, respectively (**fig.3.1**). This distinction is very important during the nanoparticle analysis, since the spectra can change intensely depending on nanoparticle size. For this reason, it is necessary to use an integrating sphere attachment which allows for the removal of the scattering contribution from the extinction spectra. Here, the scattered light is reflected by the coating that covers the internal walls of the sphere, where the cuvette is positioned, and it is received as transmitted light.³⁵⁴

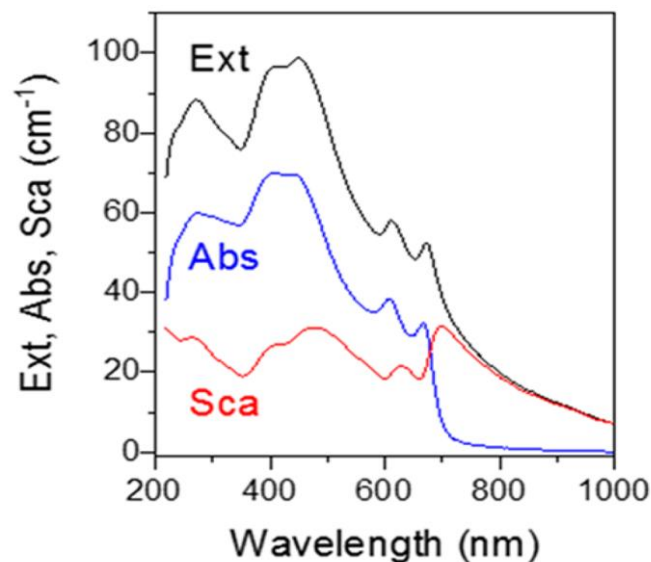


Fig.3.1. Extinction (in black), absorption (in blue) and scattering (in red) spectra of MoS₂ in water and surfactant. The “tail” at large wavelengths, indicative of scattering, is typical for large nanoparticles.⁵⁹

3.8 RAMAN SPECTROSCOPY

As previously mentioned, light scattering is a phenomenon that can occur when light is absorbed and re-emitted by a material. However, two different types of scattering we consider here are Rayleigh scattering and Raman scattering. Rayleigh scattering occurs when the photon emitted has nearly the same wavelength or energy as the incident photon used for probing; so, the emitted photon is essentially elastically scattered. Raman scattering takes place when the emitted photon has a different wavelength than the incident probe photon or is inelastically scattered. Raman scattering and the spectroscopy which harnesses this concept are named after Sir C.V. Raman, who observed the scattering phenomenon in 1928 and for which he received the Nobel prize in 1930.³⁵⁵ Since then, it has become one of the most important techniques for identifying compounds based on their vibrational modes. The technique involves the use of a monochromatic beam, incident upon a sample, which can be either absorbed, reflected or scattered. Moreover, if during the scattering energy is transferred from the incident photon to the molecule or from the molecule to the photon, producing lattice vibrations, this will result in scattered radiation with a different frequency/wavelength.¹³³ This change of energy provides a large variety of information about the sample from chemical structure to chemical bonding, and environmental effects such as stress and strain.^{317,318,356}

There are two types of Raman scattering: Stokes and anti-Stokes (**fig.3.2**). In each case, the photon scattering interaction excites the probed molecule to a virtual energy state. If the molecule relaxes to a real phonon state and emits energy with less than that of the incident photon, it is termed Stokes scattering. However, if the molecule's virtual energy state is reached from the molecule already being in a phonon excited state, and the molecule emits a photon higher in energy than the absorbed photon after it relaxes back down to the ground state, it is known as anti-Stokes scattering.

A peculiarity of these scattering paths is that in Stokes Raman scattering, the molecules are excited from the ground state to the higher energy state, and when the photon is re-emitted, the energy goes to another vibrational state. In anti-Stokes Raman scattering, some molecules are already in an excited state, caused by thermal

energy, and scattering to the ground state produces a transfer of energy to the photon.³⁵⁵

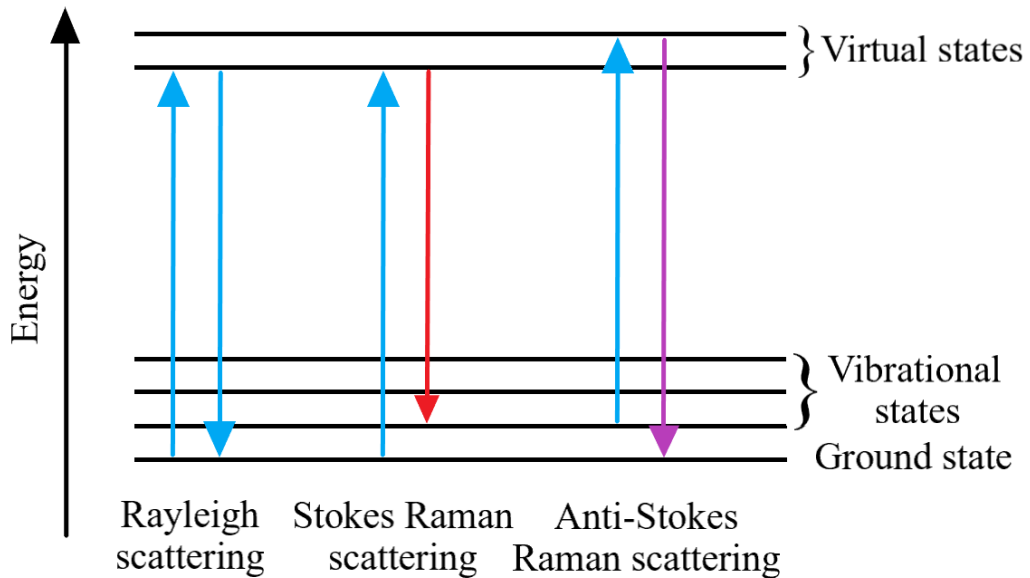


Fig.3.2. *Graphic representation of Rayleigh and Raman scattering.*

3.9 TRANSMISSION ELECTRON MICROSCOPY (TEM)

Transmission electron spectroscopy is a very important analysis technique. It is largely used in LPE analysis because it is an excellent method to verify the produced nanosheet quality.^{19,52,163,192,320} While techniques such as UV-vis and Raman spectroscopy harness the interaction of the matter with light, TEM measures the electron interaction with samples. Indeed, it was De Broglie’s work in 1927 that lead to the basic theory of TEM technology.³⁵⁷ In his work, he realized that electrons display a wave-like behaviour and thus, they could be used in microscopy as the wavelength of electrons e^- is given by:

$$\lambda = \frac{1.22}{E^{1/2}} \quad (3.7)$$

where λ is the wavelength and E is the energy of an electron. TEM works by the emission of an electron beam from a heated filament (usually tungsten or LaB₆) through a column of electromagnetic lenses onto a sample (**fig.3.3**). Here, the beam interacts with the sample producing a series of secondary interactions (i.e. backscattered electrons, Auger electrons, secondary electrons, etc.), but also the electrons can be transmitted through the sample, while being scattered or not. Afterward, the electrons transmitted through the sample are detected by a CCD camera and converted into an image (**fig.3.4**).³⁵⁸ The image formation is analogous to the optical microscope, however, the advantage of using TEM over optical microscopy is simply the higher resolution the TEM allows. This can be explained through the Abbe diffraction limit which states that the wavelength of the wave used to image an object is proportional to the dimension, d , of the object one is trying resolve.²⁴⁵

$$d \approx \frac{\lambda}{2} \quad (3.8)$$

Thus, the smallest objects that can be resolved with an optical microscope ($\lambda = 400 - 800$ nm) has a dimension of 200 nm. From equation 3.5, it is possible to theoretically work out that the resolution of the smallest object for 100 keV is 2 pm, but the presence of aberration limits the resolution to ~ 0.3 nm.

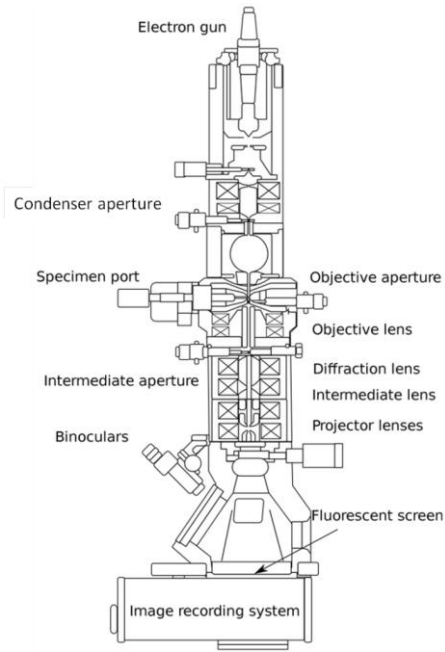


Fig.3.3. Schematic of a TEM column. ³⁵⁸

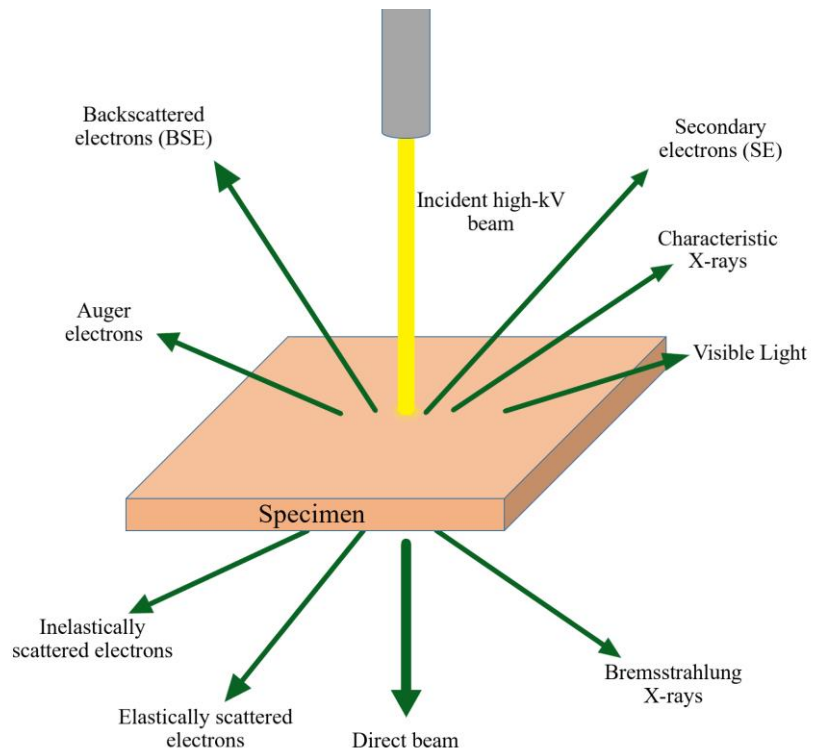


Fig.3.4. Possible outcomes after an electron beam interacts with the specimen.

3.10 SCANNING ELECTRON MICROSCOPY (SEM)

Another common high resolution technique similar to TEM is scanning electron microscopy (SEM). Like the TEM, this tool harnesses electron beams accelerated with high voltage and focuses the beam using electro-magnetic lenses, with the purpose of imaging the sample. However, there is a difference between the two methods. SEM is a technique where the focused beam is scanned on the surface of the specimen, and back scattered electrons from the sample are detected and collected to image the surface. While the TEM passes through the sample and several types of electrons are collected.³⁵⁹

Moreover, SEM, as well as TEM, provides electrons that are characteristically emitted by tungsten or LaB₆ into a column under vacuum and accelerated by an applied potential. The beam is then scanned over the sample by the scanning coil which controls the imaging process. When the beam interacts with the specimen, backscattered electrons and secondary electrons are mainly used for the imaging; whereas, Auger electrons and X-rays can be collected for other sample characterization. Secondary electrons are emitted by the sample due to inelastic collisions with the electron beam, and these are particularly surface sensitive while backscattered electrons are less surface sensitive. Indeed, backscattered electrons are high energy electrons elastically scattered by the sample. A simple diagram illustrating a scanning electron microscope can be seen in **figure 3.5**.

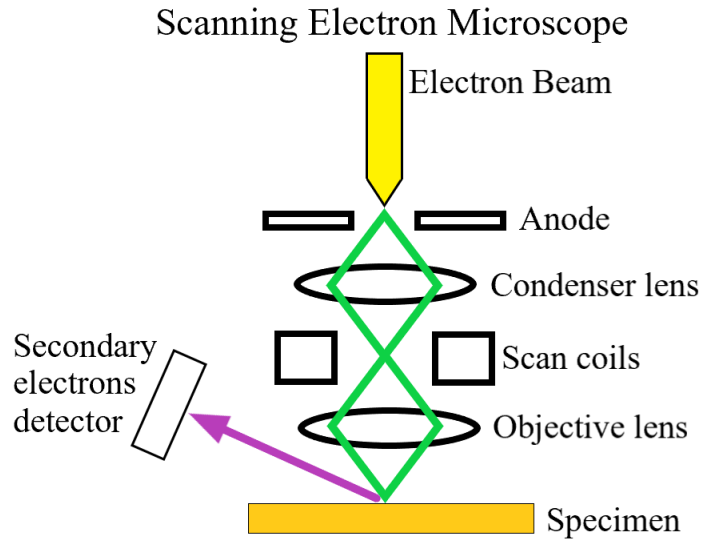


Fig.3.5. Schematic representation of a SEM column.

3.11 ATOMIC FORCE MICROSCOPY (AFM)

Atomic force spectroscopy (AFM) is a common technique very important for 2D nanosheet characterization.^{11,19,191} In fact, this scanning probe tool is able to map the topography of a sample displaying important information such as the thickness and length of the nanosheets.^{41,360,361} Unlike the other analysis methods previously described, AFM does not use electron nor photon beams, but instead a sharp-tipped cantilever that is scanned over a sample surface. As the cantilever is moved across the surface of a sample, variations in the topography cause vertical deflections. These deflections are observed and amplified by reflecting a laser beam off the back of the cantilever which is detected by a photodiode (**fig.3.6**). Once detected, this tip displacement is converted into an image.³⁶¹

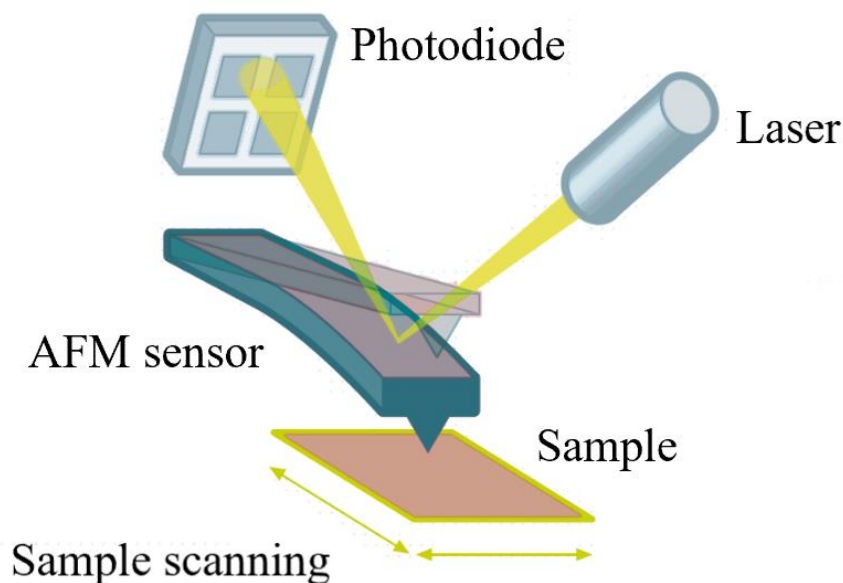


Fig.3.6. *General representation of AFM operation.*³⁶¹

There are three operational modes: contact, non-contact and tapping mode. In the contact mode, the tip is lowered down very close to the sample surface, and as the tip is “dragged” across the surface the repulsive forces cause the deflection of the tip. This method facilitates fast imaging and it is used for high image resolution but it also carries the risk of both tip and sample damage. During non-contact mode, the tip is positioned nanometres above the surface, and when it passes above an object, attractive forces cause the deflection of the tip. This method is complex to execute since the tip has to be kept close to the surface while avoiding the repulsive region.³⁶¹ Moreover, there is a resolution decrease and it is largely affected by the water unavoidably situated on the surface. A method that can find a middle ground between the two techniques, obtaining high resolution without damaging the tip nor the sample, is the tapping mode (also called intermittent contact mode). In this mode, the cantilever oscillates at its own frequency alternating the non-contact with the contact mode, eliminating the frictional forces thus preventing the tip from being trapped by contaminants. In this thesis a Veeco Nanoscope-IIIa system (Digital Instruments) was used in tapping mode for AFM measurements.³⁶¹

3.12 ELECTROMECHANICAL TESTING

Composite films were cut and uniform strips were obtained (strip width = 2.25 mm). The strips were attached to the clamps of the tensile tester at a 9.73 mm gauge length. These clamps were also connected to a source meter for electrical measurements (**fig.3.7**). For all samples made, the zero-strain conductivity was measured before measuring the tensile strain. Afterwards, the samples were strained (10 mm/min test speed) and both the stress and electrical resistance of the samples were recorded. From the stress-strain curves, it was possible to evaluate Young's moduli using TestXpert software. Using R- ϵ curves, it was possible to plot $\Delta R/R_0$ versus strain and by evaluating the slope of the graph, G values were extrapolated. A sine wave simulation program was used in order to execute cyclic tests on the composite films. A minimum number of 7 tests per sample were performed, then the average and standard deviation were calculated using Origin software.

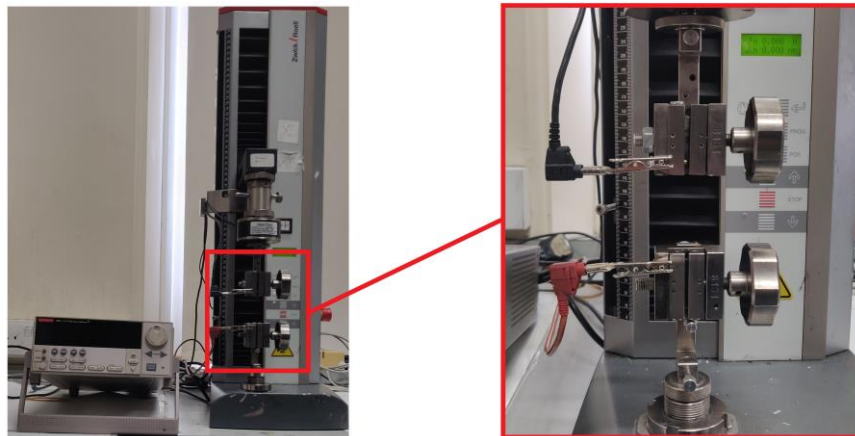


Fig.3.7. Tensile tester/source meter apparatus (left) and zoom in of the clamps (right).

Exfoliation of 2D Materials by High Shear Mixer

4.1 INTRODUCTION

As previously mentioned, Tungsten disulphide is a layered material belonging to the TMDs class. This material is used in a considerable amount of applications such as the fabrication of electronic devices e.g. batteries, transistors and supercapacitors.^{25,49,143,161,190} For this reason, a scalable production method is needed. Stated in chapter **2.1**, previous work demonstrated that this can be achieved for other layered materials such as graphene, boron nitride and MoS₂.^{20,203,217} In fact, it has been found that this goal can be accomplished by exploiting LPE, in particular via shear mixing exfoliation.^{20,30,49,183,362–365} In this work, WS₂ nanosheets were obtained using a Silverson shear mixer (L5M-A series) and sodium cholate (NaC) was used to avoid the reaggregation of the nanoparticles.³⁰

However, it is particularly important to know what controls the WS₂ nanosheet production for two main reasons: to maximise both WS₂ concentration and the production rate of the method. The production rate (P_R) is a particularly relevant parameter in industry and is essential to gauge the feasibility of scaling up any production method; it can be obtained using this equation:²⁰

$$P_R = \frac{CV}{t} \quad (4.1)$$

where C is the concentration of exfoliated nanosheets, V the volume of the dispersion and t the shearing time. Moreover, the properties of shear-mixed dispersions have a tendency to scale with processing parameters as power laws.²⁰⁹ *Paton K. et al.*²⁰ showed how graphene concentration scales following this formula:

$$C \propto C_i^\chi N^n V^\nu t^\tau D^d \quad (4.2)$$

Here, C_i is the initial concentration of the material, N is the shear rate necessary for the exfoliation (in our case the shearing step, **section 4.2.2**) and D is the rotor diameter. In our case, it was not possible to include the diameter parameter because there was no exfoliation using rotors smaller than 32 mm. Thus, having D constant, we can consider the WS_2 scaling depending just on C_i , N , V , and t , producing the equation:³⁰

$$C \propto C_i^\chi N^n V^\nu t^\tau \quad (4.3)$$

In this thesis, each parametric dependence was studied in order to find each exponent and to build an equivalent final equation.³⁰ A standard sample was settled with specific values reported in **table 4.1** and **table 4.2**. The parameters involved in the exfoliation process were varied one at the time from the standard while keeping the others constant. WS_2 dispersion preparation is comprised of two stages; the first is a pre-treatment stage (PT). This stage was necessary in order to remove impurities that may be present in the starting material. After that, the dispersion was left overnight to settle down. Finally, the supernatant was removed, the sediment re-dispersed in fresh DI water, and subjected to the final shearing (**fig.4.1**).³⁰ However, in order to avoid temperature increase during the exfoliation process that can cause possible undesired reactions (i.e. oxidation), each sample was immersed in a cooling system (ice bath) in both pre-treatment and shearing steps.

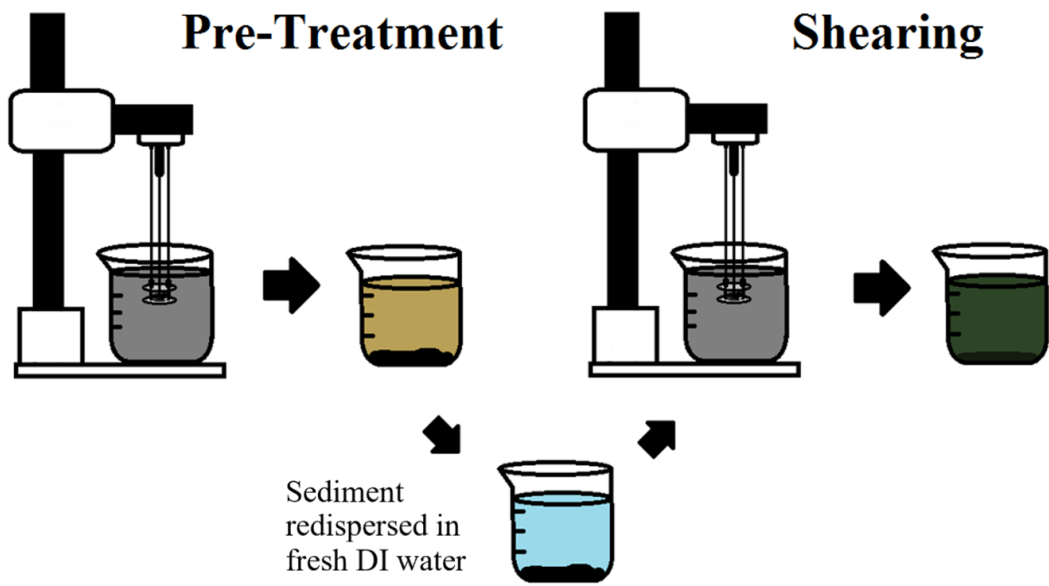


Fig.4.1. Graphic representation of WS_2 preparation.



Fig.4.2. Images of impurities collected after pretreatment (a) and exfoliated WS_2 after the shearing stage (b).³⁰

4.2 PROCEDURE

4.2.1 Pretreatment

All the samples prepared were subjected to a pretreatment step and to do so, WS_2 was dispersed in water and surfactant. The surfactant concentration, C_s , and initial

concentration of WS_2 , C_i , were varied solely in this step and the values of this variation are reported in **table 4.1**. Moreover, the volume of dispersion was varied in the same way in both pre-treatment and shearing steps (**table 4.1** and **table 4.2**). The shear rate, N , and the shearing time, t , were kept constant in this stage at 6k rpm and 90 minutes, respectively (**table 4.1**), for the preparation of all the samples. These two parameters were varied just in the shearing step (**table 4.2**). All the information related to the pretreatment parameters variation are defined in **table 4.1**.³⁰

Table 4.1. *Parameters description of the pretreatment step.*³⁰

Pretreatment Parameters	C_s (g/L)	C_i (g/L)	V (L)	N (krpm)	t (mins)
Standard	0.8	20	0.3	6	90
	0.1	5	0.4	-	-
	0.3	10	0.75	-	-
	0.5	35	1.75	-	-
	0.9	60	2.5	-	-
	1.2	100	3.25	-	-
	1.5	-	4	-	-
	2	-	-	-	-

4.2.2 Shearing step

As previously mentioned, the dispersion was left to settle down overnight after the pretreatment stage. After removing the supernatant, the sediment was re-dispersed in fresh DI water always using the same volume utilized in the pretreatment step. The samples were then subjected to the shearing step.

The factors which needed to be varied in this step for the experiment purpose were volume, V , shear rate, N , and shear time, t . To evaluate the effects that both shear rate and time had on the WS_2 concentration and dimensions, these two parameters were varied in this phase and the values are stated in **table 4.2**. Here, the standard values are highlighted in green.³⁰

Table 4.2. Parameters description of the shearing step.³⁰

Shearing Parameters	V (L)	N (krpm)	t (mins)
Standard	0.3	9	90
	0.4	4	10
	0.75	4.5	20
	1.75	5	30
	2.5	6	60
	3.25	7	180
	4	8	360
	-	8.5	-

4.3 RESULTS

In each study, the concentration, thickness (in layers) and length of nanoparticles were found via UV-vis spectroscopy. Due to the sample preparation procedure, the final concentration of NaC was unknown, and considering the fact that the baseline in optical analysis is required, just water was used as blank. Moreover, it was not possible to use the formulae found by *Backes et al.*^{48,163} because they relate the concentration and the thickness to a specific wavelength in which the surfactant absorbed. For this reason, another equation was extrapolated from the same metric using a different wavelength (350 nm) to find the extinction coefficient.^{30,48} **Figure 4.3** shows the relationship between the calculated extinction coefficients of WS₂ A-exciton, $\varepsilon_{A\text{-exciton}}$, and the ratio of the extinction values (took from the UV-vis spectra) at the wavelength of the A-exciton, Ext_A , and at 350 nm, $Ext_{350\text{nm}}$, obtained from Backes et al. work.⁴⁸ This trend was fitted and the resulting equation extrapolated allows us to compute the extinction coefficient of all of our samples and consequently, to calculate the concentration.^{30,48}

$$\varepsilon = -9.73 + 54.67 (Ext_A / Ext_{350})^{0.757} \quad (4.4)$$

Here, the extinction coefficient ε is in units $L \cdot g^{-1} \cdot cm^{-1}$.^{30,48}

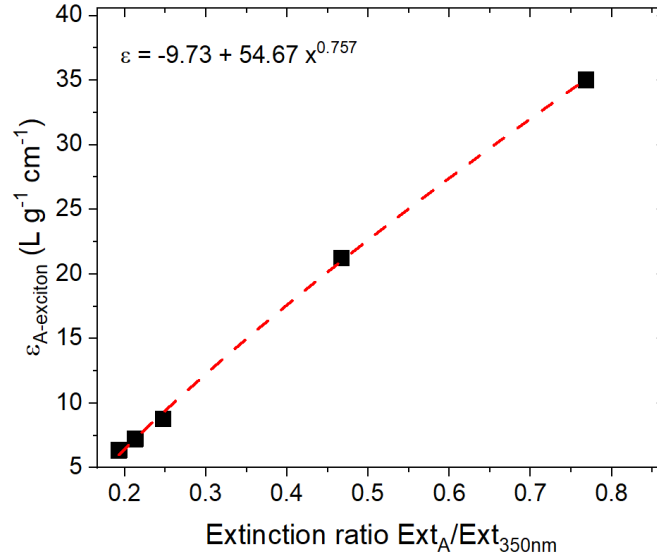


Fig.4.3. Plot displaying how extinction coefficient varies with ratio of extinctions at A exciton and at 350 nm.³⁰

From the same work, it was possible to extrapolate the data and modify the metric to calculate L (**fig.4.4**), yielding the following equation:^{30,48}

$$L = \frac{(3.69 - (Ext_{365} / Ext_{465}))}{(0.011 \times (Ext_{365} / Ext_{465}) + 0.0011)} \quad (4.5)$$

where L is in nm.^{30,48}

The mean layer, $\langle N \rangle$, was calculated using the previous metric. In this case, there was no need to modify any equation from *Backes et al.* work⁴⁸ because, it relates the thickness to wavelengths out of NaC absorption range and the same metric was used again here:^{30,48}

$$\langle N \rangle = 6.35 \times 10^{-32} e^{\lambda_A (nm)/8.51} \quad (4.6)$$

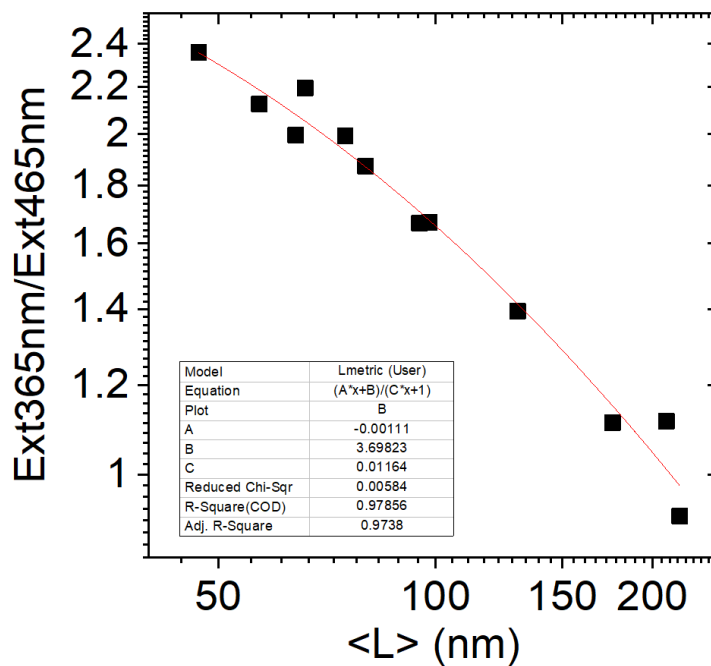


Fig.4.4. Ratio of extinction at 365 nm and 465 nm plotted as a function of the flake size found using TEM statistics.^{30,48}

Also TEM analysis was performed on the standard sample finding a mean length of ~56 nm while Raman spectroscopy was executed to verify the quality of the exfoliated material (**fig.4.5**).

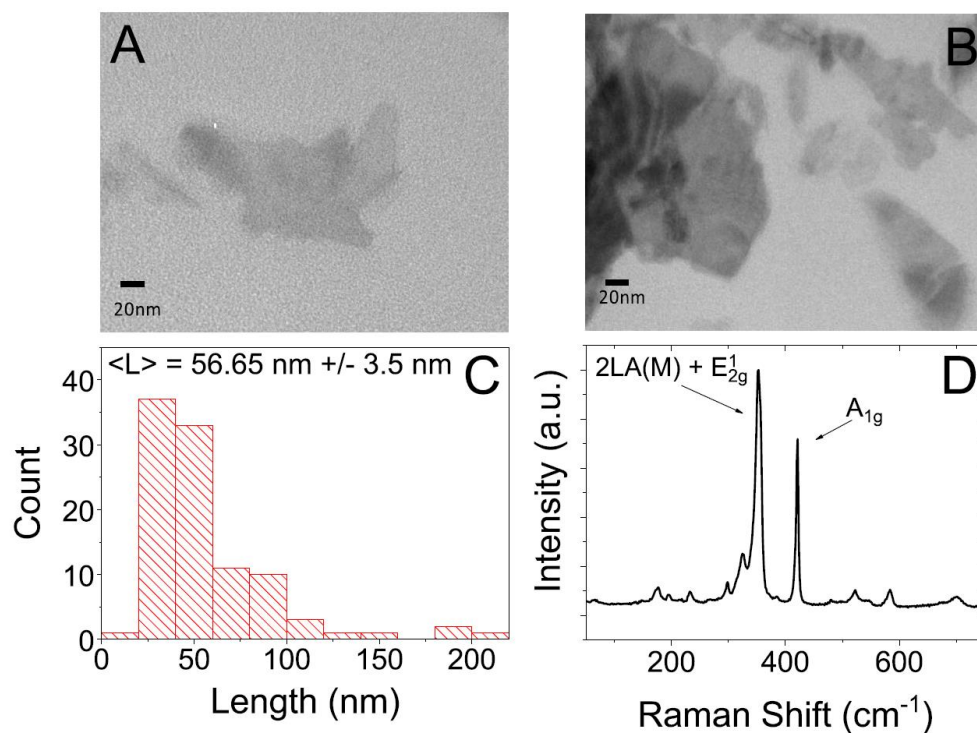


Fig.4.5. Representative TEM images (A and B) and relative histogram (C) of WS₂ nanoparticles. Raman spectrum of standard sample of WS₂ in H₂O/NaC showing the typical WS₂ peaks: in plane E_{2g}¹ mode ($\sim 350 \text{ cm}^{-1}$) and out of plane A_{1g} mode ($\sim 420 \text{ cm}^{-1}$).³⁰

4.3.1 Surfactant concentration variation

The first experiment was the study of the concentration of WS₂ versus the surfactant concentration in order to maximise the concentration of WS₂. In this case, samples were prepared changing the concentration of NaC in the pre-treatment step and keeping all the other parameters constant. Concentration, length, and thickness of WS₂ particles were calculated from the UV-vis spectra performed on the dispersions (**fig.4.6**). The graph below shows that the dependency of nanosheet concentration does not follow a power-law dependency as the other parameters but is peaked, reaching a maximum at C_S = 1.2g/L (**fig.4.6 C**). By analysing the dependency of the size on the NaC concentration from **figure 4.6 B and D**, we can deduce from optical analysis that both the particle thickness and length of WS₂ decreases as the NaC concentration increases. However, due to the excess foam

which often occurred during the shearing stages, we chose a concentration of NaC equal to 0.8 g/L as a standard parameter.³⁰

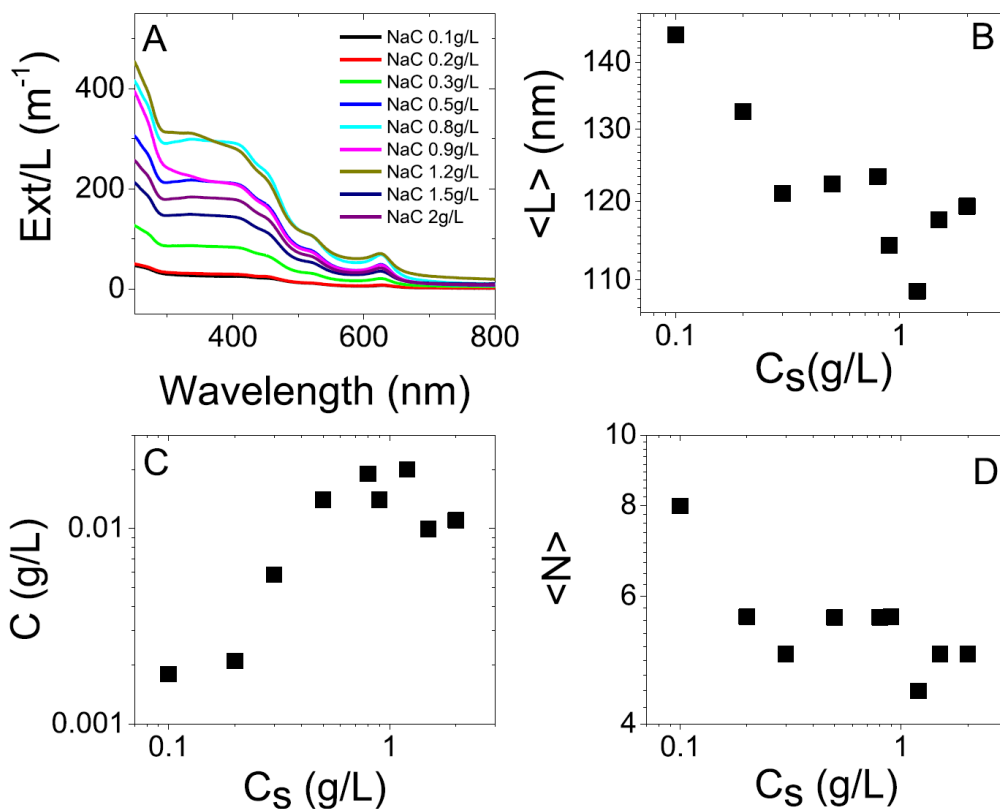


Fig.4.6. UV-vis spectra (A), mean length (B), concentration (C), and mean layers (D) of WS₂ nanosheets vs the NaC concentration.³⁰

With the purpose of finding the exponents for the scale-up equation, rotation rate, N , initial WS₂ concentration, C_i , volume, V , and shear time, t , were varied individually keeping the other parameters constant.^{20,30,209}

4.3.2 Shear rate variation

To allow us to find the exponent relative to the rotation rate, N , several samples were prepared varying the rate of the shearing process.

The graph in **figure 4.7 B** confirms the concentration of exfoliated WS₂ grows as the shear rate increases. We can also see that the concentration does not change

considerably up to 7000 rpm and after that, rises significantly. We could determine the value of the exponent related to shear rate by calculating the slope of the range of data where we have an increase of the concentration, finding $n = 7.15$. This value is significantly larger than that seen for graphene in previous studies ($n_{\text{gra}} = 1.13$) this is probably due to several reasons such as the different medium used (NMP for graphene, water and surfactant for WS₂), different standard volume (1500 mL for graphene despite 300 mL for WS₂ dispersions) and different rotor speed range where the material scales up (1500-4500 RPM for graphene, 7000-9000 RPM for WS₂).^{20,30}

4.3.3 Initial concentration dependence

WS₂ initial concentration was changed after setting NaC standard concentration and shear rate. Similarly, as the initial concentration of WS₂ is increased the final concentration of WS₂ increases. The parameter χ was found fitting the curve with the allometric equation, $C = a \cdot C_i^\chi$ (**Fig.4.7 C**), finding $\chi = 1$. This value agrees with the value found for graphene.^{20,30}

4.3.4 Volume study

Four different types of beakers were used for the volume study (600 ml; 1 l, 2 l, and 5 l) in order to study as wide a range of volumes as possible. This is described in **table 4.3**. As previously mentioned, it is crucial to estimate the degree to which WS₂ exfoliation can be scaled up, and for commercial production, the most important parameter is the production rate P_R . Looking at the equation (4.1), we notice it is necessary to use large volumes and a short period of time to maximise P_R . For this reason, the analysis of these two factors is significant. In this case, the volume study shows how concentration decreases when volume increases (**fig. 4.7 D**) finding the slope value $v = -0.84$.³⁰ This value does not correspond to the one found for graphene which is -0.69 .²⁰ This means that the WS₂ is more affected by the volume change than the graphene.

Table 4.3. Beakers used for different amount of dispersion prepared.

Beaker Capacitance	Liquid Volume (L)
600 mL	0.3
-	0.4
1 L	0.75
2 L	1.75
5 L	2.5
-	3.25
-	4

4.3.5 Time dependence

The last parameter studied is the mixing time, t . This study revealed that the WS_2 concentration increases with time according to a power law, and the exponent was found to be $\tau = 0.55$ (**fig.4.7 E**),³⁰ slightly lower than the exponent seen for graphene ($t_{\text{Gra}} = 0.66$).²⁰ These parameters mean the overall equation shows that the final dispersion concentration scales as:³⁰

$$C \propto C_i^1 N^{7.15} V^{-0.84} t^{0.55} \quad (4.7)$$

Plotting all concentration values obtained previously as a function of this equation we obtained a linear trend (**fig.4.7 F**) with a slope value equal to 1 which demonstrates that the concentration of WS_2 nanosheets is directly proportional to the scaling equation revealing a linear relationship between the two.

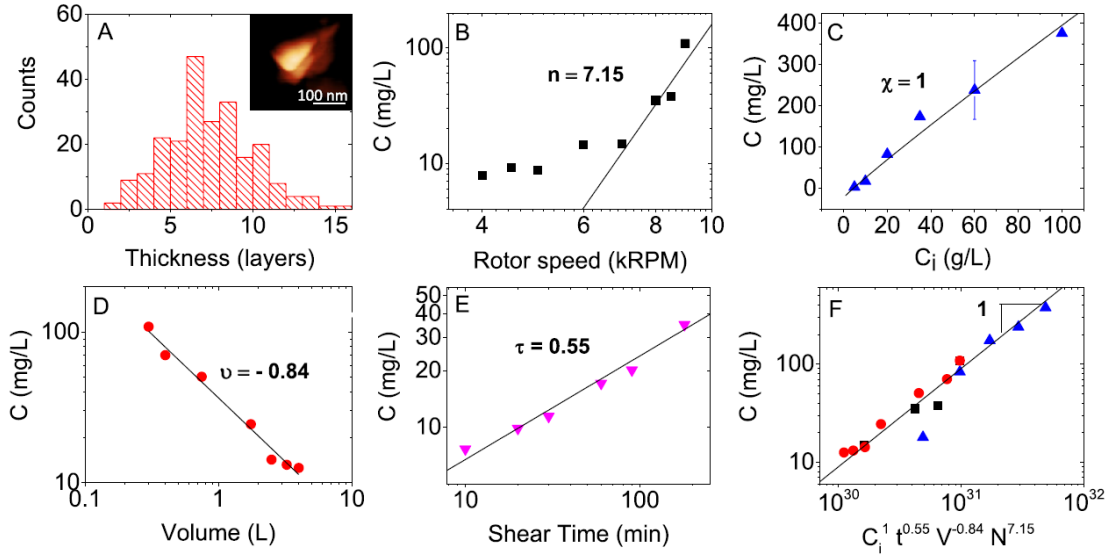


Fig.4.7. Graphs of AFM nanosheet thickness histogram ($\langle N \rangle \approx 6$) and representative image of WS_2 nanosheet obtained from standard sample (A); WS_2 concentration as a function of shear rate (B), initial concentration of WS_2 (C), volume (D), shear time (E) and as a function of the scaling equation (F) determined by the processing parameters.³⁰

Thanks to previous metrics,⁴⁸ thickness of nanosheets as a function of different processing parameters were calculated (eq.4.6, **fig.4.8**) showing, as shown in previous work with graphene shear exfoliation,²⁰ an increase of nanoparticle thickness as the dispersion volume increases (**fig.4.8D**) and a thickness reduction as the shear rate (fig.4.8A), the initial concentration (**fig.4.8B**), and the shear time (**fig.4.8C**) grow.

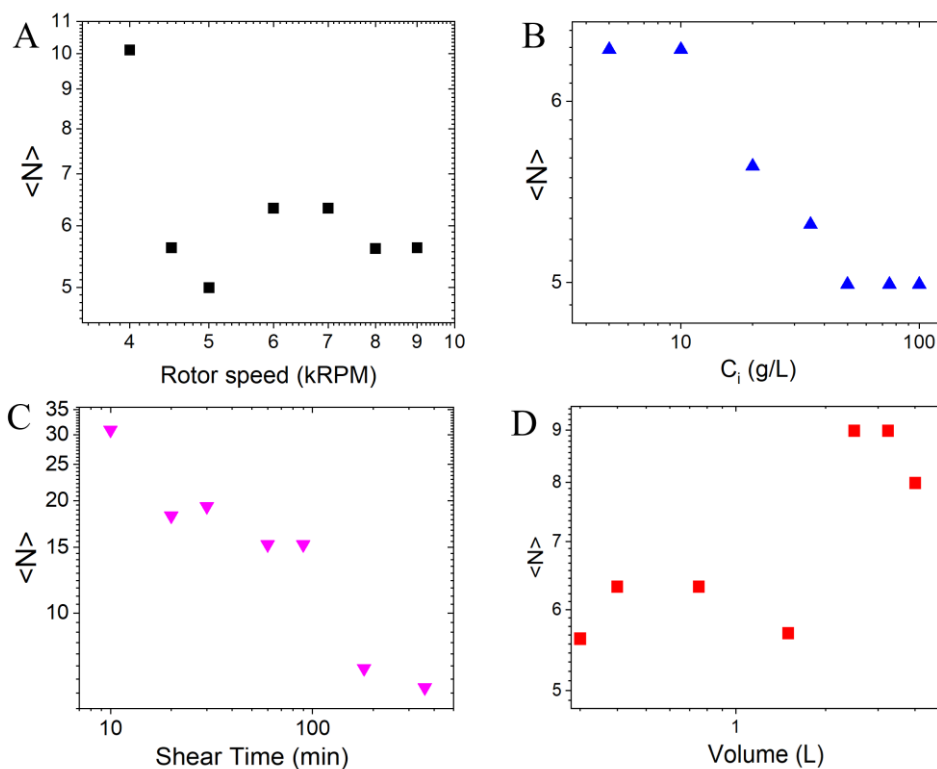


Fig.4.8. WS₂ nanosheets' thickness as a function of shear rate (A), initial WS₂ concentration (B), shear time (C), and dispersion volume (D).

Using the same work's metric,⁴⁸ it was also possible to use eq. 4.5 to obtain the length of the nanosheets as a function of different processing parameters (**fig.4.9**). From the graphs below, we can first observe that WS₂ nanosheets' size covers a range from 100-200 nm. In particular, we can see that in the case of shear rate study (**fig.4.9 A**), the WS₂ length varies from 110 to 150 nm. The lengths' trend, in this case, is not well defined, probably due to a combination of factors; firstly, this parameter might affect less the nanosheets length and secondly, the size selection procedure covers a large centrifugation speed range (2k-10k) resulting in a broad distribution of nanosheets dimension which affects the peaks shift of the UV-vis spectra and, consequently, the length values. We can also notice that the graph displaying the nanosheets' length as a function of WS₂ initial concentration (**fig.4.9 B**) shows a length decrease as the concentration of WS₂ raises with length values range between ~140 and ~110 nm. Finally, observing the graphs of the nanosheets' length as a function of the shear time (**fig.4.9 C**) and the volume (**fig.4.9 D**), we can see that these are the processing parameters which affect the nanosheets' size trend

the most. As expected, there is a decrease in length as the shearing time grows (going from ~200 to ~145 nm) and larger particles as the volume increases (with a length range of 120-160 nm).

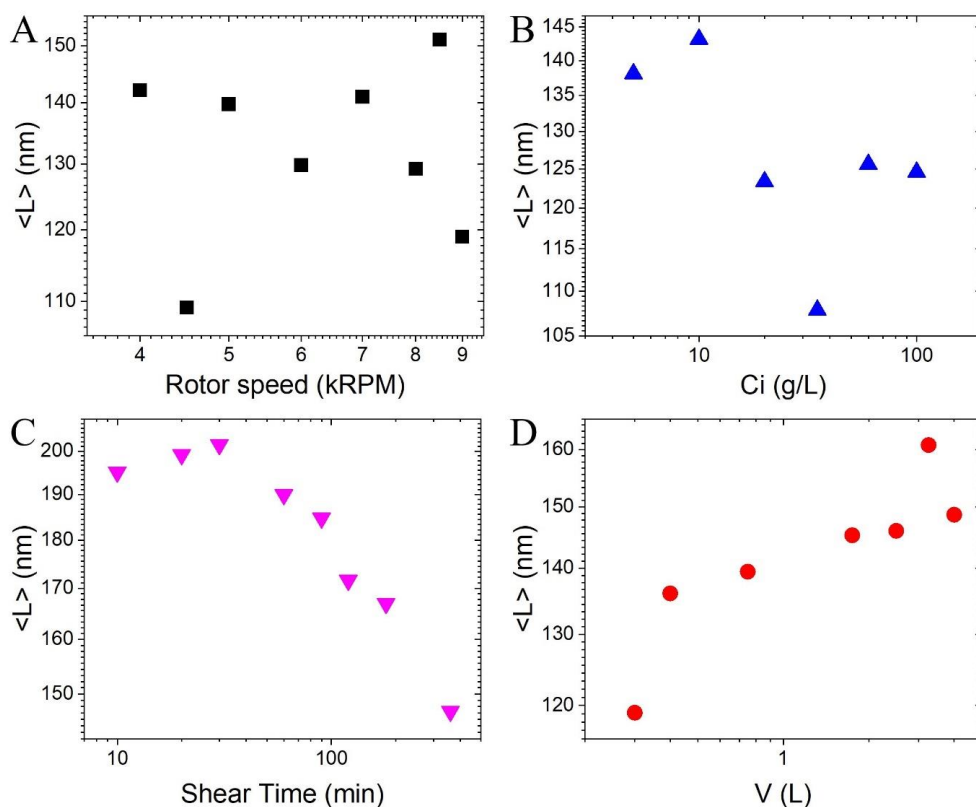


Fig.4.9. WS₂ nanosheets' length as a function of shear rate (A), initial WS₂ concentration (B), shear time (C), and dispersion volume (D).

Through variation of key parameters, it has been demonstrated that shear exfoliation is a suitable method to produce large quantities of exfoliated WS₂. After we determined the scaling parameters and demonstrating that shear exfoliation is a suitable method to produce large amounts of exfoliated WS₂, these parameters have been utilised to obtain two maximised cases: high concentration, reaching 1.82 g/L in 6 h (**fig.4.10A**) and material production rate reaching a value of 0.95 g h⁻¹ after 10 minutes (**fig.4.10B**).³⁰

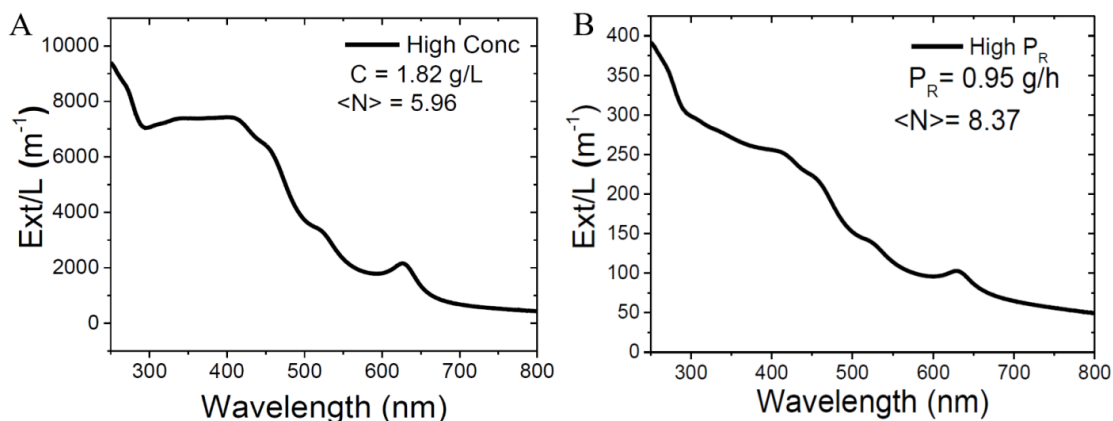


Fig.4.10. *UV-vis spectrum of WS₂ at high concentration (A) and at high production rate (B).*³⁰

We finalized our work by introducing the value of the high concentration in the plot of WS₂ nanosheets concentration *versus* scaling equation (**fig.4.11**) finding the high concentration value consistent with the data and the linear relationship previously obtained.

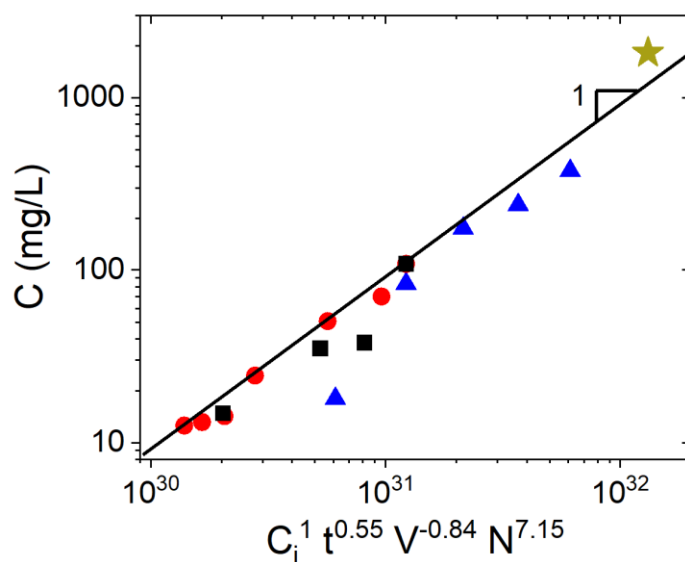


Fig.4.11. *Plot of WS₂ concentration versus scaling equation determined by processing parameters, including the high concentration value (represented by the star on the top right).*

Albeit it was possible to use the WS₂ for the preparation of PEO composites (described in **chapter 5**), unfortunately, the scaling parameters for other nanoparticles such as WSe₂ and MoSe₂ in water and cholate are unknown. For this reason, all nanoparticles used to fabricate PEO composites were prepared via ultrasonication in order to keep the preparation method constant for all the materials. However, preliminary studies were performed on PEO composites containing WS₂ prepared via shear exfoliation and WS₂ prepared using the sonic tip (selecting large nanoparticles in both cases), finding absolutely no difference between the two nanocomposites in terms of quality nor quantity results.

4.4 CONCLUSIONS

In this work, it was possible to demonstrate how to produce large quantities of defect-free WS₂ nanosheets.³⁰ This was achieved using high shear mixing, a widely accessible and versatile technology, already used to exfoliate a broad range of materials (from graphene to clay).^{200,204–207,366–368} Using empirical metrics obtained by simple optical analysis,⁴⁸ concentration, size and thickness of WS₂ nanosheets have been calculated.³⁰ Thanks to this information, an equation that relates the final concentration of nanosheets produced with different processing parameters was calculated. In this way, it was possible to show that shear mixing exfoliation of WS₂ leads to an equation which follows a power-law dependency demonstrating the scalability of WS₂ exfoliation in water and surfactant. By changing the surfactant concentration, it was found a peak with a maximum at 1.2 g/L of surfactant, maximising the concentration of WS₂ for the study. Furthermore, after the study of each processing parameter was performed, it was possible to understand how WS₂ nanosheets concentration changes as these parameters increase; showing that WS₂ raises with shear rate, shear time and initial concentration, and decreases with volume increase. It was also observed the dependency of WS₂ nanosheets thickness, finding that, as expected, it decreases with shear time, shear rate and initial concentration increase. It was possible to calculate the nanosheets size finding an overall length range between ~110-200 nm as the different processing parameters were varied. In particular, we observed a size decrease as the initial concentration of WS₂ and the shear time increases and a length rise directly proportional to the dispersion volume. Finally, the concentration values of WS₂ nanosheets was

maximised reaching a final concentration of 1.82 g/L finding this data matching with the scaling data. A production rate of 0.95 g/h was obtained which is one of the highest values obtained for WS₂ in water and surfactant,³⁰ showing the shear mixer as a valid scalable alternative to easily produce not just graphene, BN and MoS₂^{20,206} but, also defect-free (i.e. no chemical modification) WS₂ nanosheets.

Negative gauge factor piezoresistive nanocomposites

5.1 INTRODUCTION

With the development of sensor technology, the functionality of strain sensors has found use in the environmental monitoring of pressure and vibrations and also in biomonitoring through wearable sensors.^{58,137,329,369,370} To achieve high sensitivities and new functionalities, nanocomposites have recently been investigated as strain sensors.^{58,85,314,315} Nanocomposites exploit the combined properties of both filler and matrix.²²⁵ A strain sensor is a material that changes its resistance when a strain is applied and, commonly, the resistance increases during the tensile deformation.^{114,371–376} To verify the performance of a sensor, the important parameters to determine are the conductivity and gauge factor, or strain gauge (G).⁸² As previously mentioned (**chapter 2.2.6, eq. 1.1a**), the strain gauge is related to the change of resistance ($\Delta R / R_0$) as a function of strain, ε :⁶⁸

$$\frac{\Delta R}{R_0} = G\varepsilon \quad (5.1)$$

The majority of works on strain sensor reports positive values of gauge factor in a tensile test.^{276,344,377–384} This happens because the tunnelling effect occurs between conducting particles and, when a material is stretched, this effect decreases causing an overall resistance growth.^{93,385} However, there exists a category of materials which shows a negative gauge factor as a tensile strain is applied.^{315,349,386,387} As mentioned before, these materials have rarely been studied and while just a few works report composites with this characteristic, other materials have an intrinsic

negative gauge factor (usually n-type materials).^{65,387} This behaviour can be associated with the band-gap change of the material; an example is MoS₂ whose can be changed under strain, implying a negative gauge factor.^{58,90,156,360}

In this work, we used the typical band-gap change of MoS₂ in order to fabricate dynamic strain sensors. These sensors were prepared inserting TMD nanosheets in polyethylene oxide, the electromechanical properties are studied, and a model which describes the electrical and mechanical behaviour of the system is computed.⁵⁹

The nanosheets were prepared via ultrasonication of bulk powder in water and sodium cholate. The nanosheets were then size-selected and analysed via UV-vis spectroscopy, AFM, and TEM (**section 5.3.1**). Afterwards, they were inserted in PEO and the films were subjected to Raman and SEM analysis (**section 5.3.2**) and electromechanical tests (**section 5.3.3**).⁵⁹

5.2 PROCEDURE

5.2.1 Nanomaterial preparation

MoS₂, WS₂, MoSe₂, WSe₂, and graphene nanoparticles were prepared via liquid phase exfoliation. TMDs and graphene powders were subjected to a pre-treatment stage where the powder, with a concentration of 20 g/L, was immersed in water and sonicated for 1 hour and centrifuged for 2 hours at high speed (6000 rpm) to remove impurities. The supernatant was discarded and the sediment re-dispersed in 2 g/L sodium cholate aqueous solution and sonicated for 330 minutes. In order to avoid overheating and, consequently, possible undesired reactions (i.e. oxidation or other chemical modification of the nanoparticles), the dispersions were kept in a cooling system during both sonication steps. Afterwards, selections of large nanosheets were obtained by centrifuging the supernatant at low speed (1000 rpm) and were then ready to be characterized.⁵⁹

5.2.2 Film preparation

Different ratios of polymer-nanosheets composite films were been prepared (reported in graphs as mass fractions, M_f , or volume fractions, ϕ). Specific volumes of nanosheet dispersions were mixed with PEO/H₂O solutions. A total volume of 15 mL was kept constant by adding water to the mixture. After that, the dispersion nanosheet-polymer was poured into a Petri dish and dried overnight at 50 °C. The films obtained looked macroscopically uniform and were then analysed (**fig.5.1**).⁵⁹

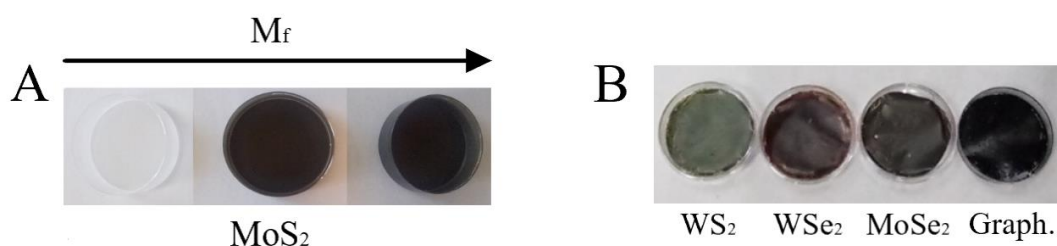


Fig.5.1. *Nanocomposite films containing different MoS₂'s loading level (a) and different types of fillers (b).*⁵⁹

5.2.2 Electromechanical testing

Composite films were cut obtaining uniform strips with a width of 2.25 mm and a thickness of 72 μ m for each strip. The strips were attached to the clamps of the tensile tester at a distance of 9.73 mm apart. These clamps were also connected to a source meter and electrical measurements were recorded using a LabView program. For all samples made, the resistance was recorded at zero-strain before measuring the tensile strain and the conductivity was calculated from these data.

Afterwards, the samples were strained (10 mm/min speed test) and both stress and resistance of the samples were recorded. From the stress-strain curves, it was possible to evaluate Young's moduli using TestXpert software. Using R- ϵ curves, it was possible to extrapolate G values by determining the slope of the $\Delta R/R_0$ versus strain graph.

In order to perform cyclic tests, a sine wave simulation program was used on 0.5 wt.-% PEO/MoS₂ films obtaining a dynamic strain profile for 3 different frequencies (0.1, 0.5 and 1 Hz). A minimum number of 7 tests per sample was

performed, computing the average and standard deviation through Origin software.⁵⁹

5.2.3 *In-situ* Raman deformation test

In this case, Raman tests were sent to Manchester University and there, the sample was prepared by drop-casting MoS₂/PEO mixture solution with a mass fraction of MoS₂ = 0.5 wt.-% onto a PMMA beam and left to dry. The PMMA beams were UV treated prior deposition to improve adhesion between the sample and the beam itself. After that, the sample was placed on the microscope stage of the Raman spectrometer (LabRAM HR Evolution, Horiba) equipped with a laser with $\lambda = 488$ nm. Using a four-point bending rig, the sample was deformed and the strain was measured using a strain gauge next to the film.^{59,356}

5.3 RESULTS

5.3.1 Nanosheets production and analysis

After the centrifugation steps, optical spectra were obtained from the size selected dispersions (**fig.5.2 A** and **fig.5.3 E-H**). As expected, in **figure 5.2 A** we observe the presence of a long “tail” in the extinction spectrum (black line).⁵⁹ This is due to the scattering effect that occurs in large nanoparticle UV-vis analyses (red line). In order to remove the contribution of scattering in the extinction spectrum, an integrating sphere was used.^{59,354} In this way, it was possible to obtain a pure absorption spectrum (blue line) which has the distinctive MoS₂ shape with the typical A-peaks around 670 nm.^{19,20,48} Thanks to these analyses it was possible to calculate, through previously published metrics, concentration, length and thickness of the nanoparticles.⁴⁸ Using both the position of the excitonic A-peak and the shape of the spectra, we estimated a nanoparticle length of ~240 nm and a thickness of around 6 nm for MoS₂ nanoparticles.⁵⁹

These data have been confirmed by TEM (**fig.5.2 B, E**) and AFM (**fig.5.2 C, F**) analyses. The TEM statistical analysis was performed on the sample with 200

counts, finding a length distribution from 50 to 700 nm with a mean of 240 nm. AFM analyses were performed drop-casting on Si/SiO₂ wafers and the statistical analysis shows a distribution similar to the TEM analysis. The calculation of the thickness (**fig.5.2. F inset**) shows a distribution with a mean at 5.5 nm.⁵⁹ From this analysis, we see that over 77% of the nanosheets were thicker than four layers. This implies thickness-independent bandgaps in the nanosheets and also a similar nanosheet conductivity.⁵⁹

To verify the quality of the material, Raman analysis ($\lambda = 532$ nm) was performed on a filtered MoS₂ nanosheets film (**fig.5.2 D**). From the spectrum, it is possible to see the typical Raman shifts of (2H) semiconducting MoS₂ at 380 (E_{2g}^1) and 405 (A_{1g}) cm^{-1} .³⁸⁸

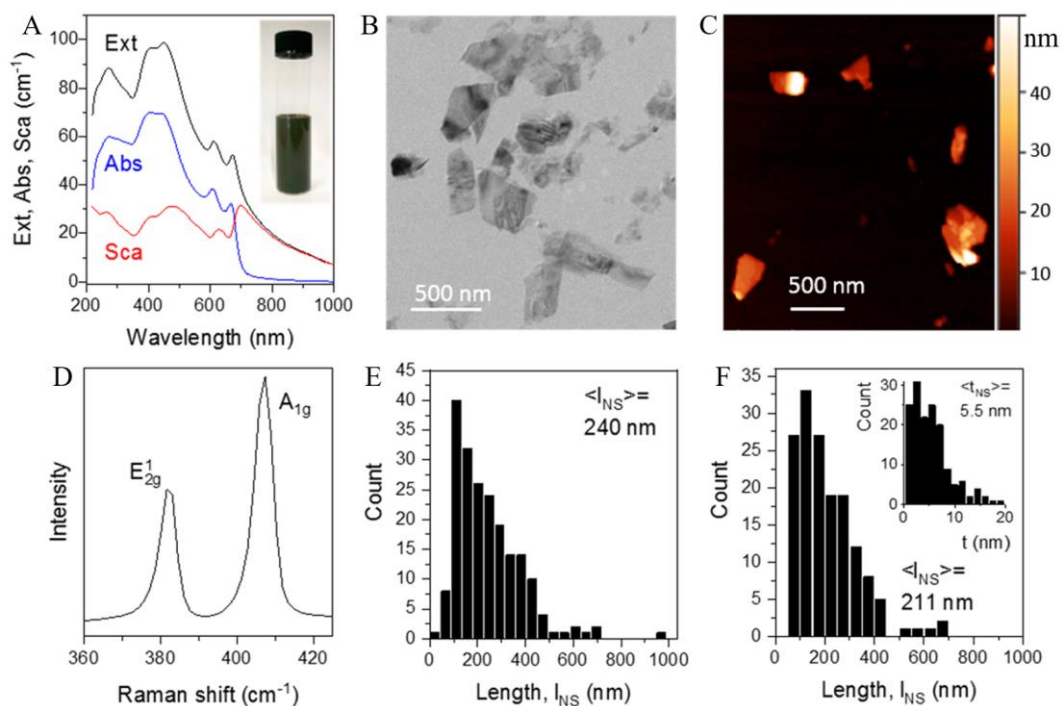


Fig.5.2. Characterizations of MoS₂ dispersion (A inset picture). UV-vis analysis showing the extinction (black), absorption (blue) and scattering (red) spectra (A). TEM image (B) and of the nanosheets. Representative AFM image of MoS₂ deposited on Si/SiO₂ wafer (C). Raman spectrum measured on a nanosheet film (D). Nanosheets length histogram measured from TEM images (E). Nanosheet length and thickness (inset) histogram obtained by AFM images (F).⁵⁹

WS₂, WSe₂, MoSe₂ and graphene nanosheets dispersions were prepared using the same sonication and centrifugation procedure adopted to prepare MoS₂ dispersion previously described. From UV-vis analysis (**fig.5.3 E-H**) it was possible to obtain the extinction spectra of the nanosheets (black line) and with the integrated sphere the scattering (blue line) typical of large nanosheets was subtracted and the pure absorption spectra found (red line).³⁸⁹ Here, a previous metric was also used to obtain concentration, length, and thickness of the nanosheets.^{48,320} TEM analysis of the nanosheets dispersions was performed and the length of the nanosheets was found (**fig.5.3 A-D**). The statistical distribution of the nanosheets shows a length of 200 nm for all the nanosheets with the sole exception of the WSe₂ which presented with a mean length of ~77 nm.⁵⁹

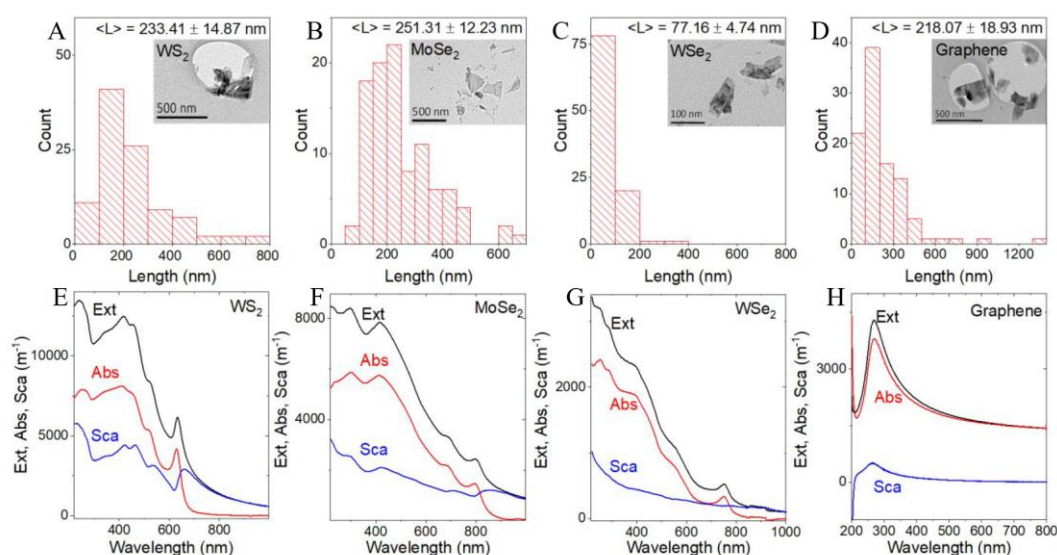


Fig.5.3. TEM representative images and histograms of WS₂ (A), MoSe₂ (B), WSe₂ (C) and graphene (D) nanosheets. The bottom row shows nanosheets' comparison of absorption (red), extinction (black) and scattering (blue) spectra of WS₂ (E), MoSe₂ (F), WSe₂ (G) and graphene (H).⁵⁹

5.3.2 Composite basic characterization

After blending the dispersion with the polymer and obtaining uniform films, qualitative Raman analyses were performed on the PEO film (**fig.5.4 top**), on the MoS₂ film (**fig.5.4 bottom**) and on the composite with different wt.-% of MoS₂.

Here, the Raman spectra of the composites show the typical peaks of both MoS₂ and PEO (**fig.5.4 inset**) demonstrating the presence of MoS₂ nanosheets blended with the PEO matrix.

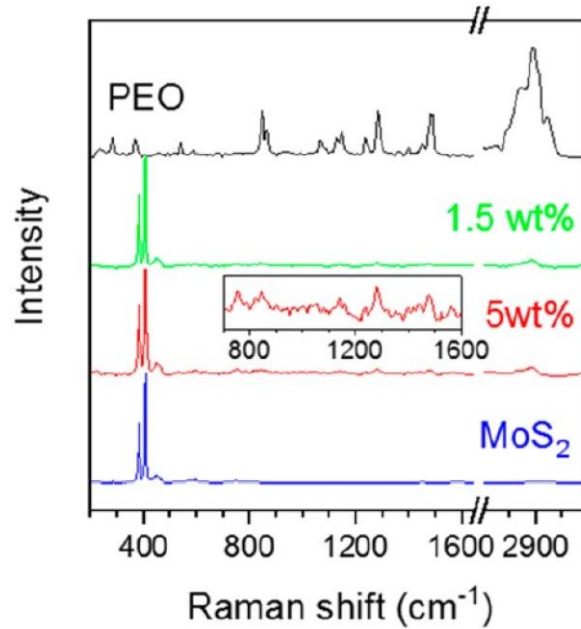


Fig.5.4. Raman spectra measured on a PEO film (black) and MoS₂/PEO composite films with $M_f = 1.5$ (green) and 5 (red) wt.-%. The spectrum associated with a MoS₂-only film is also shown (blue). The inset displays PEO modes are also observed in the composite films.

Mechanical analyses were performed by measuring tensile stress-strain curves for each mass fraction of MoS₂/PEO composites (**fig.5.5**). A ductile behaviour was observed for all the mass fraction composites showing strains above 100%.⁵⁹

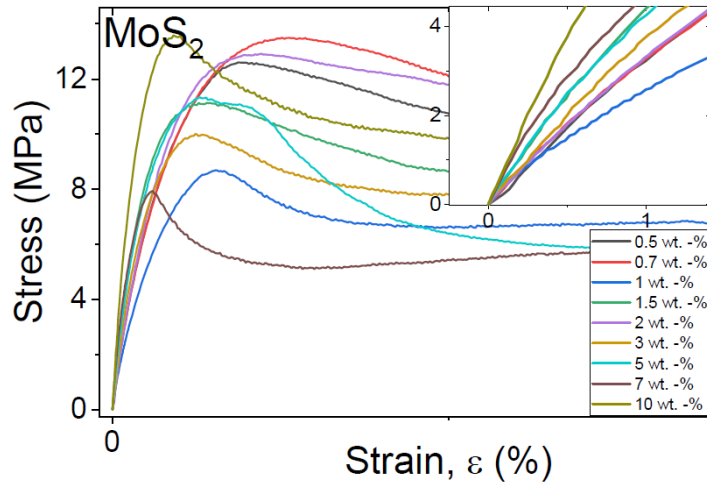


Fig.5.5. Stress-strain curves of different MoS_2 mass fractions.⁵⁹

Representative stress-strain curves (**fig.5.6 A**) show how the presence of MoS_2 stiffens the polymer. This analysis can be done quantitatively by measuring Young's modulus from stress-strain curves. In **figure 5.6 B**, the average of Young's modulus of each sample has been plotted versus the volume fraction, ϕ , (with also the corresponding mass fraction, M_f). It is clear from this graph that reinforcement occurs as the MoS_2 is added to the polymer with Young's modulus ranging from 270 MPa for the PEO itself to 570 MPa for 0.5 vol. % (2 wt.-%).⁵⁹ At higher loading levels, Young's modulus saturates and this saturation is generally attributed to an aggregation effect.⁵⁹ Furthermore, it is possible to notice that the ultimate tensile strength does not change significantly, oscillating from 10 to 15 MPa, while the yield strain decreases considerably going from ~10 % to ~4 %, as the amount of MoS_2 increases.⁵⁹

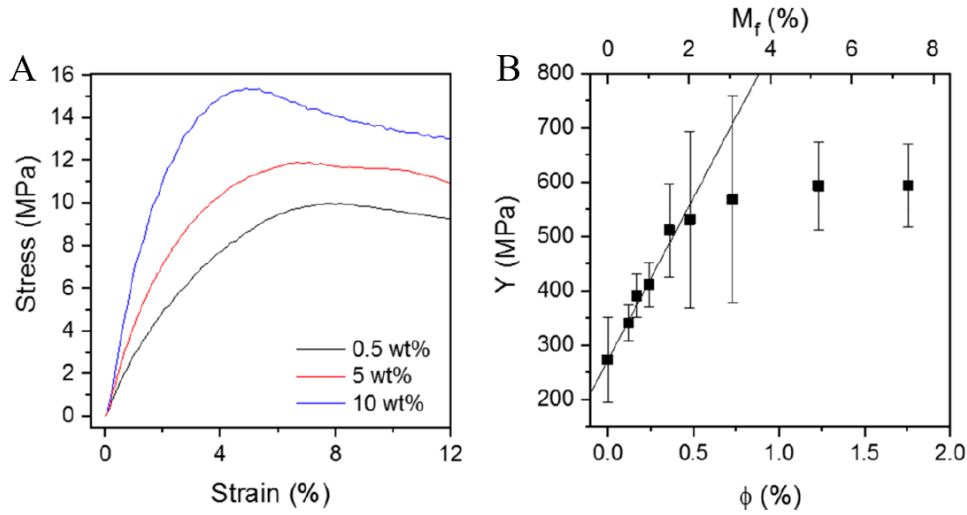


Fig.5.6. Representative stress-strain curves for selected MoS₂/PEO composites (A) and Young's modulus plotted versus MoS₂ volume fraction for MoS₂/PEO composites.⁵⁹

The modulus increase was quantitatively analysed using the rule of mixtures. As mentioned in **chapter 2.4.4**, this model predicts the composite modulus, Y_C , to increase with filler volume, ϕ , fraction as³¹⁷

$$Y_C = \eta_l \eta_0 Y_f \Phi_f + Y_m (1 - \Phi_f) \quad (5.2)$$

where Y_f and Y_m are the moduli of the filler and the polymer matrix, respectively, while η_l and η_0 are efficiency factors associated with filler length and orientation, respectively.³¹² As we can see from **figure 5.6 B**, this model matches the data very well up to $\phi \approx 0.5$ % after which the modulus diverges from theory. This is a common behaviour of nanocomposites and, as mentioned above, is due to aggregation effects.

As previously mentioned (**section 2.4.4**), it is possible to calculate the efficiency factor using the general equation (**eq. 2.28**):

$$\eta = \frac{Y_f / Y_m - 1}{Y_f / Y_m + 2l_f / t_f} \quad (2.28)$$

where Y_f and Y_m are respectively, the Young's moduli of filler and matrix used in the composite and l_f and t_f are length and thickness of filler nanoparticles.

For composite where the ratio Y_f/Y_m is $\gg 1$ the expression above can be rewritten:

$$\eta \approx \left[1 + 2 \frac{l_f / t_f}{Y_f / Y_m} \right]^{-1} \quad (5.3)$$

Observing this equation, we can first notice that η can assume values $0 \leq \eta \leq 1$. Then, due to the fact that in most of the nanocomposite there is a very low concentration of nanofiller, we can make the approximation $\phi \ll 1$. So we can combine these two expressions and find:

$$Y_C \approx Y_m + \frac{Y_f \phi}{\left[\frac{Y_f / Y_m}{2l_f / t_f} + 1 \right]} \quad (5.4)$$

By comparison with the rule of mixture and, disregarding the orientation effects, we can combine $Y_C = \eta_l Y_f \Phi_f + Y_m (1 - \Phi_f)$ with equation 5.4 finding the efficiency factor, η_l :

$$\eta_l \approx \left[\frac{Y_f / Y_m}{2l_f / t_f} + 1 \right]^{-1} \quad (5.5)$$

This equation is very accurate at low nanoparticles volume fraction. Substituting the values $Y_f = 270$ GPa,³⁶⁰ $Y_m = 270$ MPa (from **fig.5.6 B**), $l_f/t_f = 55$ (from **fig.5.2**) we can calculate the value of the efficiency factor, finding $\eta_1 \approx 0.1$.

From the experimental data, the linear fit gives $\eta_0 \eta_1 Y_f = 60$ GPa and, using a value for randomly oriented distributions of platelets $\eta_0 = 8/15$,^{314,390} plus combining the equation with the known value of $Y_f = 270$ GPa,³⁹¹ we obtain $\eta_1 = 0.4$. This value is significantly larger than the calculated value ($\eta_1 < 0.1$),³⁵⁶ which implies a better reinforcement than expected. These relatively high levels of reinforcement indicate that stress is transferred effectively across the PEO/MoS₂ interface which implies that the MoS₂ nanosheets come under strain as the polymer is stretched.⁵⁹ This might be explained by a process called boost reinforcement, which involves the crystallization of PEO at the MoS₂ surface as PEO is already known to crystallize on graphene surfaces.³⁹² In fact, the incorporation of inorganic fillers in semi-crystalline polymers can affect the crystallization behaviour acting like nucleation agents.^{252,393} This causes an acceleration of the crystallization process, influencing the interface between filler and matrix and the mechanical properties of the composites.³⁹³

Conductivity analyses were performed on the samples, revealing an increment of the conductivity with the volume fraction, ϕ (**fig.5.7**). We found the conductivity to increase from $\sim 10^{-6}$ S/m to $\sim 2 \cdot 10^{-5}$ S/m for the $\phi = 1.75\%$ sample.³²⁰ Interestingly, these values are significantly higher than the typical MoS₂'s conductivity values reported ($\sim 10^{-6}$ S/m).²⁸ This is very surprising as we would expect a conductivity decrease with polymer implementation compared to neat nanosheet networks. We further investigated conductivity behaviour by fitting the curve with the percolation theory equation described in **chapter 2.4.5**.³²¹

$$\sigma = \sigma_0 (\Phi - \Phi_c)^n \quad (5.6)$$

As stated, the conductivity of the composite, σ , is related to the filler conductivity, σ_0 , the volume fraction, Φ , the percolation threshold, Φ_c , and the percolation exponent, n . The fit leads to $\Phi_c = 10^{-3}$, $n = 1.1$, and $\sigma_0 = 1.73$ mS/m.⁵⁹ For randomly

arranged 2D fillers, percolation thresholds are typically $\Phi_c \sim t_{NS}/l_{NS}$ (thickness/length), which implies $\Phi_c \sim 0.02$. The experimental percolation threshold value is significantly below this prediction, possibly due to a phenomenon called kinetic percolation.^{321,322,339} In fact, the kinetic percolation implies a decrease or increase of the percolation threshold caused by experimental and/or chemical processes (i.e. shearing of conducting particles caused by experimental procedures, thermodynamic or mechanical instabilities during a chemical reaction in homogeneous systems).^{323,325,326,394-397} Moreover, the exponent is slightly lower than the value of 1.3 expected for percolation in two dimensions (i.e., a thin film), although reduced n-values often accompany low percolation thresholds.^{339,356} What is most unusual about the electrical data is the relatively high value of the filler conductivity which, for networks of MoS₂ nanosheets are typically found to be $\sim 10^{-6} - 10^{-5} \text{ S}\cdot\text{m}^{-1}$,^{28,398} is considerably lower than the value we found.⁵⁹

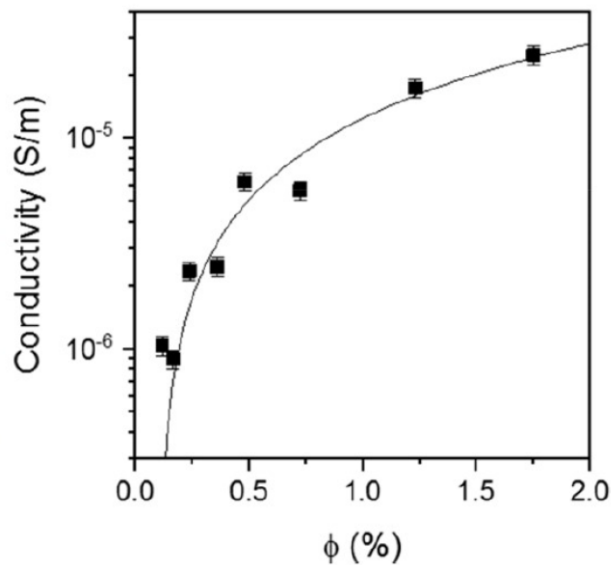


Fig.5.7. Conductivity plotted versus MoS₂ volume fraction for MoS₂/PEO composites. The line is fitting the percolation theory.⁵⁹

To explain these findings, we hypothesized that the PEO has a doping effect on the nanofillers.⁵⁹

To test this, we first performed a conductivity analysis on a MoS₂-only network deposited on an electrode array finding, for both samples, $\sigma_0 = 3 \cdot 10^{-5}$ S/m. After this, 1 μ L droplet of PEO/H₂O solution was dropped onto the MoS₂ network, allowed to dry, and the conductivity measured with the process repeated twice for both samples (**Fig. 5.8 A**).⁵⁹ This led to interesting results, where the MoS₂ conductivity increases 10 times as the PEO is added to the network, which confirms the doping effect of PEO which is associated to a charge transfer mechanism (**fig.5.8 B**), as it is often found in different polymer/MoS₂ systems.^{59,399}

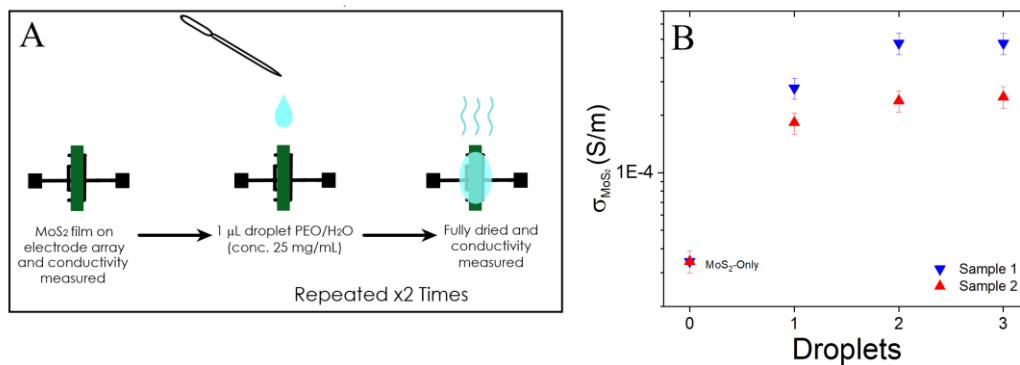


Fig.5.8. The procedure adopted in order to verify the doping effects of PEO on MoS₂ (A). The conductivity of a MoS₂-only network before (0 droplets) and after depositing 1, 2, and 3 droplets of PEO dissolved in water (B).⁵⁹

SEM analyses were also performed on the samples at 2 kV at different MoS₂ loading levels. In **figure 5.9**, the cross-section (**A-D**) and the surface (**E-H**) of PEO/MoS₂ composite films are shown. From these images, we can observe the presence of MoS₂ flakes embedded with the polymer (**fig.5.9 A-D**) demonstrating the presence of MoS₂ flakes not just on the composite surface. Moreover, we can see how the increase of MoS₂ nanosheets affects also the composite topography (**fig.5.9 E-H**).

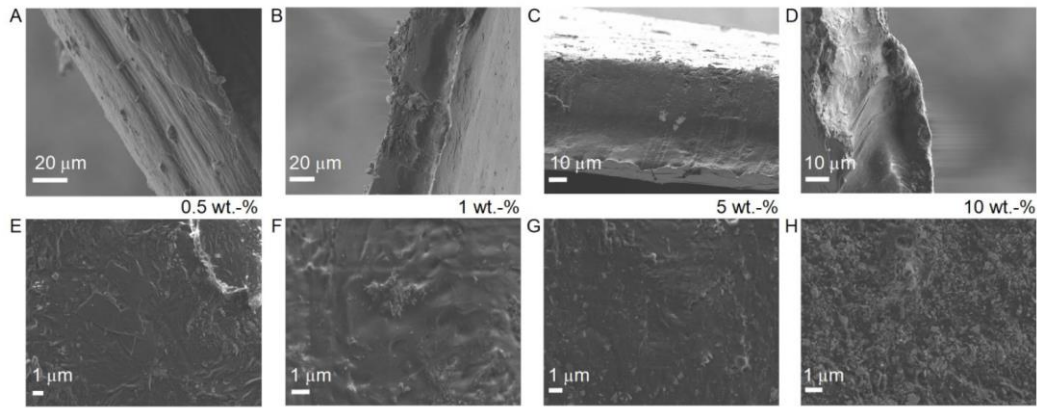


Fig.5.9. SEM images of composite PEO/MoS₂ films for different M_f . The top row displays the cross section while on the bottom row the surface of PEO/MoS₂ composite film at 0.5 (A, E), 1 (B, F), 5 (C, G) and 10 (D, H) wt.-%.⁵⁹

5.3.3 Electromechanical properties

The most interesting part about these composites is their electromechanical response. The typical plots of fractional resistance change, $\Delta R/R_0$, as a function of tensile strain, ϵ , for different mass fractions are shown in **figure 5.10 A**. As we can see from the graph, the resistance falls at low tensile strain and reaches a minimum before increasing at higher strains.⁵⁹ This behaviour was observed for all MoS₂ mass fraction samples tested. Such resistance reductions are exceptionally unusual for tensile tests, in which almost all nanocomposite electromechanical tests display monotonic resistance increase as a tensile strain is applied. The only non-monotonic behaviour we are aware of is a work from *Boland et al.*,¹³⁷ where a polysilicone/graphene composite shows a resistance increase followed by a subsequent decrease with increasing strain behaviour, associated to the extreme softness of the matrix. In terms of quantitative characterization, the gauge factor, G (the slope of $\Delta R/R_0$ vs ϵ) was calculated for each sample and the mean value was plotted vs. MoS₂ volume fraction (**Fig.5.10 B**). The mean gauge factors measured for MoS₂/PEO composites, in the limit of low strain, are all negative and they range between -12 and -25 with a peak at intermediate loading.⁵⁹

In order to understand this peculiar behaviour, we first observe that the strain associated with the resistance minimum coincides with the yield strain (strain at maximum stress) as measured in the tensile mechanical tests (**fig.5.10 C**). In **figure**

5.10 D we can see that this correlation holds over all samples. This implies that the negative gauge factor is associated with the elastic region of the stress-strain curve while plastic deformation at higher strains results in large resistance increases.⁵⁹ This leads to the hypothesis that, at low strains within the elastic region, enough stress is transferred to the MoS₂ nanosheets to stretch them, thus reducing the nanosheet resistance and causes the negative gauge factor effect. This hypothesis has its origin in the fact that the MoS₂ nanosheets themselves have a negative gauge factor.³⁶⁰

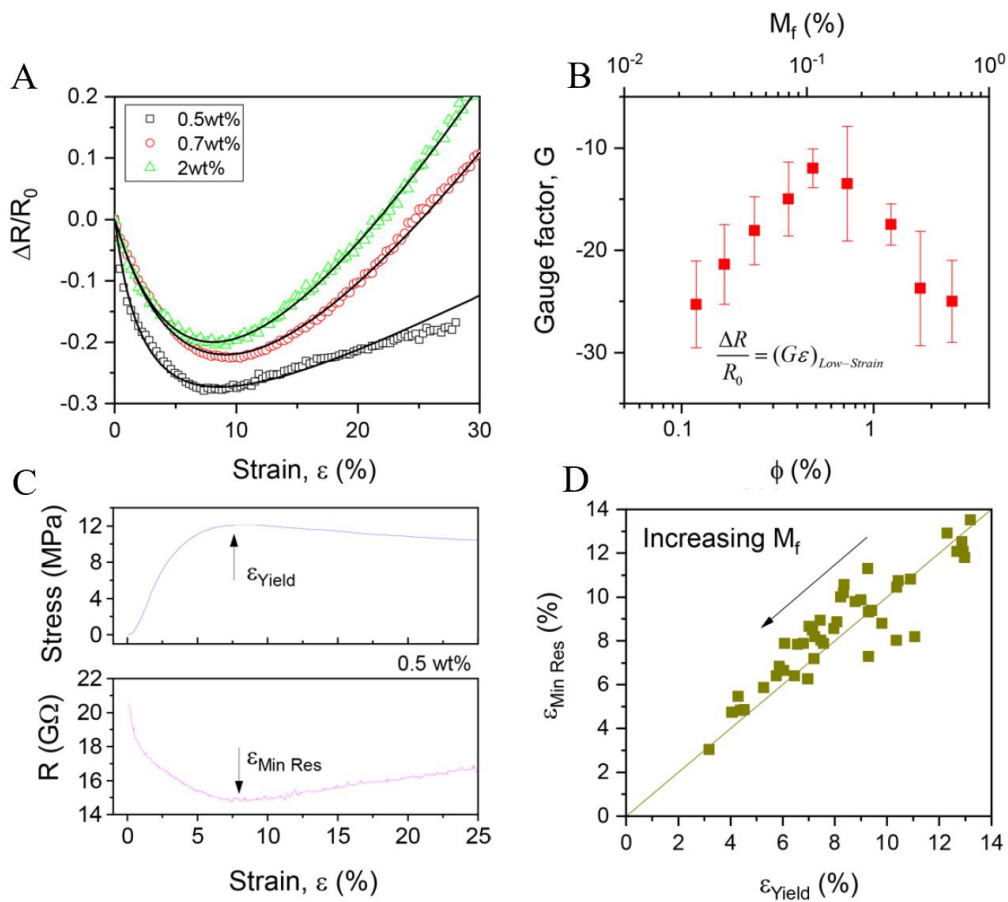


Fig.5.10. Representative curves showing fractional resistance change as a function of applied tensile strain (A). Gauge factor plotted as a function of the volume fraction, ϕ % (B). Typical stress-strain (top) and resistance-strain (bottom) curves measured for plotted MoS₂/PEO composites (here $M_f = 0.5\%$) (C). Strain associated with resistance minimum plotted versus the yield strain for all MoS₂/PEO composites (D).⁵⁹

For this hypothesis to be true, enough stress must be transferred from polymer to nanosheet to stretch the nanosheets, and in order to test this, we performed Raman spectroscopy as a function of strain applied to the composite. In **figure 5.11** we can see that both the E_{2g}^1 and A_{1g} bands downshift as MoS₂ nanosheets are stretched with the composites. The in-plane vibrational mode, E_{2g}^1 , with a wavenumber of $\sim 380\text{ cm}^{-1}$, has a shift rate of about $-0.7\text{ cm}^{-1}/\%$.⁵⁹ Although the absolute value is lower than the values reported in the literature,⁶⁸ they were from a more ‘ideal’ specimen where the nanosheets are not just larger and thinner but also aligned in the plane of strain (same as the direction of vibration). Observing the shift rate of the out-of-plane A_{1g} mode, we notice that it is $0.8\text{ cm}^{-1}/\%$. This is slightly lower than the values reported for few-layer nanosheets, most likely due to the fact that this shift mode is less sensitive to flake size.³⁵⁶

Another important observation to highlight is that the linearity between the Raman band positions and the strain only holds until $\sim 0.5\%$ strain.⁵⁹ After that, a lower stress transfer efficiency between the interfaces causes a flattening of the curve. This study confirms that strain can be transferred to the MoS₂ nanosheets, and this causes a negative composite gauge factor related to the nanosheets stretching.

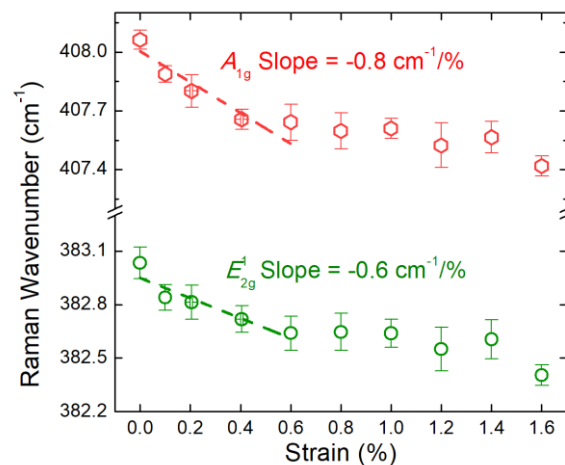


Fig.5.11. Raman band position of E_{2g}^1 and A_{1g} bands as the function of strain. The measurement is the average from seven measurements, and the error bars represent the standard error of the mean.⁵⁹

After comprehending the association between the negative gauge factor and the elastic deformation of the samples, dynamic tests were performed on the composites (**fig. 5.12**). In order to demonstrate that PEO/MoS₂ composites can be used as strain sensors, we applied sinusoidal strains varying the strain from 0.5 to 2%, and repeated the test at different frequencies (0.1, 0.5, and 1 Hz, **fig.5.12 A-C**). As expected, the resultant resistance shows in each case an out-of-phase harmonic response with the applied strain.⁵⁹ To demonstrate the consistency of the data, we calculated the Fourier transforms from the entire duration of the test Origin program (duration: 100 s for 0.1 Hz, 200 s for 0.5 Hz, and 50 s for 1 Hz). In all cases, a clear peak is observed on a 1/f background for 0.1 (**fig.5.12 D**), 0.5 (**fig.5.12 E**) and 1 (**fig.5.12 F**) Hz.⁵⁹

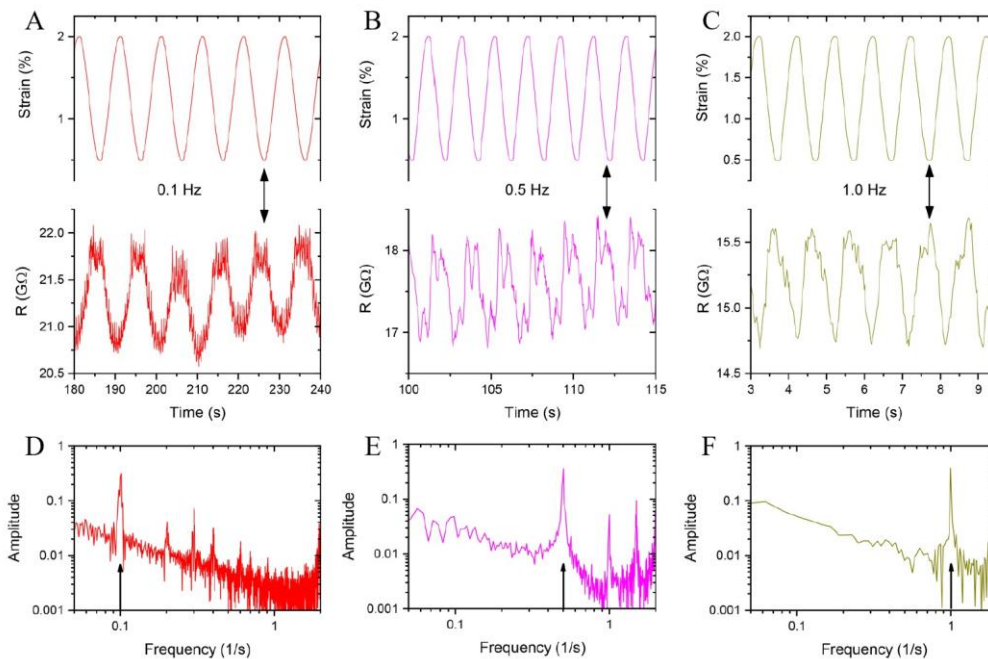


Fig.5.12. *Dynamic strain profiles with the resultant resistance response oscillating at three different frequencies: (A) 0.1 Hz, (B) 0.5 Hz, and (C) 1 Hz. Fourier transforms for the R-t curves in A-C (D-F). The arrows indicate the main peak with the other peaks representing harmonics.⁵⁹*

To check the stability of the resistance signal, step strain measurements were performed on the samples (**fig.5.13**). Composites with 5 wt.-% MoS₂/PEO have

been analysed performing step strains of 2.5% (**fig.5.13 A**) and 3% (**fig.5.13 B**) and the strain (**top row**), stress (**middle row**) and resistance (**bottom row**) response as a function of time are recorded. As we can see the resistance response is reasonably stable over time although changes start to occur after a few minutes due to possible water adsorption, which can cause, overtime, changes in electrical and mechanical properties.⁵⁹

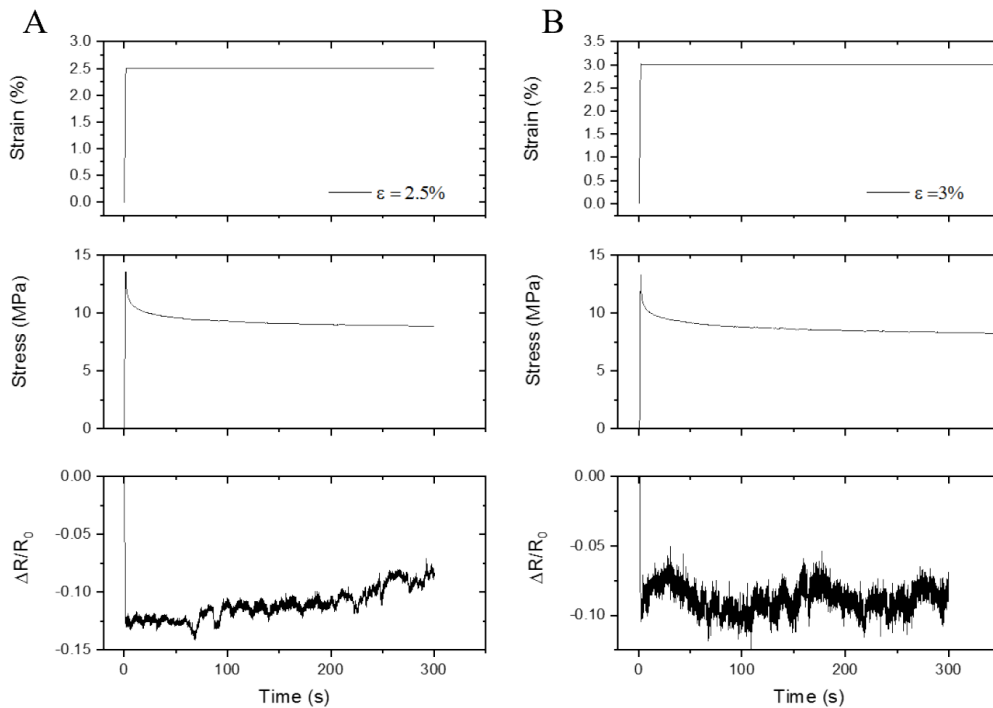


Fig.5.13. Response of 5wt.-% MoS₂/PEO composite to step strains of 2.5 (A) and 3% (B). Top row: applied strain. Middle row: stress. Bottom row: fractional resistance change.⁵⁹

5.3.4 Modelling composite piezoresistance

As the initial resistance decrease is followed by an increase at high strain, a physical model is needed to fully describe the system. Below we describe such a model.

As previously mentioned, in standard composite strain sensors, the composite piezoresistance is associated with inter-nanosheet tunnelling resistance effects.^{93,385} This occurs because the filler particles themselves have a relatively low resistance thus, the overall conductivity is limited by junction resistances. This implies that

any strain-induced resistance change would be caused by changes in inter-nanosheet tunnelling with strain. However, this circumstance does not occur in MoS₂/PEO composites because of the higher resistivity of the nanosheets themselves than conductive fillers, such as graphene nanosheets or carbon nanotubes.⁴⁰⁰ Thus, the composite resistance is limited by the nanosheet resistance rather than the inter-nanosheet junction resistance. The presence of this characteristic in the MoS₂/PEO system allows a change of the composite resistance as the strain-induced filler resistance varies (previously demonstrated from the Raman *in situ* deformation test).⁵⁹

Every time a charge carrier passes through a nanosheet, it must also cross an inter-nanosheet junction through a minimum number of nanosheets per conductive path. Thus, we assumed that the nanosheet network resistivity depends on four factors: the intrinsic nanosheet resistance, R_{NS} , the inter-nanosheet junction resistance, R_J , the network structure, χ , and the nanosheet dimensions, l_{NS} :¹³⁷

$$\rho = \frac{(R_{NS} + R_J) \cdot \chi}{l_{NS}} \quad (5.7)$$

In general, R_{NS} , R_J , and ρ all depend on applied strain. Because equation 5.6 describes the ϕ -dependence of the conductivity, equation 5.6 and equation 5.7 must be closely related thus, equation 5.7 should also display ϕ -dependence. Considering the fact that χ is a measure of the nanosheet network structure, we used the equation 5.6 to correlate χ with the percolation theory³²¹ finding $\chi \propto (\Phi - \Phi_c)^{-n}$.³²¹

It is also possible to represent an individual nanosheet modifying equation 5.1:

$$R_{NS}(\varepsilon) = R_{NS,0} \cdot G_{NS} \cdot \varepsilon + R_{NS,0} \quad (5.8)$$

where G_{NS} is the intrinsic gauge factor of the nanosheet and $R_{NS,0}$ is the resistance of the nanosheets at zero-strain. Assuming that the strain in the nanosheet is equal to the applied strain,³³⁹ we combined the previous equations and obtained:

$$\rho(\varepsilon) = \frac{[R_{NS,0}(G_{NS}\varepsilon + 1) + R_J(\varepsilon)]\chi}{l_{NS}} \quad (5.9)$$

In addition, for any incompressible material, $\Delta R / R_0$ as a function of the strain, with the Poisson ration, $\nu = 0.5$, can be described by the equation:¹³⁷

$$\frac{\Delta R}{R_0} = \left[\frac{1}{\rho_0} \frac{d\rho}{d\varepsilon} + 2 \right] \varepsilon \quad (5.10)$$

And combining equations 5.9 and 5.10 we obtained⁵⁹

$$\frac{\Delta R}{R_0} = \left[\frac{G_{NS} + (dR_J / d\varepsilon) / R_{NS,0}}{1 + R_{J,0} / R_{NS,0}} + 2 \right] \varepsilon \quad (5.11)$$

where $R_{J,0}$ is the zero-strain junction resistance. This is a general equation which describes the electromechanical response of a network. It is possible to estimate $dR_J/d\varepsilon$ using two pre-existing models, based on tunnelling⁴⁰⁰ and dynamic network connectivity.¹³⁷ However, the strain-dependence of conductivity/resistivity in composites includes several effects which contribute to this relationship such as tunnelling, network connectivity, as well as orientation effects. Considering the fact that this behaviour is complicated to describe, we decided to take an empirical approach in order to identify a function able to represent the R_J dependency on the strain. First of all, we prepared a PEO-graphene composite. In fact, this composite

exhibits a positive piezoresistance which enabled us to approximate $G_{NS} \sim 0$ finding:⁵⁹

$$\frac{\Delta R}{R_0} = \left[\frac{(dR_J / d\varepsilon) / R_{NS,0}}{1 + R_{J,0} / R_{NS,0}} + 2 \right] \varepsilon \quad (5.12)$$

We measured the strain-dependent resistance and, through trial and error, we found an empirical equation that described the strain-resistance behaviour:

$$\frac{dR_J}{d\varepsilon} = \frac{k\varepsilon}{\varepsilon_1 + \varepsilon} \quad (5.13)$$

where k and ε_1 are constants. If we use equation 5.13 we obtain:

$$\frac{\Delta R}{R_0} = \left[\frac{a\varepsilon / (\varepsilon_1 + \varepsilon)}{1 + R_{J,0} / R_{NS,0}} + 2 \right] \varepsilon \quad (5.14)$$

where

$$a = \frac{k}{R_{NS,0}} \quad (5.15)$$

which fits with the graphene/PEO composites data (solid lines in **fig.5.14**).

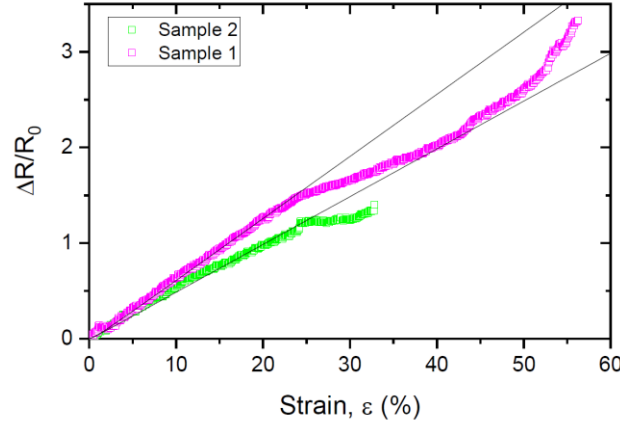


Fig.5.14. Resistance vs strain plot for two samples of PEO/graphene samples.

By integrating Eq. 5.13 we found that $R_J \approx k\varepsilon^2 / (2\varepsilon_1 + \varepsilon)$ and combining these equations we obtained a semi-empirical model that described the strain dependence of the composite resistance. Therefore, for $G_{NS} \neq 0$:⁵⁹

$$\frac{\Delta R}{R_0} = \left[\frac{G_{NS} + a\varepsilon / (\varepsilon_1 + \varepsilon)}{1 + R_{J,0} / R_{NS,0}} + 2 \right] \varepsilon \quad (5.16)$$

This equation fits very well with all experimental data as displayed (solid lines) in **figure 5.10 A**. Furthermore, we could find a direct relationship between the gauge factor of the composite with the gauge factor of the nanosheets, the junction resistance, and the nanosheets resistance. In fact, by definition, the gauge factor is measured at low strain and taking the limit of equation 5.16 at low strain we could obtain

$$\frac{\Delta R}{R_0} = \left[\frac{G_{NS}}{1 + R_{J,0} / R_{NS,0}} + 2 \right] \varepsilon \quad (5.17.a)$$

which can be re-written:

$$G = \frac{G_{NS}}{1 + R_{J,0} / R_{NS,0}} + 2 \quad (5.17.b)$$

Considering that for MoS₂ nanosheets $G_{NS} = -50$,³⁶⁰ it was possible to substitute this value to the equation above to find the ratio $R_{J,0}/R_{NS,0}$. After that, we were able to plot this ratio as a function of the volume fraction, ϕ (**fig. 5.15**).⁵⁹ From the graph below, we can see that the nanosheet resistance is similar to the junction resistance in all cases. This validates our initial theory which states that the junction resistance is not the only limiting factor in the PEO/MoS₂ composite electrical properties.

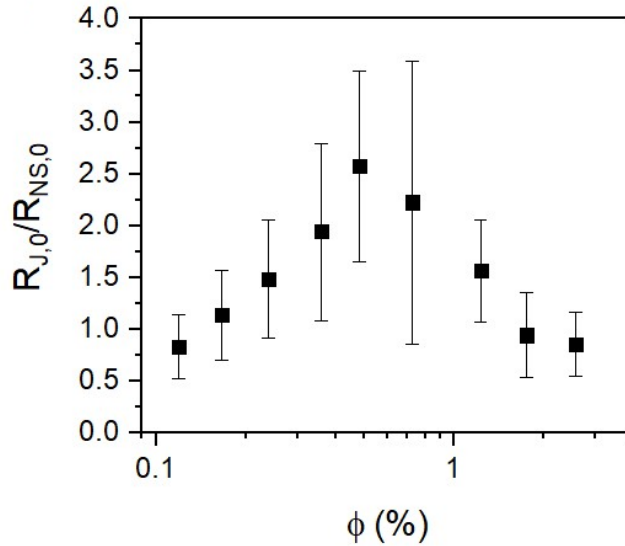


Fig.5.15. Ratio of zero-strain junction resistance to zero-strain nanosheet resistance calculated using equation 5.14b and plotted versus ϕ . The error bars combine the error in G with an assumption that the error in G_{NS} is ± 10 .⁵⁹

However, we also noted that these data are not in agreement with the tunnelling models.⁴⁰⁰ In fact, this model would predict a particle separation thus, R_J to decrease as the volume fraction, ϕ , increases. However, we have to bear in mind that tunnelling models do not describe all the effects involved in the strain-dependent conductivity changes which explain why it is not in agreement with these results.

Finally, it is remarkable to note that the data shows a peak at $\phi \approx 0.5\%$ where aggregation starts to occur (**fig.5.6 B**).

Moreover, combining the value of the network mobility of MoS₂ ($0.15 \text{ cm}^2\text{V}^{-1}\text{s}^{-1}$)²⁸ with the conductivity of a PEO doped nanosheet network ($\sigma_0 = 1.73 \text{ mS}\cdot\text{m}^{-1}$), we could estimate the carrier density in the nanosheets ($4\cdot 10^{20} \text{ m}^{-3}$).⁵⁹ Also, using the intrinsic nanosheet mobility ($50 \text{ cm}^2\text{V}^{-1}\text{s}^{-1}$)²⁸ we could estimate the nanosheet conductivity ($\sigma_{\text{NS}} \approx 0.5 \text{ S}\cdot\text{m}^{-1}$) and, knowing the nanosheet thickness ($\sim 5.5 \text{ nm}$), we could find that $R_{\text{NS},0} \approx 400 \text{ M}\Omega$.⁵⁹ Considering that the junction resistance is similar to the nanosheets resistance (**figure 5.15**), it is fair to assume that junction resistances of this magnitude can be similar to other 2D materials. This implies that for similar junction resistance, more conductive 2D materials should lead to less negative gauge factors. In fact, if the nanosheet conductivity increases without significant changes of the junction resistance, then $R_{\text{J},0} \gg R_{\text{NS},0}$ and the nanosheets resistance under strain have less effect on the composite resistance.

To confirm this theory, we prepared PEO composites filled with nanosheets of WS₂, MoSe₂, WSe₂, and graphene in order to compare their properties, all at the same nanosheet volume fraction of 0.12 vol %.⁵⁹ Electromechanical tests were performed on the sample in order to find the conductivity at zero-strain (**Fig.5.16 A-D**). Then, it was possible to obtain the G values and compare them with PEO/MoS₂ values (**fig.5.17**). The first thing we noticed observing the R- ϵ curves shown below in **figure 5.16** is the difference in the shape of the curves compared to those of PEO/MoS₂ composites.⁵⁹ In fact, we can see how the negative slope of the R- ϵ curve, before the yield point, becomes less steep, denoting a decrease of the negative gauge factor as the conductivity rises until it becomes positive for the PEO/graphene composite (**fig.5.17 B**) which confirmed the validity of the equation 5.17b.

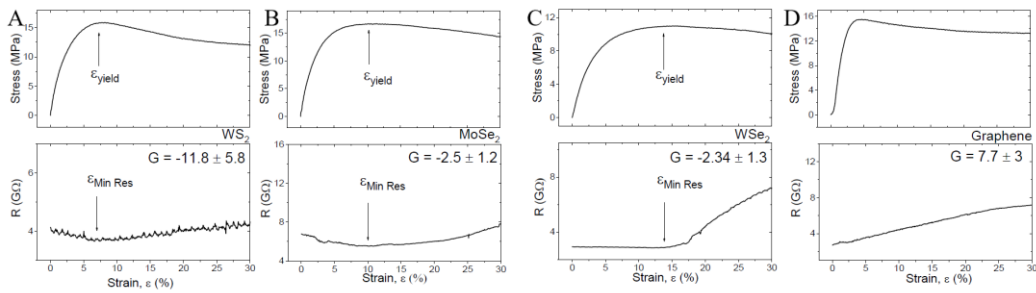


Fig.5.16. Typical stress/strain (top) and resistance/strain (bottom) curves of WS_2/PEO (A), $MoSe_2/PEO$ (B), WSe_2/PEO (C) and graphene/PEO (D) composites (all at $\phi = 0.12$ vol.-%).⁵⁹

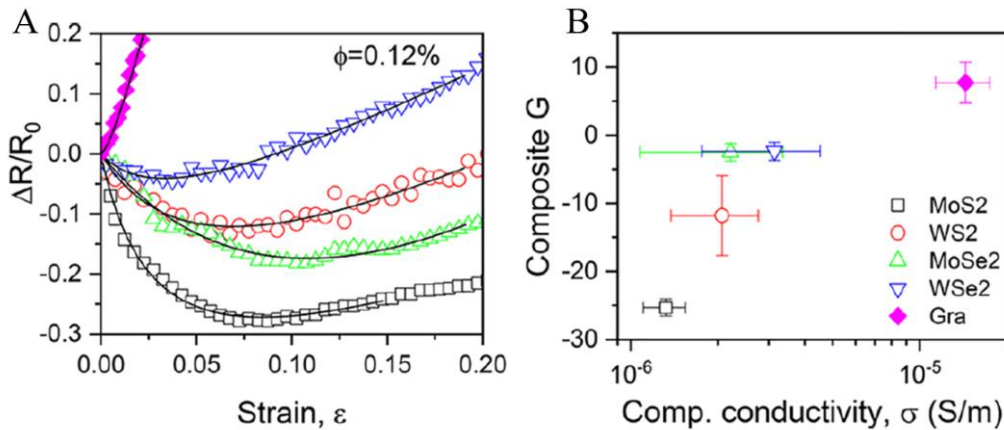


Fig.5.17. Representative resistance-strain curves for composites of PEO filled with 4 different types of TMD nanosheet as well as graphene (all at $\phi = 0.12$ vol.-%, A). Gauge factors for the composites shown in A plotted versus measured composite conductivity (B). The colour coding used in B also applied to A.⁵⁹

5.4 CONCLUSIONS

This study showed another branch of piezoresistive materials which has barely explored before, demonstrating that is possible to harness the band gap of semiconductors in order to obtain a dynamic sensor. In order to do so, we proposed the fabrication of composites realized with liquid exfoliated nanosheets of MoS_2 . These nanosheets were blended with polyethylene oxide (PEO) and

electromechanical tests are performed in order to investigate both mechanical reinforcement from the addition of the nanofiller to the polymer and the electrical performance of the composites.⁵⁹ Furthermore, we highlighted the differences between the PEO/MoS₂ and the composites prepared using graphene and other TMDs (WS₂, MoSe₂, WSe₂) as nanofillers. This has been done with the purpose of showing the interesting and perhaps useful properties that can be modulated, such as both positive and negative gauge factor and a minimum resistance at some critical strain %. We found noteworthy reinforcement and strain-induced Raman band shift, indicating the strain transfer from the polymeric matrix to the filler. Moreover, the PEO acts as a dopant and increases the conductivity of the composite resulting in conductivity value of $>10^{-5}$ S/m.⁵⁹ Most importantly, we found a reduction in resistance at low strain due to a band gap change of the nanoparticles, consistent with the influence of the negative piezoresistive filler, followed by a resistance increase above the yield strain due to tunnelling. We showed that this behaviour can be explained by a combination of strain-induced deformation (at low strain) coupled with strain induced modification of junction resistance (high strain). We demonstrated in this way that it is possible to harness the band-gap of conducting nanosheets inserted in the appropriate matrix to produce dynamic strain sensors. We finally developed a simple model to describe this data which relates, not just the junction resistance to the gauge factor of different types of 2D materials but, also to the nanosheets resistance predicting the composite gauge factor to decrease as the nanosheet conductivity increases.⁵⁹ This work can be considered a starting point towards the exploration of negative gauge factor piezoresistive nanocomposites, giving a better comprehension of piezoresistive materials and marking a new pathway in sensing technology

Experimental Design of polymer:polymer /graphene nanocomposites

6.1 INTRODUCTION

Since the first G-Putty was made,¹³⁷ it has been one of the main interests in this research group to better understand and finally optimise this material.¹³⁸ In fact, just adding graphene to a viscoelastic polymer (commercially called Silly Putty), it was possible to prepare a composite with incredible sensing properties (reaching high gauge factor values) and with high potential in several fields, including biomedicine.^{137,138} This material represented a landmark in the sensing world not just for its properties but, also for the low cost and simplicity of the material preparation. This consists, firstly, in the PDMS (or Silly Putty) crosslinks formation via polycondensation reaction of silicone oil and boric acid (**fig.6.1**), with the addition of graphene afterwards.^{137,138}

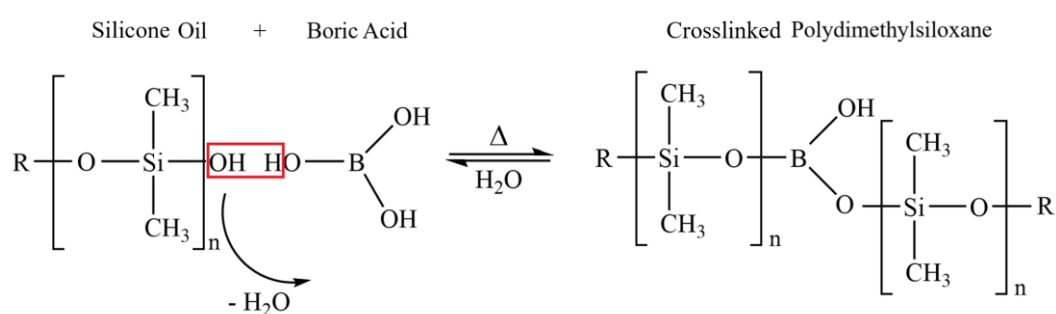


Fig.6.1. Crosslinking condensation reaction of PDMS.

However, despite the fact that G-putty shows incredible sensing properties,^{137,138} the high mobility of the polymeric chains influences the polymer's chain relaxation which negatively affects the hysteresis (**fig.6.2**) and consequently on electrical

properties which are unstable and change over time. For this reason, we needed a polymer that would not interact with the chemistry of the G-putty and its sensing properties (i.e. another type of PDMS), but that would improve the mechanical properties. This also implies that the mixture has to be made with the right proportions in order to optimize both hysteresis and gauge factor.

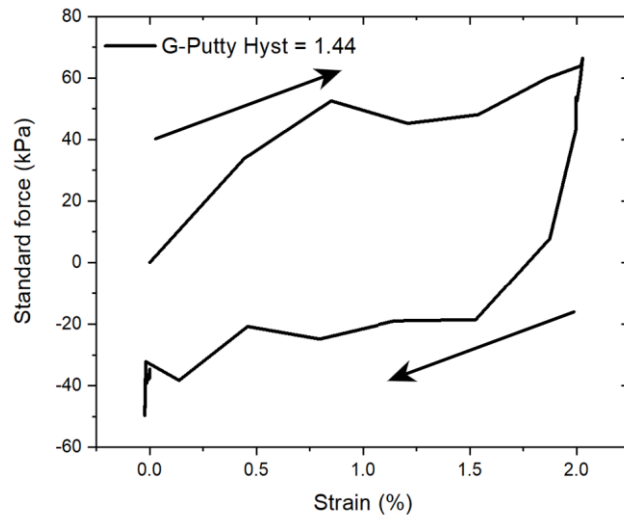


Fig.6.2. *Representative stress-strain curve of G-Putty with 12.5 wt.% of graphene loading level and its hysteresis value (inset).*

The final project of this thesis consists of realizing a dynamic strain sensor embedding the characteristics of more than one polymeric matrix with graphene properties. In order to do so, a statistical method called design of experiments (DOE) was used. As mentioned in **chapter 2.5**, DOE is a systematic method capable of determining the relationship between factors of a process and the output/s affecting that process. In the DOE language, factors are the variables involved in an experiment (i.e. time, temperature, reagents, etc.) and the responses are the results obtained in an experiment. In other words, DOE is utilized to find the cause-effect relationship of an experiment.¹¹⁹

Generally, a research study requires a certain amount of sampling to be completed, and if the number of variables involved is two or three, the whole study does not excessively affect the cost and/or time necessary to complete the experiment. But

what happens if the variables involved number more than three or four? The number of samples necessary to have a widespread study increases considerably, leading to higher costs and longer times which is simply not feasible. (**fig.6.3**).

Variables		Minimum number of samples
2	—————→	4
3	—————→	6
4	—————→	24
5	—————→	120
6	—————→	720
7	—————→	5040

Fig.6.3. *Minimum number of samples required for a study (right) depending on the number of variables involved in the experiment (they follow an $n!$ relationship).*

For this reason, a systematic method is necessary for experiments that require a high number of variables. DOE is comprised of five steps that are necessary to obtain reliable results. These steps are fully described in **chapter 2.5**, while this chapter is focused on experimental procedures used to prepare the samples rather than just explaining the software.

In this thesis, a strain sensor was prepared by mixing two polymeric matrixes: the first one, Polydimethylsiloxane, prepared via polycondensation reaction of silicone oil with boric acid, the second polymeric matrix is an industrial silicone encapsulant called Sylgard 170®. The Sylgard is comprised of two liquid parts which form a flexible elastomer when thoroughly mixed (ratio 1:1). The polymers were mixed with graphene then electromechanical analyses were performed on the final nanocomposite and gauge factor and hysteresis were measured.

6.2 PROCEDURE

6.2.1 Preliminary Studies on the Variables and Program Settings

The first thing we need to consider is the effect of mixing the different compounds on the final sample. With the purpose of obtaining a dynamic strain sensor, we need a composite which shows a low hysteresis (**chapter 2.4.4**) and high gauge factor (**chapter 2.4.4** and **chapter 5**). In order to find the working range for each test, preliminary studies on the properties of the components have been performed. In this way, it was possible to skim the factors that needed to be included in the variation.

G-PUTTY COMPOSITE

The G-putty was prepared following the previously published procedure:^{137,138} Two millilitres of silicone oil was mixed with boric acid at a concentration of 300 mg/ml in a vial. Six vials were prepared in the same way and immersed in an oil bath at ~220 °C for 150 minutes. Once ready, the PDMS was dissolved in IPA and specific amounts of graphene dispersed in IPA added to the solution. The mixture was stirred and heated on a hot plate until the solvent evaporated forming the final G-Putty.^{137,138}

SYLGARD 170®

The elastomer was prepared following the instructions from the company. The two liquid components could simply be mixed and the polymer could be cured at room temperature. The instructions also provided the curing time as a function of the temperature (**Table.6.1**).²³⁴

Table 6.1. Curing time at a specific temperature.²³⁴

Temperature (°C)	Curing time
25	24 hr
50	45 min
70	25 min
85	15 min
100	10 min

After we mixed the two liquid components of the Sylgard with the G-putty dissolved in IPA (ratio 50/50, with a total mass fraction of graphene = 12.5 wt.-%), it was possible to let the solvent evaporate and cure. The first thing we noticed was that the G-putty inhibits the curing agent, and after more than 24 hours, the elastomer was still in a viscous liquid form. Thus, we decided to operate at higher temperatures in order to catalyse the curing reaction and obtain the elastomer. For this reason, a preliminary study on the effect that the temperature has on the G-Putty' gauge factor overtime was executed (**fig.6.4**). Here, the gauge factor of G-Putty was recorded for each temperature after 30, 60, 120 and 360 minutes.

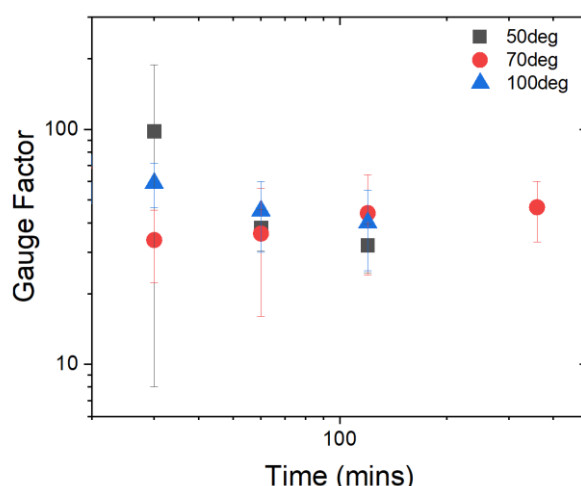


Fig.6.4. Gauge factor as a function of time at 50 (black square), 70 (red circle) and 100 °C (blue triangle).

The first thing we noticed from the graph above was that the gauge factor values did not change significantly for the different temperatures over time. Also, we noticed that the samples heated at 50 and 100 °C were not stable after 3 hours of heating, and the gauge factor could not be calculated for these samples. However, after several tests at different temperatures and times, and considering the curing times/temperatures of the Sylgard, the curing parameters were set to 100 °C for 150 minutes.

We have to bear in mind that for sensing purposes, the mechanical properties of the composite are as important as the electrical ones. Hence, the material has to be soft and at the same time, elastic. The parameters that influence the mechanical properties of this composite are silicone oil viscosity and the ratio between graphene, PDMS and Sylgard. The first factor we set was the silicone oil viscosity. We decided to include 3 different oil viscosities in the study: 1k, 10k and 100k cst. Another parameter we could fix was the graphene. In fact, the minimum amount of graphene required for conductivity is 12.5 wt.-% over the total composite. In order to decide the range of silly putty and Sylgard, we prepared three different ratios of Sylgard/PDMS (**fig.6.5**) using the lowest silicone oil viscosity to prepare the PDMS (thus with the worst hysteresis). First of all, we have to point out that for Sylgard in amounts lower than 30 wt.-% the sample does not cure, forming a paste once the graphene is added to the mixture. From **figure 6.5**, we first notice how the hysteresis decreases as the Sylgard amount increases. Because the hysteresis of the composite matrix is higher than one for the 50:50 composite ratios, the PDMS amount cannot be higher than 50 wt.-% (**fig.6.5 b**).

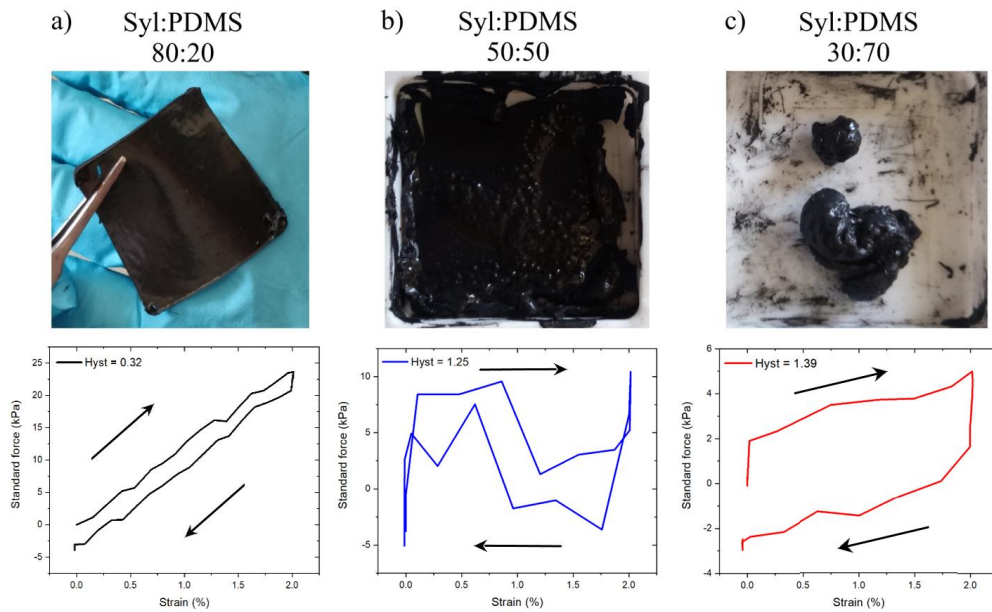


Fig.6.5. Images (top) with the relative cyclic stress-strain curve (bottom) and hysteresis values (inset) of 80:20 (a), 50:50 (b) and 30:70 (c) Sylgard/PDMS ratios.

After we had a clearer idea of the factors involved in this experiment and their working range, it was possible to set the program. After we defined the factors' range, we set the responses deciding to maximize the gauge factor and minimize the hysteresis. Finally, a table of specific tests to perform was designed by the program (Table 6.2).¹¹⁹

Table 6.2. *Designed tests obtained from the DOE after the preliminary study.*

Sample Name	Graphene %	Sylgard %	PDMS %	Oil Viscosity cst
DOE 1	12.5	30	57.5	10k
DOE 2	12.5	30	57.5	100k
DOE 3	12.5	77.5	10	100k
DOE 4	12.5	30	57.5	1k
DOE 5	12.6	77.4	10	10k
DOE 6	12.6	77.4	10	1k
DOE 7	12.6	77.4	10	100k

6.2.2 Sample preparation

The samples were prepared following the procedure described below. Firstly, the liquid components of Sylgard were poured in a Teflon dish and thoroughly mixed. After that, the PDMS previously prepared with the method described before^{137,138} was dissolved in a beaker and the graphene added. The mixture was stirred on a hotplate until the solvent was almost all evaporated (5 ml or less left) to favour the incorporation with the Sylgard. After the PDMS with graphene and Sylgard was mixed until homogeneous, and spread uniformly in the Teflon dish, the solvent was left to evaporate overnight. Finally, the sample was cured at 100 °C for 150 minutes and then ready to be analysed.

6.2.3 Electromechanical testing

Composite films were cut creating uniform strips with a width of 2.25 mm and a thickness of 0.5 mm for each strip. The strips were attached to the clamps of the tensile tester at a distance of 9.73 mm apart and connected to a source meter and electrical measurements were recorded using a LabView program. From these tests, both hysteresis and gauge factor were obtained. In order to find the hysteresis, a cycle test was performed straining the samples up to 10% strain (10 mm/min speed test). As mentioned in **chapter 2.4.7**, the hysteresis, H, represents the energy loss

that occurs in a viscoelastic material during loading and unloading cycles. It is possible to calculate the (mechanical) hysteresis by evaluating the area of from the stress-strain curve or simply using the formula:^{220,312}

$$H = \frac{\sigma_0 - \sigma_i}{\sigma_0} \quad (6.1)$$

where σ_0 and σ_i are the load and unload stress respectively, taken at the same value of the strain applied (**fig.6.6**). Here, the hysteresis can assume values from 0 to 1 (the PDMS by itself can go over 1), and the scope of this work is to minimize this value.

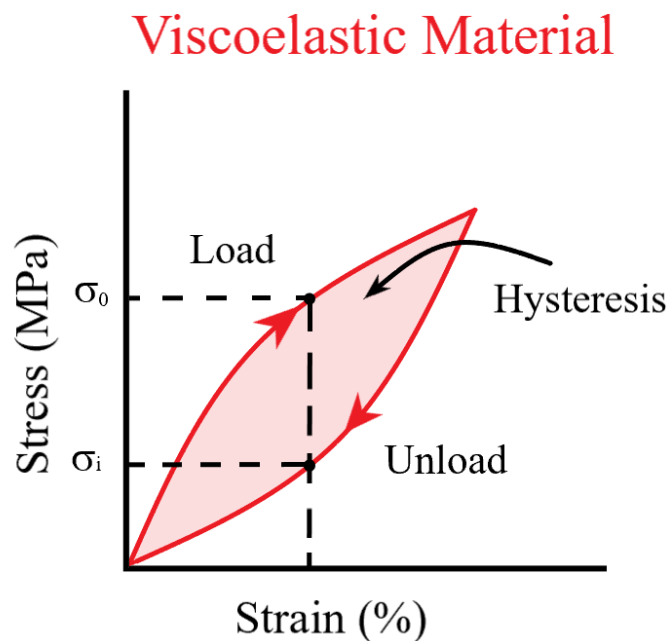


Fig.6.6. *Representative stress-strain curve of a viscoelastic material during a loading-unloading cycle.*

To obtain the gauge factor, the samples were strained (10 mm/min speed test) and both stress and resistance of the samples were recorded, and, as well as for PEO composites (**chapter 5**), we extrapolated G values from R- ϵ curves by determining the slope of the $\Delta R/R_0$ versus strain graph.

A sine wave simulation program was used on samples to obtain a dynamic strain profile for different frequencies (0.5 and 1.5 Hz). Also, in this case, a minimum number of 7 tests per sample were performed, computing the average and standard deviation through Origin software.

6.3 RESULTS

Seven or more tests were performed for each sample and the hysteresis values were calculated using the load, σ_0 , and the unload, σ_i , stress at a 5% strain (**fig.6.7**). The average values were calculated and reported in the DOE table.

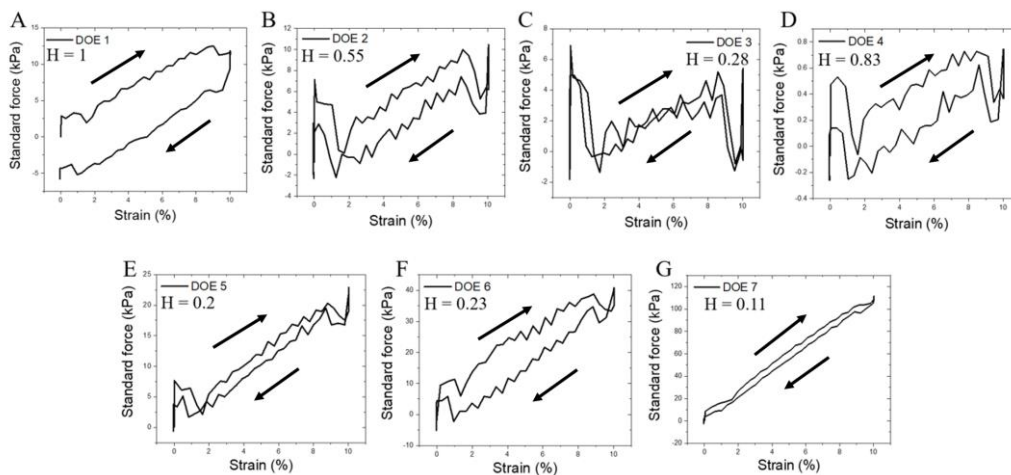


Fig.6.7. Stress-strain curves with calculated hysteresis (inset) for each sample prepared. Here, the sample names correspond to DOE 1 (A), DOE 2 (B), DOE 3 (C), DOE 4 (D), DOE 5 (E), DOE 6 (F) and DOE 7 (G) reported in table 6.2.

The G values were obtained for each sample and, even in this case, 7 tests were performed for each sample. The average values from the tests were reported on the DOE table. In **figure 6.8** we can see a representative curve of each sample with the

average gauge factor value (inset). However, DOE 1 and DOE 5 were not conductive and did not show any change in resistance as the strain was applied. This resulted in a gauge factor equal to zero.

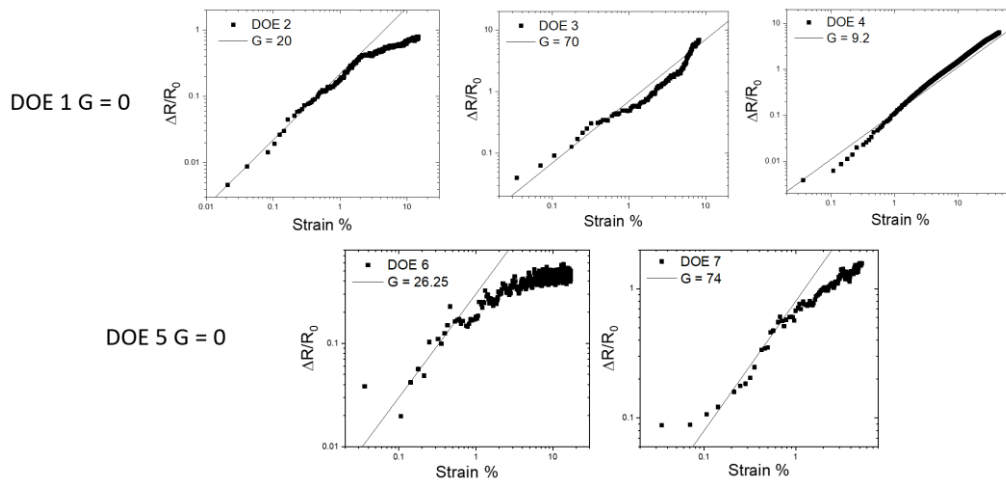


Fig.6.8. Representative curves of fractional resistance change, $\Delta R/R_0$, as a function of strain for each sample (the name of the sample is reported inside the graph). The average G values were obtained and inserted in the table.

After all the results were reported, a model was applied (**fig.6.8**) obtaining a report of the design with a prediction profiler computed by the program (**fig.6.9**).

	Graphene	Sylgard	PDMS	Oil Viscosity	Gauge factor	Hysteresis
1	0.125	0.3	0.575	10	0	1
2	0.125	0.3	0.575	100	20	0.55
3	0.125	0.775	0.1	100	70	0.28
4	0.125	0.3	0.575	1	9.2	0.83
5	0.126	0.774	0.1	10	0	0.2
6	0.126	0.774	0.1	1	26.25	0.23
7	0.126	0.774	0.1	100	74	0.11

Fig.6.9. Table of DOE with reported results.

The prediction profiler is able to give a visual idea of how changes in the factor settings affect both hysteresis and gauge factor. Here, the responses are reported on

the left of the graphs and the factors on the bottom of the graph. Aside from the responses and the factors, the prediction profiler also displays the desirability parameter (from 0 to 1). This parameter represents how close the responses are to the desired values.

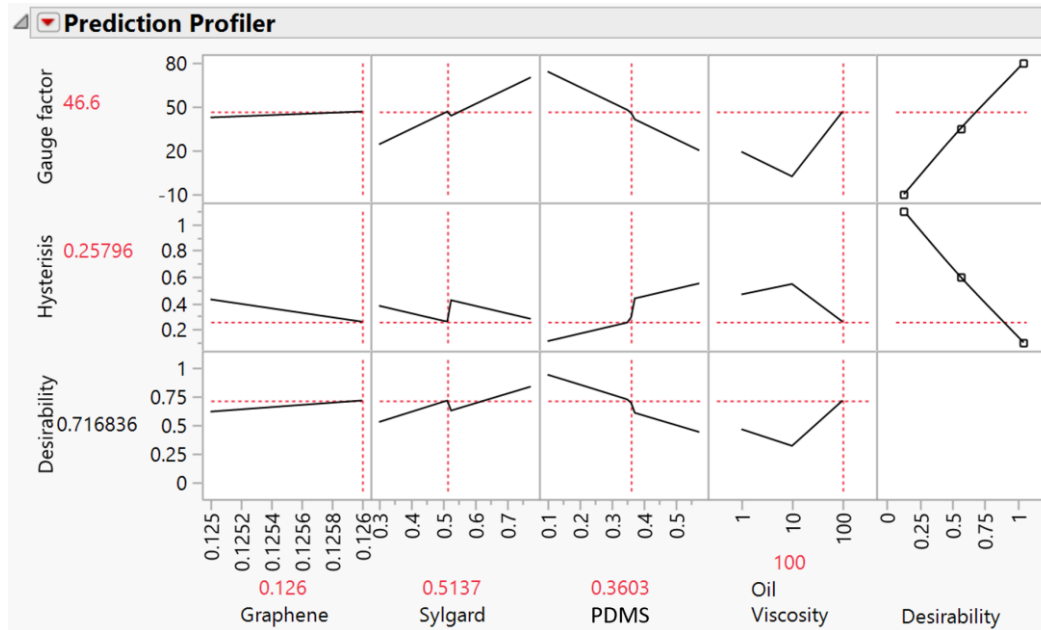


Fig.6.10. Prediction profiler with a selection of random factors. For those factors values (bottom row, red), the program predicted a hysteresis of ~0.26 and a gauge factor of 46.6 (red values on the left).

In order to verify the validity of this method, random values of graphene (12.6 %), Sylgard (51.37 %), PDMS (36.03 %) and oil viscosity (100k) were selected from the prediction profiler graph (Fig.6.10). A sample was prepared and electromechanical analysis was performed and both the hysteresis and the gauge factor obtained from the study were compared with the predicted ones (Hysteresis ≈ 0.258 ; Gauge factor = 46.6). In figure 6.11, the results of the tests show a very good agreement with the values predicted by DOE demonstrating the reliability of this model.

As a final step of this project, we selected factor values with the optimal settings, thus, the ones which would give us the highest gauge factor and the lowest

hysteresis possible for this experiment. In this way, we obtained a hysteresis equal to 0.11 and a gauge factor of 74 (**fig.6.12**) which shows an excellent compromise between low hysteresis and, at the same time, high gauge factor.

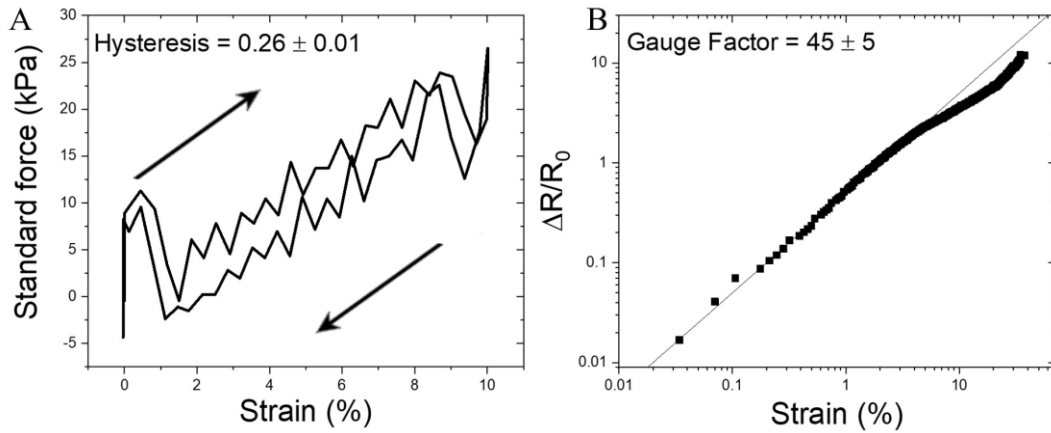


Fig.6.11. Stress-strain curve (A) and fractional resistance change as a function of strain % (B) of the random sample prepared to verify the reliability of the DOE.

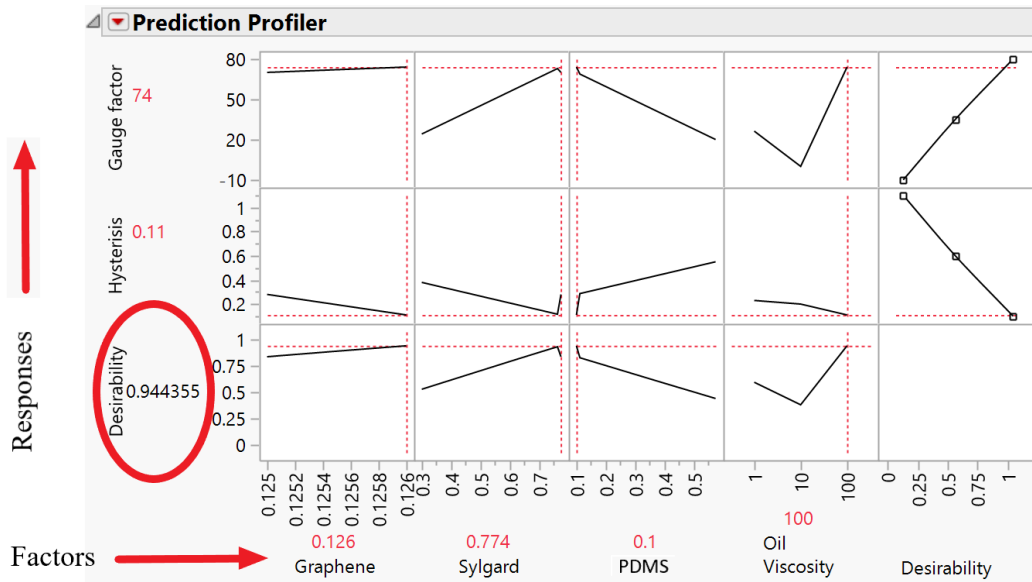


Fig.6.12. Prediction profiler showing the factors and responses values of the best sample.

After optimizing the final sample (fig.6.13), dynamic tests were performed on the composite to demonstrate that this sample can also be used as a strain sensor. As expected, the resultant resistance displays a harmonic response in each case, as the strain is applied (fig.6.14).

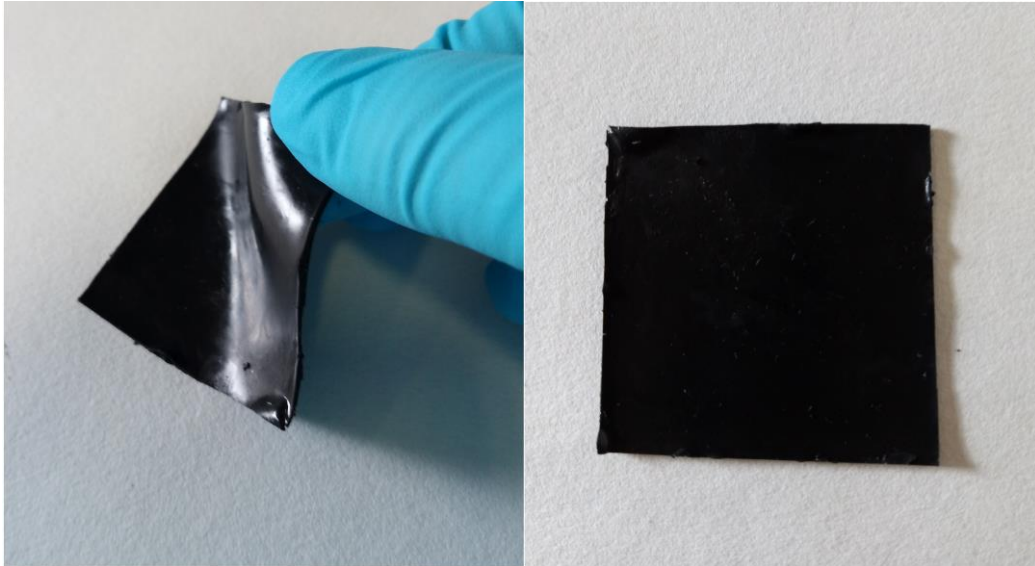


Fig.6.13. Images of the final nanocomposite. The sample appeared homogeneous inspecting by eye and showed considerable flexibility.

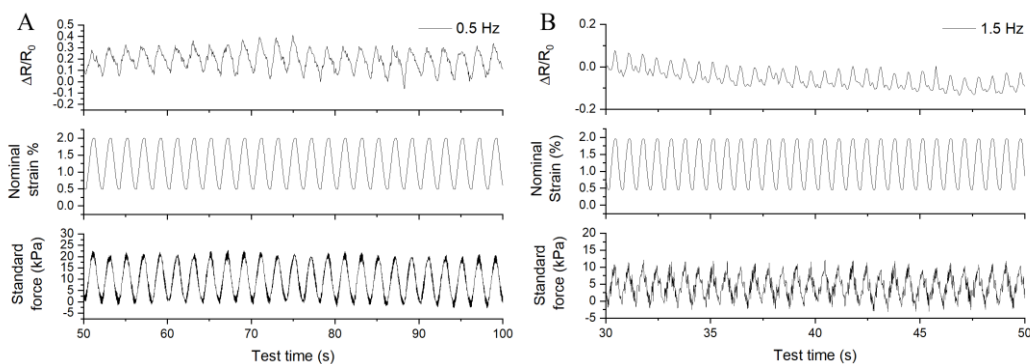


Fig.6.14. Dynamic strain profiles with the resultant resistance response oscillating at two different frequencies: (A) 0.5 Hz and (B) 1.5 Hz.

Furthermore, a creep test was executed on the sample in order to check the stability of the resistance. The test was performed at 4% strain (**fig.6.15**) and the resistance (**fig.6.15 top row**), the strain (**fig.6.15 middle row**), and the stress (**fig.6.15 bottom row**) as a function of time were recorded, showing relative stability for a couple of minutes after which a chain relaxation starts to occur.

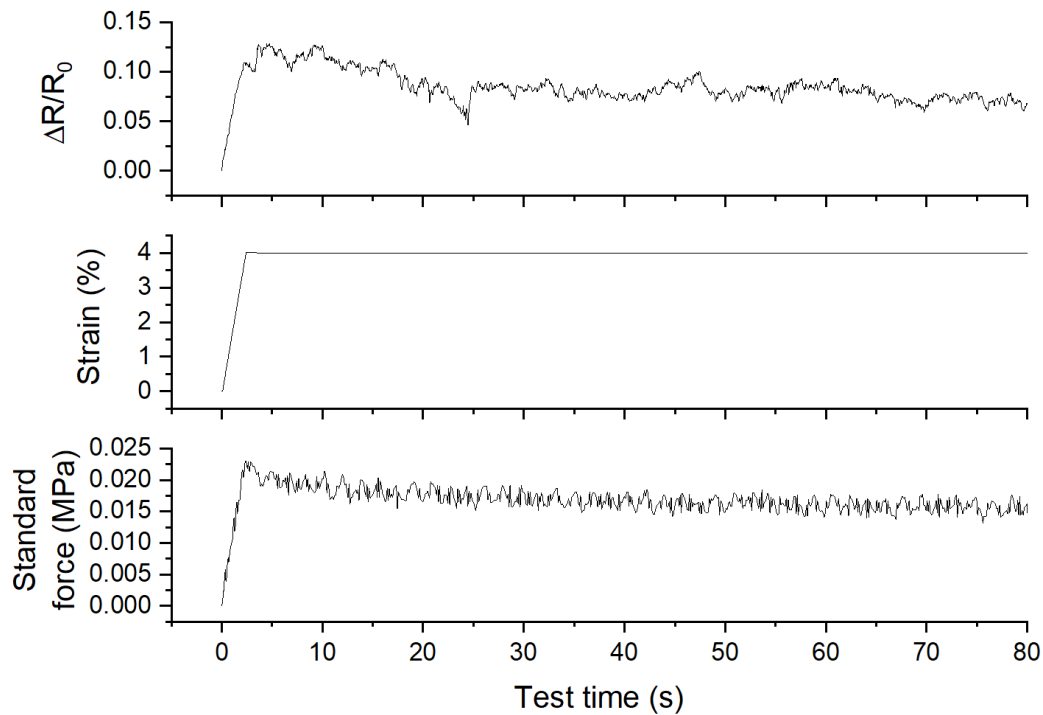


Fig.6.15. Responses of Sylgard/PDMS/graphene composite to step strains of 4%. Top row: fractional resistance change. Middle row: applied strain. Bottom row: stress.

Both cycle (**fig.6.16A**) and creep tests (**fig.6.16B**) were performed on the correspondent G-Putty, in order to see the differences on the electromechanical properties caused by high hysteresis values. In fact, as we can see from **fig.6.16**, the G-Putty shows a high resistance decay after just a few seconds of testing.

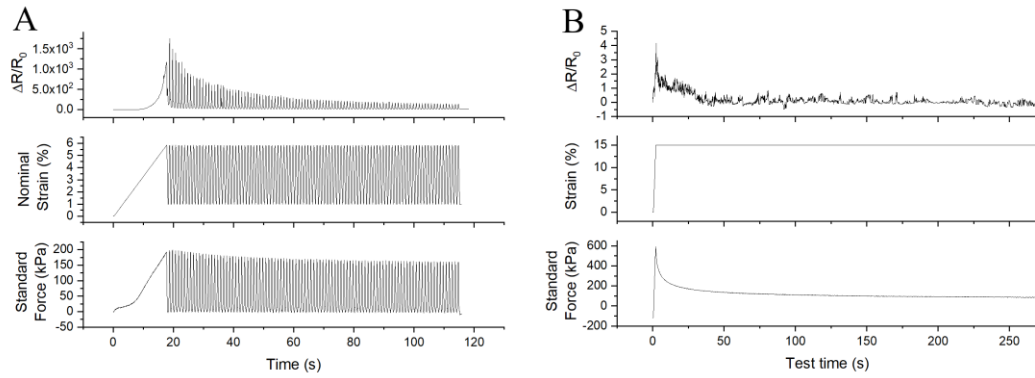


Fig.6.16. Representative graphs of sine test (A) and creep test (B) of G-Putty and the typical resistance decay (top row), strain applied (middle row) and stress (bottom row).

6.4 CONCLUSIONS

Following the path of piezoresistive materials, this last experimental project aimed to optimize polymeric composite properties using two different silicon-based matrices and graphene as a filler. With the intention of optimizing the composite properties (both mechanical and electrical), we built a system where the components involved in the preparation of the composites were combined to maximise the gauge factor and minimise the hysteresis. To do so, we used a statistical program called Design of Experiment (DOE) to reduce process variation and enhance the effectiveness of the experiment, instead of varying one parameter at the time as normally done in a scientific experiment.¹¹⁹ Taking note of this, the need for a preliminary study was apparent as a way to provide a better understanding of the process and of the interaction between the variables of the experiment. In this work, we demonstrated the reliability of this method going through the three steps mentioned next. Initially, the preparation of a protocol was needed to set specific variables' range values. Secondly, thanks to the DOE software package present in a statistics program called JMP, it was possible to formulate a table with a specific set of input variables. After that, the experiments were performed using the protocol previously prepared (described also in **chapter 3**), the set of values produced by the program, and the results of the experiment and these values were added to the table. Subsequently, a mathematical model and a profile prediction was output by the program, showing the relationship between

input and output. Afterwards, to demonstrate the consistency of the prediction, random input values were used for the sample preparation and the effective results were compared to the predicted ones, finding a match between the two. Finally, we prepared the optimized sample reaching an excellent compromise between low hysteresis (0.11) and high gauge factor (74) demonstrating its reliability as dynamic strain sensor and also the higher stability of this composite compared to the corresponding G-Putty.

Conclusions and Future Work

7.1 CONCLUSIONS

Considering the large attention in 2D materials and their incredible potential in technology, the aim of this work was to find a scalable method to produce nanosheets and to introduce these nanoparticles into both simple and complex polymeric systems. One of the reasons that brought us to the production of 2D nanocomposites was not just to investigate on the efficiency of shear mixing exfoliation to produce 2D materials but also to fabricate new, cheap, and high-performance dynamic strain sensors using semiconductors and exploring, in this way, a part of the piezoresistive world which has never been deeply studied. While scale-up exfoliation of 2D material such as graphene, BN, and MoS₂ has been abundantly studied in several mediums (i.e. solvents, water/surfactant, polymers); scaling up other 2D materials, such as tungsten disulphide, has been found challenging especially for large scale production in non-toxic medium (i.e. water/surfactant).

Because of the incessant interest's growth of this particular material, the first part of this work focused on the scale-up exfoliation of WS₂ in water and surfactant. Here, we demonstrated the scalability of WS₂ production through high shear mixing. This method has been proven to be an efficient technology that can lead to relatively cheap industrial production of nanomaterials. Thanks to empirical metrics obtained by simple optical analysis, the concentration, thickness, and length of WS₂ nanosheets have been calculated. Through the variation of key parameters, it was possible to confirm the scalability of WS₂ exfoliation in water and surfactant (NaC). As expected, it was experimentally shown that WS₂ concentration increases with shear rate, shear time, and initial concentration, while it decreases with volume increase. The exponent of each processing parameter involved in WS₂ scaling-up was successfully found by plotting the concentration of exfoliated WS₂ as a function

of the varied processing parameter. After we determined these scaling parameters, we utilised them to achieve two maximised cases: concentration, obtaining 1.82 g/L in 6 hours, and production rate, P_R , reaching 0.95 g/hour of material during a 10-minute exfoliation cycle, which is one of the highest production rate values of WS_2 ever achieved to this point.³⁰

After that, we prepared composites with PEO and liquid-exfoliated TMDs and graphene nanosheets. We found an increase in the nanosheet network conductivity due to the doping from PEO, resulting in composites that were more conductive than might have been expected. We studied the electromechanical response of the composites; in particular, we focused our attention on PEO/ MoS_2 to establish a physical model able to describe their behaviour. First of all, we saw a composite reinforcement with the stiffness that more than doubled at ~ 0.5 vol. % MoS_2 . This indicates a good polymer-nanosheet stress transfer which results in straining the nanosheets themselves as the composite is subjected to a tensile strain. We observed a negative gauge factor in MoS_2 /PEO composites at low strain. In addition, due to a mechanism such as tunnelling, we saw a resistance increase above the yield strain. The model we developed predicts the composite gauge factor (measured at low strain) and relates it to the nanosheets gauge factor and to the junction resistance. We compared the piezoresistive performances of PEO composites filled with MoS_2 , WS_2 , $MoSe_2$, WSe_2 , and graphene, also finding the gauge factor to be higher for nanocomposites filled with nanosheets of lower conductivity. We finally proved that such composites can be used as dynamic strain sensors through periodical strain cycles. We believe these observations make a significant contribution to materials' physics knowledge, exploring unusual piezoresistive properties of networks and relating them to standard composite physics.⁵⁹

We concluded the research of this thesis with the preparation of strain sensors using the joint properties of two different polymeric matrices and graphene in order to maximise the gauge factor and minimise the hysteresis. Through preliminary studies, we determined the parameters responsible for the main changes in hysteresis and gauge factor. Following this, we were able to insert all the necessary information into the program to prepare a table with tests to perform. After executing all the tests, we demonstrated the reliability of the model used in the

program. In order to do so, we compared the results obtained in a test using random variables with the ones predicted by DOE. We found the two results to be in agreement and we used the program to predict the values of the variables necessary to obtain the optimised samples. We finally showed that the optimised sample can be used as a strain sensor measuring low strain periodic deformations.

7.2 FUTURE WORK

The results presented in this work not only demonstrate the efficiency of a scalable and low-cost method for WS₂ production, but this method has the potential to achieve exfoliation of a wide variety of materials which are important in several application fields. Some of these materials are TMD's and TMO's and it will be challenging to scale them up while avoiding the use of dangerous and non-environmentally friendly solvents.

Another important step successfully achieved was the insertion of TMDs and graphene into a polymeric matrix, obtaining a composite with peculiar properties. In fact, it was possible to harness the bandgap of the nanosheets to prepare dynamic sensors. This opens up a new class of flexible piezoresistive materials with a negative gauge factor, which will be very interesting to investigate in order to find space in applications such as biomonitoring and robotics. It may be interesting to also investigate the effects of nanosheet size in this kind of material with the purpose to see the relationship between nanosheet size and the performance of dynamic sensors.

Finally, we demonstrated that through the use of a statistical model it was possible to study dynamic sensors with a more complex structure in a cheap and efficient way. The combination of Sylgard/PDMS/graphene for sensing purposes is still a subject of study in our group. In fact, the next step is to produce inks able to act as dynamic sensors when deposited on a surface, and the comparison between the results achieved with the ones obtained in this work will be crucial to have a larger picture of these materials' behaviour. Another important aspect for future work would be building a roadmap to obtain dynamic strain sensors that are cheaper and more environmentally friendly while exhibiting higher sensing performance.

REFERENCES

1. Oberlin, A., Endo, M. & Koyama, T. Filamentous growth of carbon through benzene decomposition. *J. Cryst. Growth* **32**, 335–349 (1976).
2. Iijima, S. Helical microtubules of graphitic carbon. *Nature* **354**, 56–58 (1991).
3. Kroto, H. W., Heath, J. R., O'Brien, S. C., Curl, R. F. & Smalley, R. E. C60: Buckminsterfullerene. *Nature* **318**, 162–163 (1985).
4. Novoselov, K. S. *et al.* Electric Field Effect in Atomically Thin Carbon Films. *Science* (80-.). **306**, 666 LP – 669 (2004).
5. Gusmão, R., Sofer, Z. & Pumera, M. Black Phosphorus Rediscovered: From Bulk Material to Monolayers. *Angew. Chemie Int. Ed.* **56**, 8052–8072 (2017).
6. Bizeto, M. A., Shiguihara, A. L. & Constantino, V. R. L. Layered niobate nanosheets: building blocks for advanced materials assembly. *J. Mater. Chem.* **19**, 2512 (2009).
7. Klingshirn, C. *et al.* ZnO rediscovered – once again!? in *Advances in Spectroscopy for Lasers and Sensing* 277–293 (Springer Netherlands, 2006). doi:10.1007/1-4020-4789-4_15
8. Nobuyoshi Miyamoto, N. M. & Teruyuki Nakato*, †, ‡. Liquid Crystalline Nanosheet Colloids with Controlled Particle Size Obtained by Exfoliating Single Crystal of Layered Niobate $K_4Nb_6O_{17}$. (2004). doi:10.1021/JP0363545
9. Varrla, E. *et al.* Large-scale production of size-controlled MoS₂ nanosheets by shear exfoliation. *Chem. Mater.* **27**, 3, 1129-1139 (2015).
10. Harvey, A. *et al.* Preparation of gallium sulfide nanosheets by liquid exfoliation and their application as hydrogen evolution catalysts. *Chem. Mater.* **27**, 9 3483-3493 (2015).

11. Backes, C. *et al.* Production of highly monolayer enriched dispersions of liquid-exfoliated nanosheets by liquid cascade centrifugation. *ACS Nano* **10**, 1589–1601 (2016).
12. Gholamvand, Z., McAteer, D., Harvey, A., Backes, C. & Coleman, J. N. Electrochemical Applications of Two-Dimensional Nanosheets: The Effect of Nanosheet Length and Thickness. *Chem. Mater.* **28**, 8 2641-2651 (2016).
13. Lipomi, D. J. *et al.* Skin-like pressure and strain sensors based on transparent elastic films of carbon nanotubes. *Nat. Nanotechnol.* **6**, 788–792 (2011).
14. Pang, C. *et al.* A flexible and highly sensitive strain-gauge sensor using reversible interlocking of nanofibres. *Nat. Mater.* **11**, 795–801 (2012).
15. Chun, K. Y. *et al.* Highly conductive, printable and stretchable composite films of carbon nanotubes and silver. *Nat. Nanotechnol.* **5**, 853–857 (2010).
16. Ryan, A. J. *et al.* Electroconductive Biohybrid Collagen/Pristine Graphene Composite Biomaterials with Enhanced Biological Activity. *Adv. Mater.* **30**, (2018).
17. McAteer, D. *et al.* Thickness dependence and percolation scaling of hydrogen production rate in MoS₂ nanosheet and nanosheet-carbon nanotube composite catalytic electrodes. *ACS Nano* **10**, 1, 672-683 (2016).
18. Hernandez, Y. *et al.* High-yield production of graphene by liquid-phase exfoliation of graphite. *Nat. Nanotechnol.* **3**, 563–568 (2008).
19. Backes, C. *et al.* Guidelines for exfoliation, characterization and processing of layered materials produced by liquid exfoliation. *Chem. Mater.* **29**, 243–255 (2017).
20. Paton, K. R. *et al.* Scalable production of large quantities of defect-free few-layer graphene by shear exfoliation in liquids. *Nat. Mater.* **13**, 624–630 (2014).
21. Barwich, S., Khan, U. & Coleman, J. N. A Technique To Pretreat Graphite Which Allows the Rapid Dispersion of Defect-Free Graphene in Solvents at High Concentration. *J. Phys. Chem. C* **117**, 19212–19218 (2013).

22. Brennan, L. J., Barwich, S. T., Satti, A., Faure, A. & Gun'ko, Y. K. Graphene–ionic liquid electrolytes for dye sensitised solar cells. *J. Mater. Chem. A* **1**, 8379–8384 (2013).
23. Lotya, M., King, P. J., Khan, U., De, S. & Coleman, J. N. High-Concentration, Surfactant-Stabilized Graphene Dispersions. *ACS Nano* **4**, 3155–3162 (2010).
24. Feng, C., Huang, L., Guo, Z. & Liu, H. Synthesis of tungsten disulfide (WS₂) nanoflakes for lithium ion battery application. *Electrochem. commun.* **9**, 119–122 (2007).
25. Lei, T. *et al.* Multi-Functional Layered WS₂ Nanosheets for Enhancing the Performance of Lithium-Sulfur Batteries. *Adv. Energy Mater.* **7**, 1601843 (2017).
26. Liu, Y. *et al.* WS₂ Nanowires as a High-Performance Anode for Sodium-Ion Batteries. *Chem. - A Eur. J.* **21**, 11878–11884 (2015).
27. Shiva, K., Ramakrishna Matte, H. S. S., Rajendra, H. B., Bhattacharyya, A. J. & Rao, C. N. R. Employing synergistic interactions between few-layer WS₂ and reduced graphene oxide to improve lithium storage, cyclability and rate capability of Li-ion batteries. *Nano Energy* **2**, 787–793 (2013).
28. Kelly, A. G. Printed Electronics from Solution-Processed 2D Materials. *Diss. Trinity College Dublin* (2018).
29. Jo, S., Ubrig, N., Berger, H., Kuzmenko, A. B. & Morpurgo, A. F. Mono- and Bilayer WS₂ Light-Emitting Transistors. *Nano Lett.* **14**, 2019–2025 (2014).
30. Bicca, S. *et al.* Exfoliation of 2D materials by high shear mixing. *2D Mater.* **6**, (2019).
31. Antony, J. Taguchi or classical design of experiments: a perspective from a practitioner. *Sens. Rev.* **26**, 227–230 (2006).
32. Roy, R. K. *Design of experiments using the Taguchi approach : 16 steps to product and process improvement.* (Wiley, 2001).

33. Zhu, Y. *et al.* Graphene and Graphene Oxide: Synthesis, Properties, and Applications. *Adv. Mater.* **22**, 3906–3924 (2010).
34. Donarelli, M. & Ottaviano, L. 2D Materials for Gas Sensing Applications: A Review on Graphene Oxide, MoS₂, WS₂ and Phosphorene. *Sensors (Basel)*. **18**, (2018).
35. Lin Yu-Pu Functionalization of two-dimensional nanomaterials based on graphene. *Diss. Aix-Marseille* (2014).
36. Hidalgo-Manrique, P. *et al.* Copper/graphene composites: a review. *J. Mater. Sci.* **54**, 12236–12289 (2019).
37. Li, Z. *et al.* Effect of the orientation of graphene-based nanoplatelets upon the Young's modulus of nanocomposites. *Compos. Sci. Technol.* **123**, 125–133 (2016).
38. Balandin, A. A. *et al.* Superior Thermal Conductivity of Single-Layer Graphene. *Nano Lett.* **8**, 902–907 (2008).
39. Ebbesen, T. W. & Hiura, H. Graphene in 3-dimensions: Towards graphite origami. *Adv. Mater.* **7**, 582–586 (1995).
40. Kavan, L., Yum, J. H. & Grätzel, M. Optically Transparent Cathode for Dye-Sensitized Solar Cells Based on Graphene Nanoplatelets. *ACS Nano* **5**, 165–172 (2011).
41. Lee, C., Wei, X., Kysar, J. W. & Hone, J. Measurement of the Elastic Properties and Intrinsic Strength of Monolayer Graphene. *Science (80)*. **321**, 385–388 (2008).
42. Bodenmann, A. K. & MacDonald, A. H. Graphene: Exploring carbon flatland. *Phys. Today* **60**, 35–41 (2007).
43. C.A. Wilkie, A.B. Morgan 5 - Nanocomposites I: Current developments in nanocomposites as novel flame retardants *Advances in fire retardant materials* 95-123 (2008) doi.org/10.1533/9781845694701.1.95.
44. Soldano, C., Mahmood, A., Dujardin E. Production, properties and potential of graphene. *Carbon*, **48**, 8, 2127- 2150 (2010).

45. Pumera, M. Electrochemistry of graphene: new horizons for sensing and energy storage. *Chem. Rec.* **9**, 211–223 (2009).
46. Wang, H. H. Flexible Chemical Sensors - Semiconductor Nanomaterials for Flexible Technology. *Elsevire Science*, pp. 247–273 (2010).
47. Bonaccorso, F. & Sun, Z. Solution processing of graphene, topological insulators and other 2d crystals for ultrafast photonics. *Opt. Mater. Express* **4**, 63 (2013).
48. Backes, C. *et al.* Edge and confinement effects allow in situ measurement of size and thickness of liquid-exfoliated nanosheets. *Nat. Commun.* **5**, 1–10 (2014).
49. Smith, R. J. *et al.* Large-Scale Exfoliation of Inorganic Layered Compounds in Aqueous Surfactant Solutions. *Adv. Mater.* **23**, 3944–3948 (2011).
50. Han, S. A., Bhatia, R. & Kim, S.-W. Synthesis, properties and potential applications of two-dimensional transition metal dichalcogenides. *Nano Converg.* **2**, 17 (2015).
51. Nicolosi, V., Chhowalla, M., Kanatzidis, M. G., Strano, M. S. & Coleman, J. N. Liquid Exfoliation of Layered Materials. *Science (80-.)*. **340**, 1226419–1226419 (2013).
52. Boland, J. B. *et al.* Liquid phase exfoliation of MoO₂ nanosheets for lithium ion battery applications. *Nanoscale Adv.* **1**, 1560–1570 (2019).
53. Kim, S. K., Wie, J. J., Mahmood, Q. & Park, H. S. Anomalous nanoinclusion effects of 2D MoS₂ and WS₂ nanosheets on the mechanical stiffness of polymer nanocomposites. *Nanoscale* **6**, 7430–7435 (2014).
54. Hanlon, D. *et al.* Liquid exfoliation of solvent-stabilised black phosphorus: applications beyond electronics. *Nat. Commun.* **6**, 8563 (2015).
55. Wang, Q. H., Kalantar-Zadeh, K., Kis, A., Coleman, J. N. & Strano, M. S. Electronics and optoelectronics of two-dimensional transition metal dichalcogenides. *Nat. Nanotechnol.* **7**, 699–712 (2012).
56. Keeley, G. P. *et al.* Electrochemical ascorbic acid sensor based on DMF-

- exfoliated graphene. *J. Mater. Chem.* **20**, 7864 (2010).
57. Park, M. *et al.* MoS₂-Based Tactile Sensor for Electronic Skin Applications. *Adv. Mater.* **28**, 2556–2562 (2016).
 58. Manzeli, S., Allain, A., Ghadimi, A. & Kis, A. Piezoresistivity and Strain-induced Band Gap Tuning in Atomically Thin MoS₂. *Nano Lett.* **15**, 5330–5335 (2015).
 59. Biccai, S. *et al.* Negative Gauge Factor Piezoresistive Composites Based on Polymers Filled with MoS₂ Nanosheets. *ACS Nano* acsnano.9b01613 (2019). doi:10.1021/acsnano.9b01613
 60. Cong, C. *et al.* Synthesis and optical properties of large-scale single-crystalline two-dimensional semiconductor WS₂ monolayer from chemical vapor deposition. *Advanced Optical Materials*, **2**: 131-136 (2013).
 61. Ovchinnikov, D., Allain, A., Huang, Y.-S., Dumcenco, D. & Kis, A. Electrical Transport Properties of Single-Layer WS₂. *ACS Nano* **8**, 8174–8181 (2014).
 62. Golberg, D. Exfoliating the inorganics. *Nat. Nanotechnol.* **6**, 200–201 (2011).
 63. Wengeler, R. & Nirschl, H. Turbulent hydrodynamic stress induced dispersion and fragmentation of nanoscale agglomerates. *J. Colloid Interface Sci.* **306**, 262–273 (2007).
 64. Wang, L., Loh, K. J., Chiang, W.-H. & Manna, K. Micro-patterned graphene-based sensing skins for human physiological monitoring. *Nanotechnology* **29**, 105503 (2018).
 65. Beeby, S. P., Ensel, G., Kraft, M. & White, N. M. MEMS Mechanical Sensors- Mechanical Transduction Techniques. *Boston: Artech House* (2004).
 66. Canavese, G. *et al.* Piezoresistive flexible composite for robotic tactile applications. *Sensors Actuators, A Phys.* (2014). doi:10.1016/j.sna.2013.11.018

67. Yamada, T. *et al.* A stretchable carbon nanotube strain sensor for human-motion detection. *Nat. Nanotechnol.* **6**, 296–301 (2011).
68. Amjadi, M.; Kyung, K. U.; Park, I.; Sitti, M., Stretchable, Skin-Mountable, and Wearable Strain Sensors and Their Potential Applications: A Review. *Advanced Functional Materials* **26**, 1678- 1698 (2016).
69. Kang, D. *et al.* Ultrasensitive mechanical crack-based sensor inspired by the spider sensory system. *Nature* **516**, 222–226 (2014).
70. Masvidal-codina, E. *et al.* cortical brain activity enabled by graphene. *Nature Mater* **18**, 280–288 (2019) doi:10.1038/s41563-018-0249-4
71. Alzari, V. *et al.* Graphene-containing thermoresponsive nanocomposite hydrogels of poly(N-isopropylacrylamide) prepared by frontal polymerization. *J. Mater. Chem.* **21**, 8727 (2011).
72. Nuvoli, L. *et al.* Double responsive copolymer hydrogels prepared by frontal polymerization. *J. Polym. Sci. Part A Polym. Chem.* **54**, 2166–2170 (2016).
73. Kopeček, J. Smart and genetically engineered biomaterials and drug delivery systems. *Elsevier Science* **20**, 1, 1-16 (2003).
74. Soppimath, K. S., Aminabhavi, T. M., Dave, A. M., Kumbar, S. G. & Rudzinski, W. E. Stimulus-Responsive “Smart” Hydrogels as Novel Drug Delivery Systems. *Drug Dev. Ind. Pharm.* **28**, 957–974 (2002).
75. Gupta, P., Vermani, K., Hydrogels: from controlled release to pH-responsive drug delivery. *Drug discovery today*, **7**, 10 569-579 (2002).
76. Bergin, L. Spookies: Combining smart materials and information technology in an interactive toy. *IDC '05* (2005).
77. Reed, P., Method for making advanced smart cards with integrated electronics using isotropic thermoset adhesive materials with high quality exterior surfaces. *US20080096326A1* (2011).
78. Zhang, X., Lewis, P., Fabrication and characterization of a smart drug delivery system: microsphere in hydrogel. *Biomaterials*, **26**, 16, 3299-3309 (2005).

79. Wang, Z. L. Self-Powered Nanosensors and Nanosystems. *Adv. Mater.* **24**, 280–285 (2012).
80. Wu, W., Wen, X. & Wang, Z. L. Taxel-Addressable Matrix of Vertical-Nanowire Piezotronic Transistors for Active and Adaptive Tactile Imaging. *Science* **340**, 952–957 (2013).
81. Ramadan, K. S., Sameoto, D. & Evoy, S. A review of piezoelectric polymers as functional materials for electromechanical transducers. *Smart Mater. Struct.* **23**, 033001 (2014).
82. Fiorillo, A. S., Critello, C. D. & Pullano, S. A. Theory, technology and applications of piezoresistive sensors: A review. *Sensors Actuators A Phys.* **281**, 156–175 (2018).
83. Barlian, A. A., Park, W.-T., Mallon, J. R., Rastegar, A. J. & Pruitt, B. L. Review: Semiconductor Piezoresistance for Microsystems. *Proc. IEEE* **97**, 513–552 (2009).
84. Hu, N., Karube, Y., Yan, C., Masuda, Z. & Fukunaga, H. Tunneling effect in a polymer/carbon nanotube nanocomposite strain sensor. *Acta Mater.* **56**, 2929–2936 (2008).
85. Abshirini, M., Charara, M., Liu, Y., Saha, M. & Altan, M. C. 3D Printing of Highly Stretchable Strain Sensors Based on Carbon Nanotube Nanocomposites. *Adv. Eng. Mater.* **20**, 1800425 (2018).
86. Christ, J. F., Aliheidari, N., Ameli, A., & Pötschke, P. 3D printed highly elastic strain sensors of multiwalled carbon nanotube/thermoplastic polyurethane nanocomposites. *Materials & Design*, **131**, 394-401 (2017).
87. Lu, Y., Biswas, M. C., Guo, Z., Jeon, J.-W. & Wujcik, E. K. Recent developments in bio-monitoring via advanced polymer nanocomposite-based wearable strain sensors. *Biosens. Bioelectron.* **123**, 167–177 (2019).
88. Ye, X. *et al.* A wearable and highly sensitive strain sensor based on a polyethylenimine-rGO layered nanocomposite thin film. *J. Mater. Chem. C* **5**, 7746–7752 (2017).
89. Clem, P. G., Dimos, D. B., Gonzales, D. M., Ruffner, J. A. & Tuttle, B. A.

- Effect of Substrate Composition on the Piezoelectric Response of Reactively Sputtered AlN Thin Films. *J. Name Thin Solid Film. Other Inf. Submitt. to Thin Solid Film.* (1999).
90. Castellanos-Gomez, A. *et al.* Local strain engineering in atomically thin MoS₂. *Nano Lett.* **13**, 5361–5366 (2013).
 91. Castellanos-Gomez, A. *et al.* Elastic Properties of Freely Suspended MoS₂ Nanosheets. *Adv. Mater.* **24**, 772–775 (2012).
 92. Tsai, M. Y. *et al.* Flexible MoS₂ Field-Effect Transistors for Gate-Tunable Piezoresistive Strain Sensors. *ACS Appl. Mater. Interfaces* **7**, 12850–12855 (2015).
 93. Rahman, R. & Servati, P. Effects of inter-tube distance and alignment on tunnelling resistance and strain sensitivity of nanotube/polymer composite films. *Nanotechnology* **23**, 055703 (2012).
 94. Hysteresis Effect -- from Eric Weisstein's World of Physics. Available at: <http://scienceworld.wolfram.com/physics/HysteresisEffect.html>. (Accessed: 2nd July 2019)
 95. Mechanical hysteresis | Article about mechanical hysteresis by The Free Dictionary. Available at: <https://encyclopedia2.thefreedictionary.com/mechanical+hysteresis>. (Accessed: 2nd July 2019)
 96. Report of the British Association for the Advancement of Science : British Association for the Advancement of Science : Free Download, Borrow, and Streaming : Internet Archive. Available at: <https://archive.org/details/reportofbritisha90brit/page/n9>. (Accessed: 2nd July 2019)
 97. A treatise on the mathematical theory of elasticity : Love, A. E. H. (Augustus Edward Hough), 1863-1940 : Free Download, Borrow, and Streaming : Internet Archive. Available at: <https://archive.org/details/atreatiseonmath01lovegoog/page/n9>. (Accessed: 2nd July 2019)

98. Jayathilaka, W. A. D. M. *et al.* Significance of Nanomaterials in Wearables: A Review on Wearable Actuators and Sensors. *Adv. Mater.* **31**, 1805921 (2019).
99. Lu, Y., Biswas, M. C., Guo, Z., Jeon, J.-W. & Wujcik, E. K. Recent developments in bio-monitoring via advanced polymer nanocomposite-based wearable strain sensors. *Biosens. Bioelectron.* **123**, 167–177 (2019).
100. Ilanchezhyan, P. *et al.* Highly efficient CNT functionalized cotton fabrics for flexible/wearable heating applications. *RSC Adv.* **5**, 10697–10702 (2015).
101. Simate, A. *et al.* Spray-coated carbon nanotube carpets for creeping reduction of conducting polymer based artificial muscles. *Nanotechnology* **28**, 025502 (2017).
102. Jang, N.-S. *et al.* Simple Approach to High-Performance Stretchable Heaters Based on Kirigami Patterning of Conductive Paper for Wearable Thermo-therapy Applications. *ACS Appl. Mater. Interfaces* **9**, 19612–19621 (2017).
103. Hsu, P.-C. *et al.* Personal Thermal Management by Metallic Nanowire-Coated Textile. *Nano Lett.* **15**, 365–371 (2015).
104. Zhai, H. *et al.* Transparent heaters based on highly stable Cu nanowire films. *Nano Res.* **9**, 3924–3936 (2016).
105. Kim, K. K. *et al.* Highly Sensitive and Stretchable Multidimensional Strain Sensor with Prestrained Anisotropic Metal Nanowire Percolation Networks. *Nano Lett.* **15**, 5240–5247 (2015).
106. Ke, K., Pötschke, P., Gao, S. & Voit, B. An Ionic Liquid as Interface Linker for Tuning Piezoresistive Sensitivity and Toughness in Poly(vinylidene fluoride)/Carbon Nanotube Composites. *ACS Appl. Mater. Interfaces* **9**, 5437–5446 (2017).
107. Akter, T. & Kim, W. S. Reversibly Stretchable Transparent Conductive Coatings of Spray-Deposited Silver Nanowires. *ACS Appl. Mater. Interfaces* **4**, 1855–1859 (2012).
108. Lee, H., Seong, B., Moon, H. & Byun, D. Directly printed stretchable strain

- sensor based on ring and diamond shaped silver nanowire electrodes. *RSC Adv.* **5**, 28379–28384 (2015).
109. Ma, R., Kang, B., Cho, S., Choi, M. & Baik, S. Extraordinarily High Conductivity of Stretchable Fibers of Polyurethane and Silver Nanoflowers. *ACS Nano* **9**, 10876–10886 (2015).
 110. Wang, J. *et al.* A highly sensitive and flexible pressure sensor with electrodes and elastomeric interlayer containing silver nanowires. *Nanoscale* **7**, 2926–2932 (2015).
 111. Wang, W., Yang, T., Zhu, H. & Zheng, Q. Bio-inspired mechanics of highly sensitive stretchable graphene strain sensors. *Appl. Phys. Lett.* **106**, 171903 (2015).
 112. Sun, B. *et al.* Fabrication of curled conducting polymer microfibrillar arrays via a novel electrospinning method for stretchable strain sensors. *Nanoscale* **5**, 7041 (2013).
 113. Shang, S., Yue, Y. & Wang, X. Piezoresistive strain sensing of carbon black /silicone composites above percolation threshold. *Rev. Sci. Instrum.* **87**, 123910 (2016).
 114. Seyedin, M. Z., Razal, J. M., Innis, P. C. & Wallace, G. G. Strain-Responsive Polyurethane/PEDOT:PSS Elastomeric Composite Fibers with High Electrical Conductivity. *Adv. Funct. Mater.* **24**, 2957–2966 (2014).
 115. Liu, S. *et al.* A high performance self-healing strain sensor with synergetic networks of poly(ϵ -caprolactone) microspheres, graphene and silver nanowires. *Compos. Sci. Technol.* **146**, 110–118 (2017).
 116. Li, M., Li, H., Zhong, W., Zhao, Q. & Wang, D. Stretchable Conductive Polypyrrole/Polyurethane (PPy/PU) Strain Sensor with Netlike Microcracks for Human Breath Detection. *ACS Appl. Mater. Interfaces* **6**, 1313–1319 (2014).
 117. Jones, R. Design and Analysis of Experiments. *Qual. Reliab. Eng. Int.* **18**, 163–163 (2002).
 118. Mayergoyz, I. D. Mathematical models of hysteresis and their applications.

Elsevier Science (2003).

119. Konda, R., Rajurkar, K. P., Bishu, R. R., Guha, A. & Parson, M. Design of experiments to study and optimize process performance. *Int. J. Qual. RI. Konda, R., Rajurkar, K. P., Bishu, R. R., Guha, A. Parson, M. Des. Exp. to study Optim. Process performance. Int. J. Qual. Reliab. Manag.* **16**, 56–71 (1999).
120. Fisher, R. A. Statistical Methods for Research Workers. in 66–70 (Springer, New York, NY, 1992). doi:10.1007/978-1-4612-4380-9_6
121. Silva, A. F., Neves, P., Rocha, S. M., Silva, C. M. & Valente, A. A. Optimization of continuous-flow heterogeneous catalytic oligomerization of 1-butene by design of experiments and response surface methodology. *Fuel* **259**, 116256 (2020).
122. Baig, U., Uddin, M. K. & Gondal, M. A. Removal of hazardous azo dye from water using synthetic nano adsorbent: Facile synthesis, characterization, adsorption, regeneration and design of experiments. *Colloids Surfaces A Physicochem. Eng. Asp.* **584**, 124031 (2020).
123. Smith, J. D., Sreedharan, V., Landon, M. & Smith, Z. P. Advanced design optimization of combustion equipment for biomass combustion. *Renew. Energy* **145**, 1597–1607 (2020).
124. Reddy, K. S. & Ananthasornaraj, C. Design, development and performance investigation of solar Parabolic Trough Collector for large-scale solar power plants. *Renew. Energy* **146**, 1943–1957 (2020).
125. Park, J. *et al.* The design and testing of a kW-class free-piston Stirling engine for micro-combined heat and power applications. *Appl. Therm. Eng.* **164**, 114504 (2020).
126. Silva, A. S. & Ghisi, E. Estimating the sensitivity of design variables in the thermal and energy performance of buildings through a systematic procedure. *J. Clean. Prod.* **244**, 118753 (2020).
127. Farnak, M., Esfahani, J. A. & Bozorgmehri, S. An experimental design of the solid oxide fuel cell performance by using partially oxidation reforming

- of natural gas. *Renew. Energy* **147**, 155–163 (2020).
128. Goel, N., Taylor, R. A. & Otanicar, T. A review of nanofluid-based direct absorption solar collectors: Design considerations and experiments with hybrid PV/Thermal and direct steam generation collectors. *Renew. Energy* **145**, 903–913 (2020).
129. Walker, B. W. *et al.* Rational design of microfabricated electroconductive hydrogels for biomedical applications. *Prog. Polym. Sci.* **92**, 135–157 (2019).
130. Kalicka, R. Optimal design and organisation of biomedical experiment. *Measurement* **26**, 19–44 (1999).
131. Weiner, D. J. Expert systems to aid in the formulation of hypotheses and design of experiments in biomedical research. *Math. Comput. Model.* **16**, 185–198 (1992).
132. Remache, D., Semaan, M., Rossi, J. M., Pithioux, M. & Milan, J. L. Application of the Johnson-Cook plasticity model in the finite element simulations of the nanoindentation of the cortical bone. *J. Mech. Behav. Biomed. Mater.* **101**, 103426 (2020).
133. Ferrari, A. C. & Basko, D. M. Raman spectroscopy as a versatile tool for studying the properties of graphene. *Nat. Nanotechnol.* **8**, 235–46 (2013).
134. Castro Neto, A. H., Guinea, F., Peres, N. M. R., Novoselov, K. S. & Geim, A. K. The electronic properties of graphene. *Rev. Mod. Phys.* **81**, 109–162 (2009).
135. Xuan Wang, Linjie Zhi, * and & Müllen*, K. Transparent, Conductive Graphene Electrodes for Dye-Sensitized Solar Cells. (2007). doi:10.1021/NL072838R
136. Alzari, V. *et al.* Tailoring the physical properties of nanocomposite films by the insertion of graphene and other nanoparticles. *Compos. Part B Eng.* **60**, 29–35 (2014).
137. Boland, C. S. *et al.* Title: Sensitive Electromechanical Sensors Using Viscoelastic Graphene-Polymer Nanocomposites. **354**, (2016).

138. O'Driscoll, D. P., Vega-Mayoral, V., Harley, I., Boland, C. S. & Coleman, J. N. Optimising composite viscosity leads to high sensitivity electromechanical sensors. *2D Mater.* **5**, 035042 (2018).
139. Perspectives in Quantum Hall Effects: Novel Quantum Liquids in Low-Dimensional Semiconductor Structures | Quantum Physics & Field Theory | Theoretical Physics | Physics & Astronomy | Subjects | Wiley. Available at: <https://www.wiley.com/en-us/Perspectives+in+Quantum+Hall+Effects%3A+Novel+Quantum+Liquids+in+Low+Dimensional+Semiconductor+Structures-p-9783527617265>. (Accessed: 22nd July 2019)
140. Lin, Y. & Connell, J. W. Advances in 2D boron nitride nanostructures: nanosheets, nanoribbons, nanomeshes, and hybrids with graphene. *Nanoscale* **4**, 6908 (2012).
141. Transition Metal Oxide - an overview | ScienceDirect Topics. Available at: <https://www.sciencedirect.com/topics/chemistry/transition-metal-oxide>. (Accessed: 4th July 2019)
142. Cunningham, G. *et al.* Solvent Exfoliation of Transition Metal Dichalcogenides: Dispersibility of Exfoliated Nanosheets Varies Only Weakly between Compounds. *ACS Nano* **6**, 3468–3480 (2012).
143. Li, L. *et al.* Black phosphorus field-effect transistors. *Nat. Nanotechnol.* **9**, 372–377 (2014).
144. Lucovsky, G., Zeller, D. & Whitten, J. L. O-vacancies in transition metal (TM) oxides: Coordination and local site symmetry of transition and negative ion states in TM₂O₃ and TMO₂ oxides. *Microelectron. Eng.* **88**, 1471–1474 (2011).
145. Kase, K., Yamaguchi, M., Suzuki, T. & Kaneko, K. Photoassisted Chemisorption of NO on ZnO. *J. Phys. Chem.* **99**, 13307–13309 (1995).
146. Linsebigler, A. L., Lu, G. & Yates, J. T. Photocatalysis on TiO₂ Surfaces: Principles, Mechanisms, and Selected Results. *Chem. Rev.* **95**, 735–758 (1995).

147. Masahiro Miyauchi, †,§, Akira Nakajima, †, Akira Fujishima, ‡, Kazuhito Hashimoto, *,† and & Toshiya Watanabe*, †. Photoinduced Surface Reactions on TiO₂ and SrTiO₃ Films: Photocatalytic Oxidation and Photoinduced Hydrophilicity. (1999). doi:10.1021/CM990556P
148. Socher, E., Bochobza-Degani, O., Nemirovsky, Y., TMOS-infrared uncooled sensor and focal plane array. *WO2004075251A3* (2004).
149. Hu, X., Li, G. & Yu, J. C. Design, Fabrication, and Modification of Nanostructured Semiconductor Materials for Environmental and Energy Applications. *Langmuir* **26**, 3031–3039 (2010).
150. Meyer, J. *et al.* Transition Metal Oxides for Organic Electronics: Energetics, Device Physics and Applications. *Adv. Mater.* **24**, 5408–5427 (2012).
151. Wang, J., Ma, F., Sun, M. Graphene, hexagonal boron nitride, and their heterostructures: properties and applications. *RSC advances*, **7**, 27, 16801-16822, (2017).
152. Du, H., Lin, X., Xu, Z. & Chu, D. Recent developments in black phosphorus transistors. *J. Mater. Chem. C* **3**, 8760–8775 (2015).
153. Haque, F., Daeneke, T., Kalantar-zadeh, K. & Ou, J. Z. Two-Dimensional Transition Metal Oxide and Chalcogenide-Based Photocatalysts. *Nano-Micro Lett.* **10**, 23 (2018).
154. Golden, J. *et al.* Rhenium variations in molybdenite (MoS₂): Evidence for progressive subsurface oxidation. *Earth Planet. Sci. Lett.* **366**, 1–5 (2013).
155. Wilson, J. A. & Yoffe, A. D. The transition metal dichalcogenides discussion and interpretation of the observed optical, electrical and structural properties. *Adv. Phys.* **18**, 193–335 (1969).
156. Joensen, P., Frindt, R. F. & Morrison, S. R. Single-layer MoS₂. *Mater. Res. Bull.* **21**, 457–461 (1986).
157. Two-Dimensional Transition-Metal Dichalcogenides Alexander V. Kolobov and Junji Tominaga. *MRS Bull.* **42**, 471 (2017).
158. Han, S. A., Bhatia, R. & Kim, S.-W. Synthesis, properties and potential

- applications of two-dimensional transition metal dichalcogenides. *Nano Converg.* **2**, 17 (2015).
159. Zeng, H. & Cui, X. An optical spectroscopic study on two-dimensional group-VI transition metal dichalcogenides. *Chem. Soc. Rev.* **44**, 2629–2642 (2015).
 160. Kuc, A., Zibouche, N. & Heine, T. Influence of quantum confinement on the electronic structure of the transition metal sulfide TS_2 . *Phys. Rev. B* **83**, 245213 (2011).
 161. Ovchinnikov, D., Allain, A., Huang, Y.-S., Dumcenco, D. & Kis, A. Electrical Transport Properties of Single-Layer WS_2 . *ACS Nano* **8**, 8174–8181 (2014).
 162. Katzke, H., Tolédano, P. & Depmeier, W. Phase transitions between polytypes and intralayer superstructures in transition metal dichalcogenides. *Phys. Rev. B* **69**, 134111 (2004).
 163. Backes, C. *et al.* Spectroscopic metrics allow in situ measurement of mean size and thickness of liquid-exfoliated few-layer graphene nanosheets. *Nanoscale* **8**, 4311–4323 (2016).
 164. Liu, H. & Liu, Y. Controlled Chemical Synthesis in CVD Graphene. *Phys. Sci. Rev.* **2**, (2017).
 165. Fu, Q. & Xiang, B. Monolayer transition metal disulfide: Synthesis, characterization and applications. *Prog. Nat. Sci. Mater. Int.* **26**, 221–231 (2016).
 166. Sutton, I. & Sutton, I. Frequency Analysis. *Process Risk Reliab. Manag.* 602–666 (2015). doi:10.1016/B978-0-12-801653-4.00015-1
 167. Gritsch, L., Meng, D. & Boccaccini, A. R. Nanostructured biocomposites for tissue engineering scaffolds. *Biomed. Compos.* 501–542 (2017). doi:10.1016/B978-0-08-100752-5.00021-4
 168. Hydrolysis of Metal Alkoxides and Synthesis of Simple Oxides by The Sol-Gel Method. in *The Chemistry of Metal Alkoxides* 107–125 (Kluwer Academic Publishers, 2002). doi:10.1007/0-306-47657-6_9

169. Roberts, M. R., Coltrain, B. K., & Melpolder, S. M. Dye polymer/sol-gel composites. *U.S. Patent No. 4,948,843* (1989).
170. García-Murillo, A., Le Luyer, C., Dujardin, C., Pedrini, C. & Mugnier, J. Elaboration and characterization of Gd₂O₃ waveguiding thin films prepared by the sol-gel process. *Opt. Mater. (Amst)*. **16**, 39–46 (2001).
171. Wang, B. & Hu, L. Optical and surface properties of hybrid TiO₂/ormosil planar waveguide prepared by the sol-gel process. *Ceram. Int.* **32**, 7–12 (2006).
172. Touam, T. *et al.* Low optical loss nano-structured TiO_2 TiO₂ planar waveguides by sol-gel route for photonic crystal applications. *Opt. Quantum Electron.* **46**, 23–37 (2014).
173. Yang, P. *et al.* Patterning Porous Oxides within Microchannel Networks. *Adv. Mater.* **13**, 427–431 (2001).
174. Hench, L.L., West, J.K., The sol-gel process. *Chem. Rev.*, **90**, 1, 33-72 (1990).
175. Bedu, M. *et al.* Sol-gel planar waveguides for improved fluorescence microarrays. *Thin Solid Films* **518**, 4450–4457 (2010).
176. and, Q. S. & Zhang*, Z. J. Shape Control and Associated Magnetic Properties of Spinel Cobalt Ferrite Nanocrystals. (2004). doi:10.1021/JA049931R
177. Nguyen, V. L. *et al.* Wafer-Scale Single-Crystalline AB-Stacked Bilayer Graphene. *Adv. Mater.* **28**, 8177–8183 (2016).
178. Schutte, W. J., Boer, J. L. D. E. & Jellinek, F. Structures of Tungsten Disulfide and Diselenide. *System* **209**, 207–209 (1987).
179. O'Brien, M., McEvoy, N., Hallam, T. *et al.* Transition Metal Dichalcogenide Growth via Close Proximity Precursor Supply. *Sci Rep* **4**, 7374 (2015).
180. Hummers, W. S. & Offeman, R. E. Preparation of Graphitic Oxide. *J. Am. Chem. Soc.* **80**, 1339–1339 (1958).
181. Brodie, B.C., On the atomic weight of graphite. *Philos. Trans. R. Soc.*

- London* **149**, 249–259 (1859).
182. Lubin, G. Handbook of composites. *Van Nostrand Reinhold* (1982).
 183. Coleman, J. N. *et al.* Two-Dimensional Nanosheets Produced by Liquid Exfoliation of Layered Materials. *Science* (80-.). **331**, 568–571 (2011).
 184. Kelly, A. G. *et al.* Whiskey-phase exfoliation: exfoliation and printing of nanosheets using Irish whiskey. *2D Materials*, **6**, 4, 045036 (2019).
 185. Bergin, S. D. *et al.* Multicomponent Solubility Parameters for Single-Walled Carbon Nanotube–Solvent Mixtures. *ACS Nano* **3**, 2340–2350 (2009).
 186. Bergin, S. D. *et al.* Towards Solutions of Single-Walled Carbon Nanotubes in Common Solvents. *Adv. Mater.* **20**, 1876–1881 (2008).
 187. Varrla, E. *et al.* Turbulence-assisted shear exfoliation of graphene using household detergent and a kitchen blender. *Nanoscale* **6**, 11810–11819 (2014).
 188. Backes, C. *et al.* Production of Highly Monolayer Enriched Dispersions of Liquid-Exfoliated Nanosheets by Liquid Cascade Centrifugation Supplementary. *ACS Nano* 2016, **10**, 1, 1589-160 (2016).
 189. McManus, D. *et al.* Water-based and Biocompatible 2D Crystal Inks: from Ink Formulation to All- Inkjet Printed Heterostructures. *Nat. Nanotechnology*, **12**, 4, 343–350 (2017).
 190. Wang, H., Li, Z. & Mitlin, D. Tailoring Biomass-Derived Carbon Nanoarchitectures for High-Performance Supercapacitors. *ChemElectroChem* **1**, 332–337 (2014).
 191. Griffin, A. *et al.* Spectroscopic size and thickness metrics for liquid-exfoliated h-BN. *Chem. Mater.* **30**, 6, 1998-2005, (2018).
 192. Harvey, A. *et al.* Production of Ni(OH)₂ nanosheets by liquid phase exfoliation: from optical properties to electrochemical applications. *J. Mater. Chem. A* **4**, 11046–11059 (2016).
 193. Coleman, J. N. Liquid-Phase Exfoliation of Nanotubes and Graphene. *Adv. Funct. Mater.* **19**, 3680–3695 (2009).

194. Hansen, C. M. The Universality of the Solubility Parameter. *Ind. Eng. Chem. Prod. Res. Dev.* **8**, 2–11 (1969).
195. Hansen, C. M. Hansen Solubility Parameters - A User's Handbook. *CRC Press, Boca Raton, FL* (2007).
196. Hamaker, H. C. The London—van der Waals attraction between spherical particles. *Physica* **4**, 1058–1072 (1937).
197. Kunjappu, J. T. & Rosen, M. J. *Surfactants and interfacial phenomena*. Wiley (2013).
198. Kim, S. H. *et al.* Electrolyte-Gated Transistors for Organic and Printed Electronics. *Adv. Mater.* **25**, 1822–1846 (2013).
199. Findenegg, G. H. J. N. Israelachvili: Intermolecular and Surface Forces (With Applications to Colloidal and Biological Systems). Academic Press, London, Orlando, San Diego, New York, Toronto, Montreal, Sydney, Tokyo 1985. 296 Seiten, Preis: \$ 65.00. *Berichte der Bunsengesellschaft für Phys. Chemie* **90**, 1241–1242 (1986).
200. Tian, X. *et al.* Shear-Assisted Production of Few-Layer Boron Nitride Nanosheets by Supercritical CO₂ Exfoliation and Its Use for Thermally Conductive Epoxy Composites. *Scientific Reports* **7**, (2017).
201. Salussolia, G., Barbieri, E., Pugno, N. M. & Botto, L. Micromechanics of liquid-phase exfoliation of a layered 2D material: a hydrodynamic peeling model. *J. Mech. Phys. Solids* 103764 (2019). doi:10.1016/j.jmps.2019.103764
202. Chen, H. *et al.* Facile one-step exfoliation of large-size 2D materials via simply shearing in triethanolamine. *Mater. Lett.* **199**, 124–127 (2017).
203. Wu, P.-R., Liu, Z. & Cheng, Z.-L. A top-down exfoliation for MoS₂ nanosheets based on Li⁺/Na⁺-intercalated and shearing synergistic process. *Mater. Lett.* **248**, 236–240 (2019).
204. Río, F. del, Boado, M. G., Rama, A. & Guitián, F. A comparative study on different aqueous-phase graphite exfoliation methods for few-layer graphene production and its application in alumina matrix composites. *J. Eur. Ceram.*

- Soc.* **37**, 3681–3693 (2017).
205. Zhu, T. T. *et al.* Exfoliation of montmorillonite and related properties of clay/polymer nanocomposites. *Appl. Clay Sci.* **169**, 48–66 (2019).
 206. Varrla, E., Backes, C., Paton, K., Large-Scale Production of Size-Controlled MoS₂ Nanosheets by Shear Exfoliation. *Chem. Mater.*, **27**, 3, 1129-1139 (2015).
 207. Yasmin, A., Abot, J., Daniel, I. M. Processing of clay/epoxy nanocomposites by shear mixing. *Scripta Mater.* **49**, 1, 81-86 (2003).
 208. Chen, C. & Tolle, T. B. Fully exfoliated layered silicate epoxy nanocomposites. *J. Polym. Sci. Part B Polym. Phys.* **42**, 3981–3986 (2004).
 209. Hall, S., Cooke, M., Pacek, A. W., Kowalski, A. J. & Rothman, D. Scaling up of silverson rotor–stator mixers. *Can. J. Chem. Eng.* **89**, 1040–1050 (2011).
 210. Lab Mixer | High Shear Industrial Laboratory Mixers Homogenisers. Available at: <https://www.silverson.co.uk/en/products/laboratory-mixers#how-it-works>. (Accessed: 19th August 2019)
 211. Utomo, A.; Baker, M.; Pacek, A.W. The effect of stator geometry on the flow pattern and energy dissipation rate in a rotor-stator mixer. *Chem. Eng. Res. Des.* **87**, 533–542 (2009).
 212. Silverson.com. *Lab Mixer | High Shear Industrial Laboratory Mixers*. [online] Available at: <https://www.silverson.com/us/products/laboratory-mixers/>.(2019).
 213. Pope, S. B. Turbulent Flows. *Meas. Sci. Technol.* **12**, 2020–2021 (2001).
 214. Utomo, A. T., Baker, M. & Pacek, A. W. Flow pattern, periodicity and energy dissipation in a batch rotor–stator mixer. *Chem. Eng. Res. Des.* **86**, 1397–1409 (2008).
 215. Marchisio, D. L., Soos, M., Sefcik, J., Morbidelli, M. Role of turbulent shear rate distribution in aggregation and breakage processes. *AIChE journal*, **52**, 158–173 (2006).

216. Hughes, J. M., Aherne, D. & Coleman, J. N. Generalizing solubility parameter theory to apply to one- and two-dimensional solutes and to incorporate dipolar interactions. *J. Appl. Polym. Sci.* **127**, 4483–4491 (2013).
217. Barwich, S. T. No A Study of Liquid Phase Exfoliation and Properties of 2D Nanomaterials. *Doctoral Thesis Trinity College Library* (2015).
218. Namazi, H. Polymers in our daily life. *Bioimpacts* **7**, 73–74 (2017).
219. Ilschner, B., Lees, J. K., Dhingra, A. K. & McCullough, R. L. Composite Materials. in *Ullmann's Encyclopedia of Industrial Chemistry* (Wiley-VCH Verlag GmbH & Co. KGaA, 2000). doi:10.1002/14356007.a07_369
220. Callister, W. *Materials science and engineering : an introduction , Jr.—7th ed. p. cm.,TA403.C23 2007*, John Wiley & Sons. *Materials Science and Engineering* (2007). doi:10.1016/0025-5416(87)90343-0
221. Carraher Jr, Charles E. Seymour/Carraher's polymer chemistry. *CRC press* (2003).
222. Ebewele, R. O. Polymer Science and Technology. *CRC press* (2000).
223. Billmeyer, F. W. *Textbook of Polymer Science. Kobunshi* **12**, (1963).
224. Baer, E. Advanced Polymers. *Sci. Am.* **255**, 178–190 (1986).
225. Young, R. J. Introduction to polymers, third edition. *CRC Press* (2017).
226. Rodriguez, F., Cohen, C., Ober, C. K. & Archer, L. A. Principles of polymer systems. *CRC Press* (2014).
227. Bailey, F. E. (Frederick E. & Koleske, J. V. *Poly(ethylene oxide)*. *Academic Press* (1976).
228. French, A. C., Thompson, A. L. & Davis, B. G. High-Purity Discrete PEG-Oligomer Crystals Allow Structural Insight. *Angew. Chemie Int. Ed.* **48**, 1248–1252 (2009).
229. Beech, D. R. & Booth, C. Thermodynamic melting point of poly(ethylene oxide). *J. Polym. Sci. Part B Polym. Lett.* **8**, 731–734 (1970).
230. Fischer, E. W. & Kloos, F. Proof of the existence of a glass transition in the

- surface layers of polyethylene single crystals. *J. Polym. Sci. Part B Polym. Lett.* **8**, 685–693 (1970).
231. Wang, J., Porter, R. S. & Knox, J. R. Temperature coefficients for the viscosity of poly-1-olefins. *J. Polym. Sci. Part B Polym. Lett.* **8**, 671–675 (1970).
232. Polydimethylsiloxane - an overview | ScienceDirect Topics. Available at: <https://www.sciencedirect.com/topics/engineering/polydimethylsiloxane>. (Accessed: 15th October 2019)
233. Owen, M. J. Elastomers: Siloxane. *Encycl. Mater. Sci. Technol.* 2480–2482 (2001). doi:10.1016/B0-08-043152-6/00448-4
234. Dow Corning. Product Information: Sylgard(R) 170 Silicone Elastomer. (1999).
235. Mokkahan, J., Banlunara, W., Palaga, T., Sombuntham, P. & Wanichwecharungruang, S. Silicone Surface with Drug Nanodepots for Medical Devices. *ACS Appl. Mater. Interfaces* **6**, 20188–20196 (2014).
236. Chawla, K. *et al.* A novel low-friction surface for biomedical applications: Modification of poly(dimethylsiloxane) (PDMS) with polyethylene glycol(PEG)-DOPA-lysine. *J. Biomed. Mater. Res. Part A* **90A**, 742–749 (2009).
237. Kim, S. H., Moon, J.-H., Kim, J. H., Jeong, S. M. & Lee, S.-H. Flexible, stretchable and implantable PDMS encapsulated cable for implantable medical device. *Biomed. Eng. Lett.* **1**, 199–203 (2011).
238. Gruber, J. V., Lamoureux, B. R., Joshi, N. & Moral, L. Influence of cationic polysaccharides on polydimethylsiloxane (PDMS) deposition onto keratin surfaces from a surfactant emulsified system. *Colloids Surfaces B Biointerfaces* **19**, 127–135 (2000).
239. Denkov, N. D., Tcholakova, S., Marinova, K. G. & Hadjiiski, A. Role of Oil Spreading for the Efficiency of Mixed Oil–Solid Antifoams. *Langmuir* **18**, 5810–5817 (2002).
240. Marinova, K. G., Denkov, N. D., Branlard, P., Giraud, Y. & Deruelle, M.

- Optimal Hydrophobicity of Silica in Mixed Oil–Silica Antifoams. *Langmuir* **18**, 3399–3403 (2002).
241. Jha, B. K., Christiano, S. P. & Shah, D. O. Silicone Antifoam Performance: Correlation with Spreading and Surfactant Monolayer Packing. *Langmuir* **16**, 9947–9954 (2000).
 242. Mazumdar, S. Composites manufacturing: materials, product, and process engineering. *CRC Press* (2001).
 243. Khan, A. M., Pojman, J. A. The Use of Frontal Polymerization in Polymer Synthesis. *Trends in Polymer Science*, **4**, 8, 253-257 (1996).
 244. Kwak, J. C. T. (Jan C. T. *Polymer-surfactant systems*. (M. Dekker, 1998).
 245. Pojman, J. A. & Tran-Cong-Miyata, Q. Nonlinear Dynamics with Polymers : Fundamentals, Methods and Applications. *Wiley* (2011).
 246. Zhang, W., Camino, G. & Yang, R. Polymer/polyhedral oligomeric silsesquioxane (POSS) nanocomposites: An overview of fire retardance. *Prog. Polym. Sci.* **67**, 77–125 (2017).
 247. Tamburaci, S. & Tihminlioglu, F. Chitosan-hybrid poss nanocomposites for bone regeneration: the effect of poss nanocage on surface, morphology, structure and in vitro bioactivity. *Int. J. Biol. Macromol.* (2019). doi:10.1016/j.ijbiomac.2019.10.006
 248. Liu, Y. *et al.* Armor polyamide reverse osmosis membrane with POSS ‘armors’ through two-step interfacial polymerization for high anti-chlorine and anti-bacteria performance. *J. Memb. Sci.* **586**, 211–221 (2019).
 249. Liu, F. *et al.* Atomic oxygen-resistant polyimide composite fibers based on wet spinning of polyamic acid-POSS ammonium salts. *Polym. Degrad. Stab.* **168**, 108959 (2019).
 250. Strachota, B. *et al.* Polyurethane nanocomposites containing the chemically active inorganic Sn-POSS cages. *React. Funct. Polym.* **143**, 104338 (2019).
 251. Zhao, B., Xu, S., Adeel, M. & Zheng, S. Formation of POSS-POSS interactions in polyurethanes: From synthesis, morphologies to shape

- memory properties of materials. *Polymer (Guildf)*. **160**, 82–92 (2019).
252. Teng, S., Jiang, Z. & Qiu, Z. Effect of different POSS structures on the crystallization behavior and dynamic mechanical properties of biodegradable Poly(ethylene succinate). *Polymer (Guildf)*. **163**, 68–73 (2019).
253. Lipińska, M. & Imiela, M. Morphology, rheology and curing of (ethylene-propylene elastomer/hydrogenate acrylonitrile-butadiene rubber) blends reinforced by POSS and organoclay. *Polym. Test*. **75**, 26–37 (2019).
254. Kanezashi, M., Tomarino, Y., Nagasawa, H. & Tsuru, T. Tailoring the molecular sieving properties and thermal stability of carbonized membranes containing polyhedral oligomeric silsesquioxane (POSS)-polyimide via the introduction of norbornene. *J. Memb. Sci.* **582**, 59–69 (2019).
255. Shams, A., Mirbagheri, S. A. & Jahani, Y. The synergistic effect of graphene oxide and POSS in mixed matrix membranes for desalination. *Desalination* **472**, 114131 (2019).
256. Kibar, G. & Dinç, D. Ş. Ö. In-situ growth of Ag on mussel-inspired polydopamine@poly(M-POSS) hybrid nanoparticles and their catalytic activity. *J. Environ. Chem. Eng.* **7**, 103435 (2019).
257. Liu, Y. *et al.* Synthesis and application of PDMS/OP-POSS membrane for the pervaporative recovery of n-butyl acetate and ethyl acetate from aqueous media. *J. Memb. Sci.* **591**, 117324 (2019).
258. Kim, S.-W., Choi, S.-Y. & Rhee, H.-W. Sulfonated poly(etheretherketone) based nanocomposite membranes containing POSS-SA for polymer electrolyte membrane fuel cells (PEMFC). *J. Memb. Sci.* **566**, 69–76 (2018).
259. Zaharescu, T., Râpă, M., Lungulescu, E.-M. & Butoi, N. Filler effect on the degradation of γ -processed PLA/vinyl POSS hybrid. *Radiat. Phys. Chem.* **153**, 188–197 (2018).
260. Romo-Uribe, A. Viscoelasticity and microstructure of POSS-methyl methacrylate nanocomposites. Dynamics and entanglement dilution. *Polymer (Guildf)*. **148**, 27–38 (2018).

261. Wang, F. *et al.* Monolithic nanoporous polymers bearing POSS moiety as efficient flame retardant and thermal insulation materials. *React. Funct. Polym.* **143**, 104345 (2019).
262. Romo-Urbe, A. & Albanil, L. Dynamics retardation in hybrid POSS-NIPAm nanocomposites. Thermoplastic and thermally-responsive hydrogel behavior. *Eur. Polym. J.* **99**, 350–360 (2018).
263. Brown, D., Neyertz, S., Raaijmakers, M. J. T. & Benes, N. E. Sorption and permeation of gases in hyper-cross-linked hybrid poly(POSS-imide) networks: An in silico study. *J. Memb. Sci.* **577**, 113–128 (2019).
264. Sharma, A. K., Sloan, R., Ramakrishnan, R., Nazarenko, S. I. & Wiggins, J. S. Structure-property relationships in epoxy hybrid networks based on high mass fraction pendant POSS incorporated at molecular level. *Polymer (Guildf)*. **139**, 201–212 (2018).
265. Zhao, G. *et al.* Facile preparation and properties of polyhedral oligomeric silsesquioxane (POSS) nano-hybrid materials with disaggregation effect. *Mater. Sci. Eng. B* **246**, 136–142 (2019).
266. Gnanasekaran, D., Madhavpan, K. & Reddy, R. S. R. Developments of polyhedral oligomeric silsesquioxanes (POSS), POSS nanocomposites and their applications: A review. *J. Sci. Ind. Res. (India)*. **68**, 437–464 (2009).
267. Paolo P. Pescarmona, †, Maria E. Raimondi, ‡, John Tetteh, §, Ben McKay, ‡ and & Thomas Maschmeyer*, †,¶. Mechanistic Study of Silsesquioxane Synthesis by Mass Spectrometry and in Situ ATR FT-IR Spectroscopy. (2003). doi:10.1021/JP030665Y
268. Nasrollahzadeh, M., Sajadi, S. M., Sajjadi, M. & Issaabadi, Z. *An Introduction to Nanotechnology. Interface Science and Technology* **28**, (Elsevier Ltd., 2019).
269. Shang, L., Xu, J. & Nienhaus, G. U. Recent advances in synthesizing metal nanocluster-based nanocomposites for application in sensing, imaging and catalysis. *Nano Today* 100767 (2019). doi:10.1016/j.nantod.2019.100767
270. Zahran, M. & Marei, A. H. Innovative natural polymer metal

- nanocomposites and their antimicrobial activity. *Int. J. Biol. Macromol.* **136**, 586–596 (2019).
271. Nasrollahzadeh, M., *et al.* Types of Nanostructures. *Interface Sci. Technol.* **28**, 29–80 (2019).
272. Divya, V., Jeetika, Y. & Sangaranarayanan, M. V. Synthesis of silver-polyindole nanocomposite at water/dichloromethane interface: Nanomolar fluorescence detection of dopamine. *Mater. Today Proc.* (2019). doi:10.1016/j.matpr.2019.05.394
273. Abad-Álvarez, I. *et al.* Silver nanoparticles-clays nanocomposites as feed additives: Characterization of silver species released during in vitro digestions. Effects on silver retention in pigs. *Microchem. J.* **149**, 104040 (2019).
274. Kałuża, D., Gniadek, M., Michalska, A. & Maksymiuk, K. Polypyrrole – Gold nanocomposites. Templateless synthesis and electrochemical properties. *Electrochim. Acta* **320**, 134585 (2019).
275. Liu, D., Xu, L., Xie, J. & Yang, J. A perspective of chalcogenide semiconductor-noble metal nanocomposites through structural transformations. *Nano Mater. Sci.* **1**, 184–197 (2019).
276. Ly, T. N. & Park, S. Wearable strain sensor for human motion detection based on ligand-exchanged gold nanoparticles. *J. Ind. Eng. Chem.* (2019). doi:10.1016/j.jiec.2019.10.003
277. Esfahani, M. R. *et al.* A novel gold nanocomposite membrane with enhanced permeation, rejection and self-cleaning ability. *J. Memb. Sci.* **573**, 309–319 (2019).
278. Liu, H. *et al.* Mineralizing gold-silver bimetallics into hemin-melamine matrix: A nanocomposite nanozyme for visual colorimetric analysis of H₂O₂ and glucose. *Anal. Chim. Acta* (2019). doi:10.1016/j.aca.2019.09.025
279. Ma, Z., Xu, R., Wang, W. & Yu, D. A wearable, anti-bacterial strain sensor prepared by silver plated cotton/spandex blended fabric for human motion monitoring. *Colloids Surfaces A Physicochem. Eng. Asp.* **582**, 123918

- (2019).
280. Kolya, H., Kuila, T., Kim, N. H. & Lee, J. H. Bioinspired silver nanoparticles/reduced graphene oxide nanocomposites for catalytic reduction of 4-nitrophenol, organic dyes and act as energy storage electrode material. *Compos. Part B Eng.* **173**, 106924 (2019).
 281. Abou-Zeid, R. E., Awwad, N. S., Nabil, S., Salama, A. & Youssef, M. A. Oxidized alginate/gelatin decorated silver nanoparticles as new nanocomposite for dye adsorption. *Int. J. Biol. Macromol.* (2019). doi:10.1016/j.ijbiomac.2019.09.076
 282. Han Min, S., Asrulnizam, A. M., Atsunori, M. & Mariatti, M. Properties of Stretchable and Flexible Strain Sensor Based on Silver/PDMS Nanocomposites. *Mater. Today Proc.* **17**, 616–622 (2019).
 283. Mohammed Ali, M. *et al.* Printed strain sensor based on silver nanowire/silver flake composite on flexible and stretchable TPU substrate. *Sensors Actuators A Phys.* **274**, 109–115 (2018).
 284. Hu, T., Xuan, S., Ding, L. & Gong, X. Stretchable and magneto-sensitive strain sensor based on silver nanowire-polyurethane sponge enhanced magnetorheological elastomer. *Mater. Des.* **156**, 528–537 (2018).
 285. Min, S.-H., Lee, G.-Y. & Ahn, S.-H. Direct printing of highly sensitive, stretchable, and durable strain sensor based on silver nanoparticles/multi-walled carbon nanotubes composites. *Compos. Part B Eng.* **161**, 395–401 (2019).
 286. C60 Fullerene - an overview | ScienceDirect Topics. Available at: <https://www.sciencedirect.com/topics/chemistry/c60-fullerene>. (Accessed: 17th October 2019)
 287. Margetić, D., Štrukil, V., Margetić, D. & Štrukil, V. Applications of Ball Milling in Supramolecular Chemistry. *Mechanochemical Org. Synth.* 343–350 (2016). doi:10.1016/B978-0-12-802184-2.00008-X
 288. Rode, A. V., Christy, A. G., Gamaly, E. G., Hyde, S. T. & Luther-Davies, B. Magnetic Properties of Novel Carbon Allotropes. *Carbon Based Magn.* 463–

- 482 (2006). doi:10.1016/B978-044451947-4/50021-9
289. Yang, L. & Yang, L. Carbon nanostructures: new materials for orthopedic applications. *Nanotechnology-Enhanced Orthop. Mater.* 97–120 (2015). doi:10.1016/B978-0-85709-844-3.00005-7
290. Nishinaga, J. Growth and characterisation of fullerene/GaAs interfaces and C60-doped GaAs and AlGaAs layers. *Mol. Beam Ep.* 559–578 (2013). doi:10.1016/B978-0-12-387839-7.00024-5
291. Xie, S., Li, W., Pan, Z., Chang, B. & Sun, L. Mechanical and physical properties on carbon nanotube. *J. Phys. Chem. Solids* **61**, 1153–1158 (2000).
292. Baughman, R. H., Zakhidov, A. A. & de Heer, W. A. Carbon nanotubes--the route toward applications. *Science* **297**, 787–92 (2002).
293. Popov, V. Carbon nanotubes: properties and application. *Mater. Sci. Eng. R Reports* **43**, 61–102 (2004).
294. Jang, S.-C., Tsen, W.-C., Chuang, F.-S. & Gong, C. Simultaneously enhanced hydroxide conductivity and mechanical properties of quaternized chitosan/functionalized carbon nanotubes composite anion exchange membranes. *Int. J. Hydrogen Energy* **44**, 18134–18144 (2019).
295. Deep, N. & Mishra, P. Evaluation of mechanical properties of functionalized carbon nanotube reinforced PMMA polymer nanocomposite. *Karbala Int. J. Mod. Sci.* **4**, 207–215 (2018).
296. Sikora, P. *et al.* Mechanical and microstructural properties of cement pastes containing carbon nanotubes and carbon nanotube-silica core-shell structures, exposed to elevated temperature. *Cem. Concr. Compos.* **95**, 193–204 (2019).
297. Xia, Q., Zhang, Z., Liu, Y. & Leng, J. Self-assembly of cross-linked carbon nanotube films for improvement on mechanical properties and conductivity. *Mater. Lett.* **231**, 190–193 (2018).
298. Cheng, Z. *et al.* Constructing a weaving structure for aramid fiber by carbon nanotube-based network to simultaneously improve composites interfacial properties and compressive properties. *Compos. Sci. Technol.* **182**, 107721

- (2019).
299. Han, S., Meng, Q., Araby, S., Liu, T. & Demiral, M. Mechanical and electrical properties of graphene and carbon nanotube reinforced epoxy adhesives: Experimental and numerical analysis. *Compos. Part A Appl. Sci. Manuf.* **120**, 116–126 (2019).
 300. Poudel, Y. R. & Li, W. Synthesis, properties, and applications of carbon nanotubes filled with foreign materials: a review. *Mater. Today Phys.* **7**, 7–34 (2018).
 301. Rao, C., Sen, R. & Govindaraj, A. Fullerenes and carbon nanotubes. *Curr. Opin. Solid State Mater. Sci.* **1**, 279–284 (1996).
 302. Chaturvedi, P. *et al.* Electrical and electrochemical properties of carbon nanotube-based free standing LTO electrodes for current collector-free Li-ion batteries. *Curr. Appl. Phys.* **19**, 1150–1155 (2019).
 303. Guillet, J.-F., Valdez-Nava, Z., Golzio, M. & Flahaut, E. Electrical properties of double-wall carbon nanotubes nanocomposite hydrogels. *Carbon N. Y.* **146**, 542–548 (2019).
 304. Yahyazadeh, A., Khoshandam, B. & Kumar, R. V. An investigation into the role of substrates in the physical and electrochemical properties of carbon nanotubes prepared by chemical vapor deposition. *Phys. B Condens. Matter* **562**, 42–54 (2019).
 305. Vieira, T. A., Souza, J. R., Gimenes, D. T., Munoz, R. A. A. & Nossol, E. Tuning electrochemical and morphological properties of Prussian blue/carbon nanotubes films through scan rate in cyclic voltammetry. *Solid State Ionics* **338**, 5–11 (2019).
 306. Yang, L. *et al.* Effects of carbon nanotube on the thermal, mechanical, and electrical properties of PLA/CNT printed parts in the FDM process. *Synth. Met.* **253**, 122–130 (2019).
 307. Almagableh, A., Omari, M. A. & Sevostianov, I. Modeling of anisotropic elastic properties of multi-walled zigzag carbon nanotubes. *Int. J. Eng. Sci.* **144**, 103127 (2019).

308. Kumanek, B., Stando, G., Wróbel, P. S., Krzywiecki, M. & Janas, D. Thermoelectric properties of composite films from multi-walled carbon nanotubes and ethyl cellulose doped with heteroatoms. *Synth. Met.* **257**, 116190 (2019).
309. Chen, J., Han, J. & Xu, D. Thermal expansion properties of the polycaprolactam nanocomposites reinforced with single-walled carbon nanotubes. *Results Phys.* **12**, 1645–1652 (2019).
310. Karami, H. *et al.* The thermophysical properties and the stability of nanofluids containing carboxyl-functionalized graphene nano-platelets and multi-walled carbon nanotubes. *Int. Commun. Heat Mass Transf.* **108**, 104302 (2019).
311. Bian, L. & Gao, M. Thermal environment and strain energy related micro-model for properties of carbon nanotubes. *Mater. Sci. Eng. B* **244**, 72–80 (2019).
312. H. L. Cox. The elasticity and strength of paper and other fibrous materials. *Br. J. Appl. Phys.* **3**, 72–79 (1952).
313. White, E. F. T. Fracture behaviour of polymers. Edited by A. J. Kinloch and R. J. Young, Applied Science Publishers, London and New York, 1983. *Br. Polym. J.* **16**, 114–114 (1984).
314. Young, R. J. *et al.* The mechanics of reinforcement of polymers by graphene nanoplatelets. *Compos. Sci. Technol.* **154**, 110–116 (2018).
315. Khan, U., May, P., O’Neill, A. & Coleman, J. N. Development of stiff, strong, yet tough composites by the addition of solvent exfoliated graphene to polyurethane. *Carbon N. Y.* (2010). doi:10.1016/j.carbon.2010.07.008
316. Gong, L. *et al.* Interfacial Stress Transfer in a Graphene Monolayer Nanocomposite. *Adv. Mater.* **22**, 2694–2697 (2010).
317. Young, R. J. *et al.* Strain Mapping in a Graphene Monolayer Nanocomposite. *ACS Nano* **5**, 3079–3084 (2011).
318. Li, Z. *et al.* Effect of the orientation of graphene-based nanoplatelets upon the Young’s modulus of nanocomposites. *Compos. Sci. Technol.* **123**, 125–

- 133 (2016).
319. Kittel, C. *Introduction to Solid State Physics*. (Wiley, 2011).
320. Biccai, S. *et al.* Negative Gauge Factor Piezoresistive Composites Based on Polymers Filled with MoS₂ Nanosheets. *ACS Nano* acsnano.9b01613 (2019). doi:10.1021/acsnano.9b01613
321. Sahini, M. & Sahimi, M. *Applications of percolation theory*. (1994).
322. McLachlan, D. S., Blaszkiewicz, M. & Newnham, R. E. Electrical Resistivity of Composites. *J. Am. Ceram. Soc.* **73**, 2187–2203 (1990).
323. Stauffer, D. & Aharony, A. *Introduction to percolation theory*. (1994).
324. Balberg, I., Azulay, D., Toker, D., Millo, O. Percolation and tunneling in composite materials. *Int. J. Mod. Phys. B* **18**, 2091–2121 (2004).
325. Kirkpatrick, S. & Shante, V. K. S. *An Introduction to Percolation Theory*. *Advances in Physics* **20**, (1971).
326. Mohanty, K. K., Ottino, J. M. & Davis, H. T. Reaction and transport in disordered composite media: Introduction of percolation concepts. *Chem. Eng. Sci.* **37**, 905–924 (1982).
327. Bunde, A. & Dieterich, W. Percolation in composites. *J. Electroceramics* **5**, 81–92 (2000).
328. Hu, N., Karube, Y., Yan, C., Masuda, Z. & Fukunaga, H. Tunneling effect in a polymer/carbon nanotube nanocomposite strain sensor. *Acta Mater.* **56**, 2929–2936 (2008).
329. Amjadi, M., Kyung, K. U., Park, I. & Sitti, M. Stretchable, Skin-Mountable, and Wearable Strain Sensors and Their Potential Applications: A Review. *Adv. Funct. Mater.* **26**, 1678–1698 (2016).
330. Hurd, C. M. Quantum tunnelling and the temperature dependent DC conduction in low-conductivity semiconductors. *J. Phys. C Solid State Phys.* **18**, 6487–6499 (1985).
331. Barlian, A. A., Park, W.-T., Mallon, J. R., Rastegar, A. J. & Pruitt, B. L. Review: Semiconductor Piezoresistance for Microsystems. *Proc. IEEE* **97**,

- 513–552 (2009).
332. Tan, J. *et al.* Large out-of-plane piezoelectricity of oxygen functionalized MXenes for ultrathin piezoelectric cantilevers and diaphragms. *Nano Energy* **65**, 104058 (2019).
 333. Reyes-Gasga, J. *et al.* Detection of the piezoelectricity effect in nanocrystals from human teeth. *J. Phys. Chem. Solids* **136**, 109140 (2020).
 334. Chen, J. *et al.* Output characteristics of thin-film flexible piezoelectric generators: A numerical and experimental investigation. *Appl. Energy* **255**, 113856 (2019).
 335. Chen, Y.-Y., Lin, L.-K. & Hung, M.-H. Controllable micrometer positioning design of piezoelectric actuators using a robust fuzzy eliminator. *Microelectron. Reliab.* **103**, 113497 (2019).
 336. Falconi, C. Piezoelectric nanotransducers. *Nano Energy* **59**, 730–744 (2019).
 337. Hu, N., Karube, Y., Yan, C., Masuda, Z. & Fukunaga, H. Tunneling effect in a polymer/carbon nanotube nanocomposite strain sensor. *Acta Mater.* **56**, 2929–2936 (2008).
 338. Park, J. *et al.* Giant Tunneling Piezoresistance of Composite Elastomers with Interlocked Microdome Arrays for Ultrasensitive and Multimodal Electronic Skins. *ACS Nano* **8**, 4689–4697 (2014).
 339. Marsden, A. J. *et al.* Electrical percolation in graphene–polymer composites. *2D Mater.* **5**, 032003 (2018).
 340. Druzhinin, A., Ostrovskii, I. & Liakh, N. Study of piezoresistance in GexSi1–x whiskers for sensor application. *Mater. Sci. Semicond. Process.* **8**, 193–196 (2005).
 341. Kozlovskiy, S. I., Nedostup, V. V. & Boiko, I. I. First-order piezoresistance coefficients in heavily doped p-type silicon crystals. *Sensors Actuators A Phys.* **133**, 72–81 (2007).
 342. Kozlovskiy, S. I. & Boiko, I. I. First-order piezoresistance coefficients in silicon crystals. *Sensors Actuators A Phys.* **118**, 33–43 (2005).

343. Kalashnyk, N. *et al.* Strain sensing in single carbon fiber epoxy composites by simultaneous in-situ Raman and piezoresistance measurements. *Carbon N. Y.* **109**, 124–130 (2016).
344. Li, Z., Ye, L., Shen, J., Xie, K. & Li, Y. Strain-gauge sensing composite films with self-restoring water-repellent properties for monitoring human movements. *Compos. Commun.* **7**, 23–29 (2018).
345. Lee, Y.-J. *et al.* Auxetic elastomers: Mechanically programmable meta-elastomers with an unusual Poisson's ratio overcome the gauge limit of a capacitive type strain sensor. *Extrem. Mech. Lett.* **31**, 100516 (2019).
346. Conductivity, E. Electrical properties Basic laws and electrical properties of metals (I). *Mater. Sci.* 1–10
347. Transport, C. Lecture 3 Semiconductor Physics (II) Carrier Transport. *Spring* 1–16 (2007).
348. Wiedmann, S. *et al.* Coexistence of electron and hole transport in graphene. *Phys. Rev. B - Condens. Matter Mater. Phys.* **84**, 3–7 (2011).
349. Johnson, O. K., Kaschner, G. C., Mason, T. A., Fullwood, D. T. & Hansen, G. Optimization of nickel nanocomposite for large strain sensing applications. *Sensors Actuators A Phys.* **166**, 40–47 (2011).
350. Guo, D., Pan, X. & He, H. A simple and cost-effective method for improving the sensitivity of flexible strain sensors based on conductive polymer composites. *Sensors Actuators A Phys.* **298**, 111608 (2019).
351. Zhang, F., Wu, S., Peng, S., Sha, Z. & Wang, C. H. Synergism of binary carbon nanofibres and graphene nanoplates in improving sensitivity and stability of stretchable strain sensors. *Compos. Sci. Technol.* **172**, 7–16 (2019).
352. Harris, D. C. Quantitative chemical analysis. *W.H. Freeman and Co* (2007).
353. Swinehart, D. F. The Beer-Lambert Law. *J. Chem. Educ.* **39**, 333 (1962).
354. Goebel, D. G. Generalized Integrating-Sphere Theory. *Appl. Opt.* **6**, 125 (1967).

355. Raman, C. V. A new radiation [Reproduced from Indian J. Phys., 1928, 2, 387–398]. *Current Science* **74**, 382–386
356. Li, Z. *et al.* Deformation of wrinkled graphene. *ACS Nano* **9**, 3917–25 (2015).
357. Olszewski, S. De Broglie’s Velocity of Transition between Quantum Levels and the Quantum of the Magnetic Spin Moment Obtained from the Uncertainty Principle for Energy and Time. *J. Mod. Phys.* **05**, 2022–2029 (2014).
358. Carter, C. B., Williams, D. B. Transmission electron microscopy : diffraction, imaging, and spectrometry. *Springer* (2016).
359. Reimer, L. Scanning electron microscopy : physics of image formation and microanalysis. *Springer Vol. 45* (2013).
360. Bertolazzi, S., Brivio, J. & Kis, A. Stretching and Breaking of Ultrathin MoS₂. *ACS Nano* **5**, 9703–9709 (2011).
361. Eaton, P. J. & West, P. *Atomic force microscopy*. (Oxford University Press, 2010).
362. Viinikanoja, A. *et al.* Interactions between graphene sheets and ionic molecules used for the shear-assisted exfoliation of natural graphite. *Carbon N. Y.* **68**, 195–209 (2014).
363. Simon, D. A. *et al.* Graphene-based masterbatch obtained via modified polyvinyl alcohol liquid-shear exfoliation and its application in enhanced polymer composites. *Mater. Des.* **134**, 103–110 (2017).
364. Biccai, S. *et al.* Exfoliation of 2D materials by high shear mixing. *2D Mater.* **6**, (2019).
365. Li, L. *et al.* Preparation of graphene nanosheets by shear-assisted supercritical CO₂ exfoliation. *Chem. Eng. J.* **284**, 78–84 (2016).
366. Varrla, E. *et al.* Large-Scale Production of Size-Controlled MoS₂ Nanosheets by Shear Exfoliation. *Chem. Mater.* **27**, 1129–1139 (2015).
367. Viinikanoja, A. *et al.* Interactions between graphene sheets and ionic

- molecules used for the shear-assisted exfoliation of natural graphite. *Carbon N. Y.* **68**, 195–209 (2014).
368. Xu, Q.-Q., Zhao, W., Zhi, J.-T. & Yin, J.-Z. Exfoliation of graphite in CO₂ expanded organic solvents combined with low speed shear mixing. *Carbon N. Y.* **135**, 180–186 (2018).
369. Son, D. *et al.* An integrated self-healable electronic skin system fabricated via dynamic reconstruction of a nanostructured conducting network. *Nat. Nanotechnol.* **13**, 1057–1065 (2018).
370. Lee, S. *et al.* A transparent bending-insensitive pressure sensor. *Nat. Nanotechnol.* **11**, 472–478 (2016).
371. Li, Q., Luo, S., Wang, Y. & Wang, Q.-M. Carbon based Polyimide Nanocomposites Thin Film Strain Sensors Fabricated by Ink-jet Printing Method. *Sensors Actuators A Phys.* 111664 (2019). doi:10.1016/j.sna.2019.111664
372. Losaria, P. M. & Yim, J.-H. A highly stretchable large strain sensor based on PEDOT–thermoplastic polyurethane hybrid prepared via in situ vapor phase polymerization. *J. Ind. Eng. Chem.* **74**, 108–117 (2019).
373. Sato, J. *et al.* Ferroelectric polymer-based fully printed flexible strain rate sensors and their application for human motion capture. *Sensors Actuators A Phys.* **295**, 93–98 (2019).
374. Gogurla, N., Roy, B., Park, J.-Y. & Kim, S. Skin-contact actuated single-electrode protein triboelectric nanogenerator and strain sensor for biomechanical energy harvesting and motion sensing. *Nano Energy* **62**, 674–681 (2019).
375. Wang, L. *et al.* Highly stretchable, anti-corrosive and wearable strain sensors based on the PDMS/CNTs decorated elastomer nanofiber composite. *Chem. Eng. J.* **362**, 89–98 (2019).
376. Souri, H. & Bhattacharyya, D. Highly stretchable and wearable strain sensors using conductive wool yarns with controllable sensitivity. *Sensors Actuators A Phys.* **285**, 142–148 (2019).

377. Maskay, A., Hummels, D. M. & Pereira da Cunha, M. SAWR dynamic strain sensor detection mechanism for high-temperature harsh-environment wireless applications. *Measurement* **126**, 318–321 (2018).
378. Liu, H. *et al.* Stretchable conductive nonwoven fabrics with self-cleaning capability for tunable wearable strain sensor. *Nano Energy* **66**, 104143 (2019).
379. Yan, T., Wang, Z. & Pan, Z.-J. Flexible strain sensors fabricated using carbon-based nanomaterials: A review. *Curr. Opin. Solid State Mater. Sci.* **22**, 213–228 (2018).
380. Chang, X. *et al.* ZnO nanorods/carbon black-based flexible strain sensor for detecting human motions. *J. Alloys Compd.* **738**, 111–117 (2018).
381. Piccolo, V. *et al.* Quasi-hemispherical voids micropatterned PDMS as strain sensor. *Opt. Mater. (Amst)*. **86**, 408–413 (2018).
382. Fan, R. *et al.* Practical research on photonic crystal fiber micro-strain sensor. *Opt. Fiber Technol.* **52**, 101959 (2019).
383. Matveenko, V. P., Kosheleva, N. A., Serovaev, G. S. & Voronkov, A. A. Registration of local damage based on the use of fiber-optic strain sensors and numerical simulation results. *Procedia Struct. Integr.* **17**, 363–370 (2019).
384. Zhu, P. *et al.* Ultra-high sensitivity strain sensor based on piezotronic bipolar transistor. *Nano Energy* **50**, 744–749 (2018).
385. Stassi, S., Cauda, V., Canavese, G. & Pirri, C. F. Flexible tactile sensing based on piezoresistive composites: a review. *Sensors (Basel)*. **14**, 5296–332 (2014).
386. Bora, C., Bharali, P., Baglari, S., Dolui, S. K. & Konwar, B. K. Strong and conductive reduced graphene oxide/polyester resin composite films with improved mechanical strength, thermal stability and its antibacterial activity. *Compos. Sci. Technol.* **87**, 1–7 (2013).
387. Bashmal, S., Siddiqui, M. & Arif, A. F. M. Experimental and Numerical Investigations on the Mechanical Characteristics of Carbon Fiber Sensors.

- Sensors (Basel)*. **17**, (2017).
388. Li, H. *et al.* From Bulk to Monolayer MoS₂: Evolution of Raman Scattering. *Adv. Funct. Mater.* **22**, 1385–1390 (2012).
389. Harvey, A. *et al.* Non-resonant light scattering in dispersions of 2D nanosheets. *Nat. Commun.* **9**, 4553 (2018).
390. Papageorgiou, D. G., Kinloch, I. A. & Young, R. J. Mechanical properties of graphene and graphene-based nanocomposites. *Progress in Materials Science* **90**, (2017).
391. Bertolazzi, S., Brivio, J. & Kis, A. Stretching and Breaking of Ultrathin MoS₂. *ACS nano* **5**, 12, 9703-9709 (2011). doi:10.1021/NN203879F
392. M. Cadek, *et al.* Reinforcement of Polymers with Carbon Nanotubes: The Role of Nanotube Surface Area. *Nano Lett.* **4**, 2, 353-356 (2004). doi:10.1021/NL035009O
393. Tong, Y., Lin, Y., Wang, S. & Song, M. A study of crystallisation of poly (ethylene oxide) and polypropylene on graphene surface. *Polymer (Guildf)*. **73**, 52–61 (2015).
394. Zhang, J. *et al.* One-pot synthesis of bio-functionally water-soluble POSS derivatives via efficient click chemistry methodology. *React. Funct. Polym.* **140**, 103–110 (2019).
395. Čolović, M. *et al.* Amphiphilic POSS-based ionic liquid electrolyte additives as a boost for dye-sensitized solar cell performance. *Sol. Energy* **183**, 619–631 (2019).
396. Zhang, Q. *et al.* Preparation and characterization of polypropylene supported electrospun POSS-(C₃H₆Cl)₈/PVDF gel polymer electrolytes for lithium-ion batteries. *Colloids Surfaces A Physicochem. Eng. Asp.* **580**, 123750 (2019).
397. Kovacs, J. Z. *et al.* On the influence of nanotube properties, processing conditions and shear forces on the electrical conductivity of carbon nanotube epoxy composites. *Nanotechnology* **20**, 155703 (2009).

398. Gabbett, C. *et al.* The Effect of Network Formation on the Mechanical Properties of 1D:2D Nano:Nano Composites. *Chem. Mater.* **30**, 5245–5255 (2018).
399. Hong, S. *et al.* The doping mechanism and electrical performance of polyethylenimine-doped MoS-2 transistor. *Phys. status solidi c* **14**, (2017).
400. Hu, N., Karube, Y., Yan, C., Masuda, Z. & Fukunaga, H. Tunneling effect in a polymer/carbon nanotube nanocomposite strain sensor. *Acta Mater.* **56**, 2929–2936 (2008).